

Air Force Institute of Technology

AFIT Scholar

Theses and Dissertations

Student Graduate Works

6-2022

Theory and Design of a Highly Compressed Dropped-Channel Polarimetric Synthetic Aperture Radar

John T. Becker

Follow this and additional works at: <https://scholar.afit.edu/etd>



Part of the [Signal Processing Commons](#)

Recommended Citation

Becker, John T., "Theory and Design of a Highly Compressed Dropped-Channel Polarimetric Synthetic Aperture Radar" (2022). *Theses and Dissertations*. 5479.

<https://scholar.afit.edu/etd/5479>

This Dissertation is brought to you for free and open access by the Student Graduate Works at AFIT Scholar. It has been accepted for inclusion in Theses and Dissertations by an authorized administrator of AFIT Scholar. For more information, please contact richard.mansfield@afit.edu.



**Theory and Design of a Highly Compressed
Dropped-Channel Polarimetric Synthetic
Aperture Radar**

DISSERTATION

John T. Becker, Captain, USAF
AFIT-ENG-DS-22-J-004

**DEPARTMENT OF THE AIR FORCE
AIR UNIVERSITY**

AIR FORCE INSTITUTE OF TECHNOLOGY

Wright-Patterson Air Force Base, Ohio

DISTRIBUTION STATEMENT A
APPROVED FOR PUBLIC RELEASE; DISTRIBUTION UNLIMITED.

The views expressed in this document are those of the author and do not reflect the official policy or position of the United States Air Force, the United States Department of Defense or the United States Government. This material is declared a work of the U.S. Government and is not subject to copyright protection in the United States.

AFIT-ENG-DS-22-J-004

THEORY AND DESIGN OF A HIGHLY COMPRESSED DROPPED-CHANNEL
POLARIMETRIC SYNTHETIC APERTURE RADAR

DISSERTATION

Presented to the Faculty
Graduate School of Engineering and Management
Air Force Institute of Technology
Air University
Air Education and Training Command
in Partial Fulfillment of the Requirements for the
Degree of Doctor of Philosophy in Electrical Engineering

John T. Becker, B.S.E.E., M.S.E.E.
Captain, USAF

June 2022

DISTRIBUTION STATEMENT A
APPROVED FOR PUBLIC RELEASE; DISTRIBUTION UNLIMITED.

AFIT-ENG-DS-22-J-004

THEORY AND DESIGN OF A HIGHLY COMPRESSED DROPPED-CHANNEL
POLARIMETRIC SYNTHETIC APERTURE RADAR

DISSERTATION

John T. Becker, B.S.E.E., M.S.E.E.
Captain, USAF

Committee Membership:

Dr. Julie A. Jackson
Chair

Dr. Matthew Fickus
Member

Dr. Peter Collins
Member

Abstract

Compressed sensing (CS) is a recent mathematical technique that leverages the sparsity in certain sets of data to solve an underdetermined system and recover a full set of data from a sub-Nyquist set of measurements of the data. Given the size and sparsity of the data, radar has been a natural choice to apply compressed sensing to, typically in the fast-time and slow-time domains. Polarimetric synthetic aperture radar (PolSAR) generates a particularly large amount of data for a given scene; however, the data tends to be sparse. Recently a technique was developed to recover a dropped PolSAR channel by leveraging antenna crosstalk information and using compressed sensing. In this dissertation, we build upon the initial concept of the dropped-channel PolSAR CS in three ways. First, we determine a metric which relates the measurement matrix to the ℓ_2 recovery error. The new metric is necessary given the deterministic nature of the measurement matrix. We then determine a range of antenna crosstalk required to recover a dropped PolSAR channel. Second, we propose a new antenna design that incorporates the relatively high levels of crosstalk required by a dropped-channel PolSAR system. Finally, we integrate fast- and slow-time compression schemes into the dropped-channel model in order to leverage sparsity in additional PolSAR domains and increase the compression ratio overall. The completion of these research tasks has allowed a more accurate description of a PolSAR system that compresses in fast-time, slow-time, and polarization; termed herein as highly compressed PolSAR. The description of a highly compressed PolSAR system is a big step towards the development of prototype hardware in the future.

For my wife, whose love and support made this possible.

Table of Contents

	Page
Abstract	iv
List of Figures	viii
List of Tables	xiv
List of Abbreviations	xv
List of Symbols	xvi
I. Introduction	1
1.1 Research Contributions	3
1.2 Document Structure	3
II. Relevant Background Information	4
2.1 Synthetic Aperture Radar Background	4
2.1.1 Spotlight SAR Background	5
2.1.2 Polarimetric SAR Background	11
2.2 Compressed Sensing Background	13
2.2.1 Compressed Sensing in SAR	15
2.3 Antenna Design Background	21
2.3.1 Typical Spotlight SAR Antenna Types	24
2.3.2 Microstrip Antenna Design Background	24
2.3.3 Antenna Crosstalk	27
III. Dropped-Channel PolSAR CS Model Robustness	29
3.1 Dropped-Channel PolSAR CS	30
3.2 Experiment 1: Simulated Point Target Scenes	36
3.2.1 Measuring Robustness	36
3.2.2 Simulated Point Target Results	38
3.3 Experiment 2: Simulated GOTCHA Scenes	80
3.4 Conclusions	84
IV. Dropped-Channel System Microstrip Antenna Design	86
4.1 Dropped-Channel PolSAR Antenna Design	86
4.2 Drop-Channel PolSAR Antenna Measurements	95
4.2.1 Measurement Data Compared with Model - Port 1	101
4.2.2 Measurement Data Compared with Model - Port 2	103
4.3 BPDN Results using Measured Antenna Crosstalk	107
4.4 Antenna Conclusions	113

	Page
V. Sub-Nyquist Sampling for Drop-Channel PolSAR Model	115
5.1 Integration of Sub-Nyquist SAR with Drop-Channel PolSAR Model	116
5.1.1 Single-channel Spotlight-mode SAR sub-Nyquist Model	117
5.1.2 Highly compressed PolSAR Model	121
5.2 Sub-Nyquist Drop-Channel PolSAR CS Results	122
5.2.1 Single-Channel Case	123
5.2.2 Fully-Polarimetric Case	130
5.2.3 GOTCHA Examples	135
5.3 Sub-Nyquist Drop-Channel PolSAR System Diagram	140
5.4 Sub-Nyquist Drop-Channel PolSAR CS Conclusions	141
VI. Conclusions	143
6.1 Research Contributions	144
6.2 Future Work	145
Bibliography	147

List of Figures

Figure		Page
1	Spotlight SAR collection	6
2	Polar-to-Rectangular resampling process	9
3	Example pointspread function for a spotlight SAR system.....	10
4	Canonical PolSAR Targets	12
5	Two methods of reporting PolSAR images	13
6	Xampling block diagram	16
7	QuadCS block diagram	16
8	Demonstration of the effects of the chipping sequence on a pure tone. The black line represents the low-pass filter cut-off.	18
9	Measured signal after low pass filtering/integrating	19
10	One sided spectrum of the recovered signal	19
11	Antenna Analysis Geometry.....	22
12	Sample layout of microstrip antenna.....	25
13	Sample layout of a dual-pol microstrip antenna	26
14	PSF for 2.5°, 5°, and 10° apertures, corresponding to 36.99 cm, 18.49 cm, and 9.25 cm cross-range resolution for center frequency 9.2881 GHz and grazing angle 0°.	35
15	Truth images for all deterministic scenes	40
16	Relative error on b (38) across crosstalk, scene, and PSF combinations for deterministic scenes, no channel dropped.	42
17	Success rate across crosstalk, scene, and PSF combinations for deterministic scenes, no channel dropped. A yellow square represents a success, and a blue square represents a failure.....	43

Figure		Page
18	Truth, observed, and recovered scenes for Deterministic Scene 2 using $\delta_1 = \delta_2 = 0.1995$ and a 2.5° aperture extent, no channel dropped	45
19	Truth, observed, and recovered scenes for Deterministic Scene 2 using $\delta_1 = \delta_2 = 0.1995$ and a 5° aperture extent, no channel dropped	46
20	Truth, observed, and recovered scenes for Deterministic Scene 2 using $\delta_1 = \delta_2 = 0.1995$ and a 10° aperture extent, no channel dropped	47
21	Relative error on b (38) across crosstalk, scene, and PSF combinations for deterministic scenes, HH channel dropped.	49
22	Success rate across crosstalk, scene, and PSF combinations for deterministic scenes, HH channel dropped. A yellow square represents a success, and a blue square represents a failure.....	50
23	Truth, observed, and recovered scenes for Deterministic Scene 2 using $\delta_1 = \delta_2 = 0.1995$ and a 2.5° aperture extent, HH channel dropped.....	52
24	Truth, observed, and recovered scenes for Deterministic Scene 2 using $\delta_1 = \delta_2 = 0.1995$ and a 5° aperture extent, HH channel dropped	53
25	Truth, observed, and recovered scenes for Deterministic Scene 2 using $\delta_1 = \delta_2 = 0.1995$ and a 10° aperture extent, HH channel dropped.....	54
26	Example random point target scene, 5% target density in b	56
27	Average of relative fit (38) across Monte Carlo trials - Target Density Levels 1, 5, 10%	57
28	Average of relative fit (38) across Monte Carlo trials - Target Density Levels 1-4%	59
29	Average of relative fit (38) across Monte Carlo trials - Target Density Levels 5, 7, and 10%.....	60

Figure		Page
30	Total success rate across Monte Carlo trials - Target Density Levels 1-4%	61
31	Total success rate across Monte Carlo trials - Target Density Levels 5, 7, and 10%	62
32	Highlight of the robustness region using the 2.5 degree aperture extent, 1% target density results.	64
33	Overall average ℓ_2 -error (38) and mutual coherence for each aperture extent	67
34	Surface plots comparing average relative error on \mathbf{b} and SXR for zero-phase crosstalk across all aperture extents for 1% target density and averaged across all sparsitly levels listed in Table 1.	68
35	Anti-Diagonal and Vertical slices of SXR surface plots in Figure 34 showing error on \mathbf{b} as a function of SXR.	69
36	Surface plots of each PSF and Crosstalk Pair showing average relative error on \mathbf{b} and SXR for Complex Crosstalk - 1% Target Density.	74
37	Average of relative fit (38) across Monte Carlo trials - Target Density Levels 1-4% - $\mathbf{T} \neq \mathbf{R}$ case	75
38	Average of relative fit (38) across Monte Carlo trials - Target Density Levels 5, 7, and 10% - $\mathbf{T} \neq \mathbf{R}$ case.	76
39	Total success rate across Monte Carlo trials - Target Density Levels 1-4% - $\mathbf{T} \neq \mathbf{R}$ case	77
40	Total success rate across Monte Carlo trials - Target Density Levels 5, 7, and 10% - $\mathbf{T} \neq \mathbf{R}$ case	78
41	Overall average relative error on \mathbf{b} for each aperture extent, $\mathbf{T} \neq \mathbf{R}$ case. Reference line is Point 4 (best performance) from $\mathbf{T} = \mathbf{R}$ case in Figure 33.	80
42	GOTCHA Calibration Sub-scene CMY Results	82
43	Relative ℓ_2 error of GOTCHA sub-scene for each crosstalk pair.	83
44	S-band Antenna Model in HFSS, Isometric View	88

Figure		Page
45	S-band Antenna Model in HFSS, Close-up View	89
46	All 4 S-parameters from HFSS model of S-band antenna. Horizontal red line shows the S_{11} goal and the vertical black lines show the desired bandwidth.	90
47	HFSS modeled Port 1 realized gain sweep across frequency at boresight in E-plane.....	91
48	HFSS modeled Port 1 realized gain at 3GHz, Polar Plot, E-plane.	92
49	HFSS modeled Port 1 measured gain at 3GHz, Polar Plot, H-plane.	93
50	HFSS modeled Port 2 realized gain sweep across frequency at boresight in E-plane.....	93
51	HFSS modeled Port 2 realized gain at 3GHz, Polar Plot, E-plane.	94
52	HFSS modeled Port 2 measured gain at 3GHz, Polar Plot, H-plane.	94
53	Constructed S-band antenna, top view.	95
54	Constructed S-band antenna, back view.	96
55	Constructed S-band antenna, close-up view.	96
56	Calibration horn on the test stand.....	97
57	Measurement horn in AFRL/RYMF ATEMS lab.	98
58	S-band antenna on test stand in ATEMS lab range.	99
59	S-band antenna connected to Agilent PNA for S-parameter measurement.	100
60	Measured S-parameters from constructed S-band antenna compared with HFSS model S-parameters.....	101
61	Port 1 measured gain sweep across frequency at boresight in E-plane compared with HFSS model.	102

Figure		Page
62	Port 1 measured gain at 3GHz, Polar Plot, E-plane compared to HFSS results.	103
63	Port 1 measured gain at 3GHz, Polar Plot, H-plane compared to HFSS results.	104
64	Port 2 measured gain sweep across frequency at boresight in E-plane.	105
65	Port 2 measured gain at 3GHz, Polar Plot, E-plane compared to HFSS results.	106
66	Port 2 measured gain at 3GHz, Polar Plot, H-plane compared to HFSS results.	106
67	Recovered test scenes using measured antenna crosstalk matrix and 2.5° aperture extent.	109
68	Recovered test scenes using measured antenna crosstalk matrix and 5° aperture extent.	111
69	Recovered test scenes using measured antenna crosstalk matrix and 10° aperture extent.	112
70	GOTCHA CMY results as a function of bandwidth.	116
71	Example of fast-time undersampling.	120
72	Example of slow-time undersampling	120
73	Truth image of the point target test scene.	124
74	PFA observed and BP recovered images of the scene with no undersampling and no chipping sequence, compared with truth	125
75	PFA observed and BP recovered images of the scene with 50% slow-time undersampling, compared with truth	127
76	PFA observed and BP recovered images of the scene with chipping sequence and no undersampling, compared with truth	128
77	BP recovered scene with 50% fast-time undersampling, compared with truth	129

Figure		Page
78	BP recovered scene with 50% fast-time and slow-time undersampling, compared with truth	130
79	Truth CMY image of full-pol point target test scene.	131
80	BP recovered scene with no undersampling and no channel drop compared with truth	133
81	BP recovered scene, 50% fast-time undersampling, no channel drop	134
82	BP recovered scene, 50% fast- and slow-time undersampling, no channel drop	134
83	BP recovered scene, 50% fast- and slow-time undersampling, HH dropped	135
84	Reference CMY image of calibration target sub-scene	136
85	Reference CMY image of parking lot sub-scene	137
86	CMY image of recovered calibration target sub-scene, $M_r = 0.9N_r$, $M_s = 0.9N_s$, HH Dropped ($M_p = 0.75N_p$)	138
87	CMY image of recovered parking lot sub-scene, $M_r = 0.9N_r$, $M_s = 0.9N_s$, HH Dropped ($M_p = 0.75N_p$)	139
88	Block Diagram for Sub-Nyquist Drop Channel PolSAR System	141

List of Tables

Table		Page
1	Simulation Parameters	38
2	Crosstalk Points to Define Robustness Region	63
3	Signed Error Difference of each Aperture Extent and Crosstalk Pair Shown in Figure 36.....	71
4	Relative Error on \mathbf{b} for test scenes.....	113
5	SAR System Parameters.....	123
6	Relative Error on \mathbf{x} for point target scenes.....	135

List of Abbreviations

Abbreviation	Page
SAR	Synthetic Aperture Radar 1
PolSAR	Polarimetric Synthetic Aperture Radar 1
CS	Compressed Sensing 1
PRF	Pulse Repetition Frequency 2
BPDN	Basis Pursuit Denoising 2
FFT	fast Fourier transform 8
PFA	Polar Format Algorithm 8
PSF	pointspread function 9
PRF	Pulse Repetition Frequency 12
CMY	Cyan-Magenta-Yellow 12
BP	Basis Pursuit 14
OMP	Orthogonal Matching Pursuit 14
IHT	Iterative Hard Thresholding 14
QuadCS	Quadrature Compressive Sampling 16
AIC	Analog-to-Information Conversion 16
ADC	Analog-to-Digital Conversion 30

List of Symbols

Symbol	Page
ρ_y	Range Resolution 5
B	Bandwidth 5
c	Speed of Light 5
ρ_x	Cross Range Resolution 5
λ	Wavelength 6
$\Delta\phi$	Azimuth Collection 6
ϵ	BPDN Tolerance 14
ζ_n	Jitter 20
W	Microstrip Width 25
L	Microstrip Length 25
h	Substrate Height 25
ϵ_r	Relative Permittivity 25
λ_0	Free-space Wavelength 25
Ω	Ohm 25
Ω_A	Beam Area 26
D	Directivity 26
Q	Quality Factor 26
f_r	Resonant Frequency 26
ϵ_e	Effective Permittivity 26

THEORY AND DESIGN OF A HIGHLY COMPRESSED DROPPED-CHANNEL POLARIMETRIC SYNTHETIC APERTURE RADAR

I. Introduction

Synthetic aperture radar (SAR) systems provide imaging capabilities independent of weather or lighting conditions, which are critical to military, civilian, and scientific efforts. The addition of polarimetry to synthetic aperture radar (PolSAR) adds geometric information about the scene that would be lost to a single polarized system. The cost of the additional polarimetric information comes in the form of additional data storage, processing, and transmitting requirements. The amount of additional data can limit the size of the scene that can be imaged, increase the time needed to transmit the scene data, or increase the size/memory requirements of a computer to reconstruct the scene once the data is received. In recent years, a technique called compressed sensing (CS) has been leveraged in attempts to lower the data volume required for SAR and PolSAR systems. **The goal of this research is to define required crosstalk levels for dropped-channel PolSAR CS, use the desired crosstalk design point to define and simulate a prototype antenna for a dropped-channel PolSAR CS system, and further increase the compression by integrating fast and slow-time CS methods to the dropped-channel PolSAR model.**

By measuring the polarimetric information in a SAR scene, details such as the geometry and electric response of targets in the scene can be determined [1,2]. The advantages of polarimetric information come with several trade-offs, such as the increased data storage, processing, and transmission requirements mentioned. Addi-

tionally, the effective pulse repetition frequency (PRF) must be reduced to measure the polarimetric information [3]. Fortunately, PolSAR scenes tend to be sparse with respect to targets or scatterers. The assumption of sparsity allows us to leverage CS techniques like basis pursuit denoising (BPDN) to reduce the data volume of measurements and still reconstruct the scene with low error [4]. Previous compression efforts have been in the polarization dimension. Specifically, the drop-channel PolSAR model is able to reconstruct a dropped polarization channel via the information contained in the system crosstalk [5–8]. Other compression techniques exist though. We are specifically interested in compression in fast and slow time dimensions [9–18] as they could complement current compression in the polarization dimension. Thus, the combination of compression techniques for fast time, slow time, and polarization dimensions is a major focus of our research effort.

In order to utilize the crosstalk information to perform dropped-channel PolSAR CS, a larger than typical amount of crosstalk is required [7]. Antenna designers typically attempt to minimize crosstalk in antennas and arrays, so a new antenna design is required. In order to design a new antenna, we need insight into the required amount of crosstalk needed for the drop-channel method. Moreover, due to manufacturing error and other physical variations, we are interested in what range of crosstalk levels will work for the drop-channel method. The required range of crosstalks, dubbed the model robustness, is determined using both simulated and realistic data. With the range of crosstalks is determined, the range is used to inform the design of a new antenna. A high-crosstalk antenna is then designed, built, tested and compared to the measured and simulated values. The measured values from the designed antenna are used in the drop-channel model to better simulate and analyze a compressed PolSAR system.

1.1 Research Contributions

Compressed sensing techniques have been applied to SAR before, but only recently in the polarization dimension [5–7]. Compression in the polarization dimension leaves room to further compress in fast and slow-time, as well as presents some challenges from a system design standpoint. As such, the author’s research contributions are as follows:

1. Determine a range of crosstalk levels that provides low ℓ_2 recovery error for a range of measurement matrices.
2. Design and simulation of an antenna capable of providing the desired crosstalk parameters for a compressed PolSAR system.
3. Incorporation of fast and slow-time undersampling to dropped-channel PolSAR model.
4. A unifying algorithm to combine polarimetric compression with fast- and slow-time compression to generate highly compressed PolSAR data.

1.2 Document Structure

The dissertation document is organized in the following manner. Chapter II presents relevant background information for the research areas in this document, Chapter III displays the robustness study on the drop-channel PolSAR model. Chapter IV details the design and test of an antenna for use in a potential drop-channel PolSAR system. Chapter V shows the inclusion of sub-Nyquist sampling in the drop-channel PolSAR model. Chapter VI presents general conclusions and recommendations for future research.

II. Relevant Background Information

The intent of this chapter is to provide a short introduction to the concepts and definitions used in this document. The reader is assumed to be familiar with the basic concepts of radar, image processing, compressed sensing, and antenna theory. Topics discussed in this chapter include SAR, microstrip antenna design, and compressed sensing. Specifically, this research effort builds off of the works of Jackson and Lee-Elkin [5–8]. As such, this chapter is meant to provide suitable background information needed to understand the terms, figures, and impacts of this dissertation.

2.1 Synthetic Aperture Radar Background

In 1951 Carl Wiley developed synthetic aperture radar while working at the Goodyear Aircraft Company [19]. Using a technique known as Doppler beam sharpening [20], the signals from a series of locations are summed to produce a finer azimuth resolution than the antenna beamwidth can achieve [21]. Since then, the technology has found a multitude of applications in the scientific, military, and civilian communities alike. Due to the numerous uses, SAR technology has been a topic of constant research and development.

There are three main collection structures used for SAR: strip-map, spotlight, and scanning. In strip-map SAR, the antenna pattern is kept static with respect to the platform. The data is collected in a strip as the platform moves to form an image along the platform's path. For more information on strip-map SAR, the reader is referred to [22–24]. This work will utilize the spotlight SAR architecture, in which the beam pattern is steered to a certain area while the platform moves. By moving the platform but steering the beam to the same area, spotlight SAR is able to observe different angles, instead of a different areas like in strip-map. Scanning

SAR, also called ScanSAR, can be thought of as a hybrid of strip-map and spotlight. In ScanSAR, the platform moves along a track like in strip-map, but the beam is steered, like in spotlight, in a scanning pattern. For more information on ScanSAR, the reader is referred to [25–27]. Spotlight mode was chosen for developing the data collection model and to allow leveraging of the public data sets used within this dissertation. The proposed methods could work for other SAR collection geometries with adjustments to the measurement matrices. Similarly, a monostatic collection is assumed in this research effort, though the proposed models could also work for bistatic collections with appropriate changes to the measurement, polarimetric, and spatial matrices.

2.1.1 Spotlight SAR Background.

A typical monostatic spotlight SAR collection scheme [22, 28] is shown in Figure 1. Other flight path options are available, such as a circular path surrounding the scene [29]. The slant range is the distance between the radar and a point on the ground in the scene, which can then be converted to ground range via a projection operation [22]. Slant plane reconstruction is used in this research effort.

In monostatic, single-polarized spotlight SAR, the slant range resolution (ρ_y) is defined by the bandwidth (B) in Hertz as [28]

$$\rho_y = \frac{c}{2B}, \quad (1)$$

where c is the speed of light in meters/second. Cross range resolution (ρ_x) is defined, under the small-angle assumption, as

$$\rho_x \approx \frac{\lambda}{2\Delta\phi} \quad (2)$$

where λ is the wavelength in meters and $\Delta\phi$ is the azimuth collection size in radians [28].

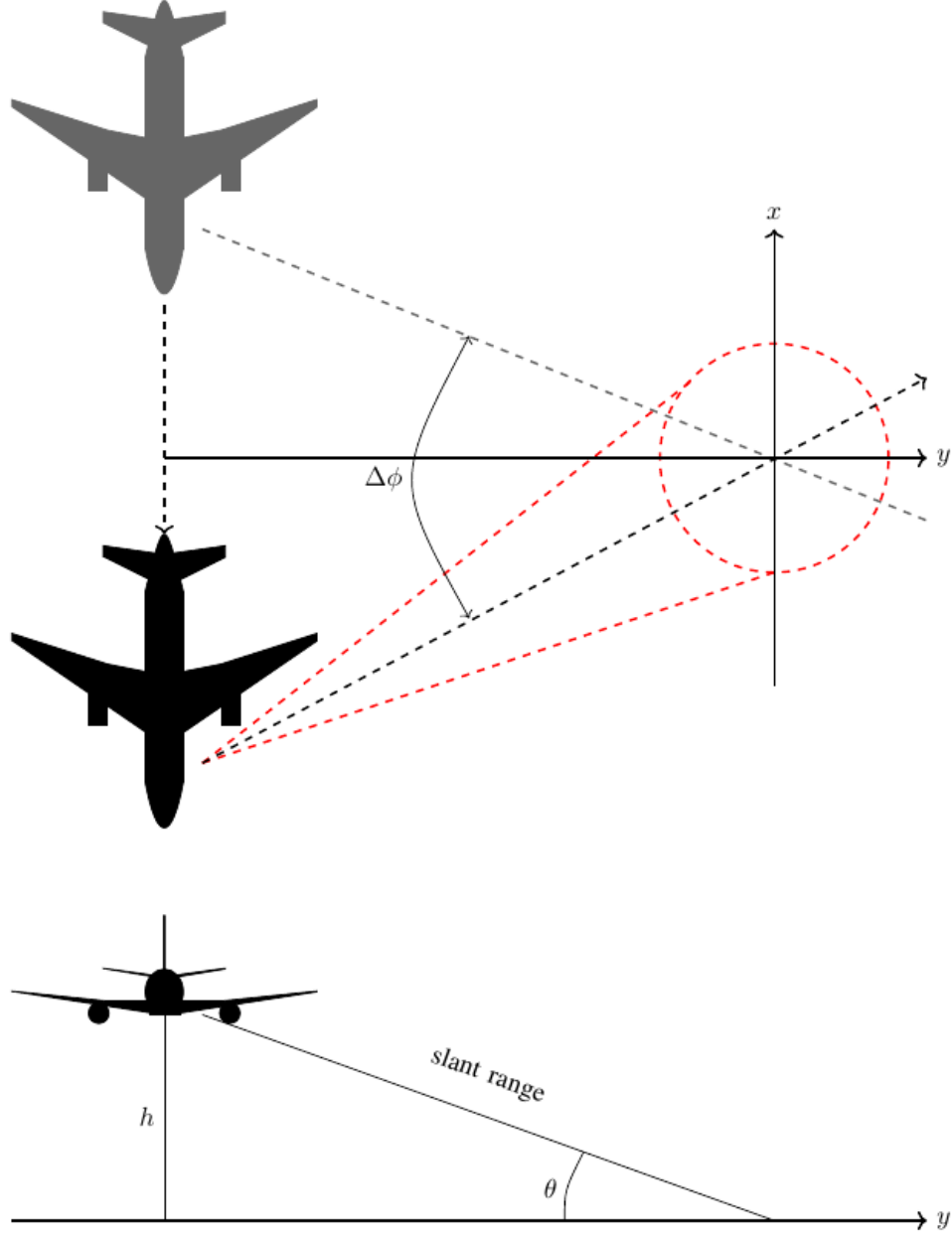


Figure 1. Spotlight SAR collection geometry

The collection aperture $\Delta\phi$ is broken up into a number of slow-time samples N_ϕ ,

which determines the maximum, unaliased crossrange size of the scene (D_ϕ) as [28]

$$D_\phi = \frac{\lambda N_\phi}{2\Delta\phi}. \quad (3)$$

At each slow-time sample location, a known signal is transmitted. That signal is then reflected by objects in the scene, convolving the signal with the scene reflectivity map. The reflected signal is then received by the SAR system where it goes through a deramping process [28] to deconvolve the transmitted signal from the scene reflectivity map. The analog, deramped signal is then sampled at the Nyquist rate to produce N_r fast-time samples. Much like in the slow-time dimension, the number of fast-time samples N_r determines the maximum unaliased range size of the scene (D_r) as [28]

$$D_r = \frac{cN_r}{2B}. \quad (4)$$

These fast-time samples are stored for each slow-time pulse. The collection of fast-time samples over all slow-time samples in the collection aperture form a matrix called the *phase history* in SAR terminology [28].

The fast-time sampled received signal at slow-time pulse ϕ_i and grazing angle θ in the spatial frequency domain is

$$r_{\phi,\theta}[n] = \sigma(x, y, z) \exp\{-j2\pi f_n/c\Delta R_q\} \quad (5)$$

where f_n is the n th discrete frequency of a set spanning the bandwidth with $n = 1, \dots, N_r$, $\sigma(x, y, z)$ is the frequency-independent, 3D scene reflectivity function, and ΔR_q is the differential range to the q th position in the discretized scene with $q =$

$1, \dots, N_r N_s N_z$, defined as

$$\begin{aligned} \Delta R_q = & x_q(\cos(\phi_t) \cos(\theta_t) + \cos(\phi_r) \cos(\theta_r)) \\ & + y_q(\sin(\phi_t) \cos(\theta_t) + \sin(\phi_r) \cos(\theta_r)) \\ & + z_q(\sin(\theta_t) + \sin(\theta_r)), \end{aligned} \quad (6)$$

where (x_q, y_q, z_q) are the coordinates of the q th position in the discretized scene, ϕ_t, ϕ_r are vectors of azimuth (ϕ) positions of the transmitter and receiver and θ_t, θ_r are vectors of the elevation (θ) positions of the transmitter and receiver. Using the projection slice theorem, the fast-time samples can be thought of as a range profile describing a 1D projection of the scene's reflectivity along constant range lines orthogonal to the look angle ϕ in the slant plane. By collecting pulses along a series of ϕ azimuth angles, a ribbon shaped collection surface is formed in the slant plane [28].

A consequence of the spotlight SAR collection geometry is that the phase history data are acquired on a polar raster instead of a rectangular grid. Thus, a resampling step is required before a 2-D inverse fast Fourier transform (FFT) can be used to form an image from the phase history data. The standard method of resampling the phase history data for spotlight SAR is called the polar format algorithm (PFA) [20–22, 28]. The PFA process is shown in Figure 2. The process consists of two steps. First, the samples are interpolated in the range dimension to a trapezoidal keystone grid. Then the samples are interpolated in cross-range onto a rectangular grid. With the data on a rectangular grid, the complex SAR image can be formed with a 2-D inverse FFT [28].

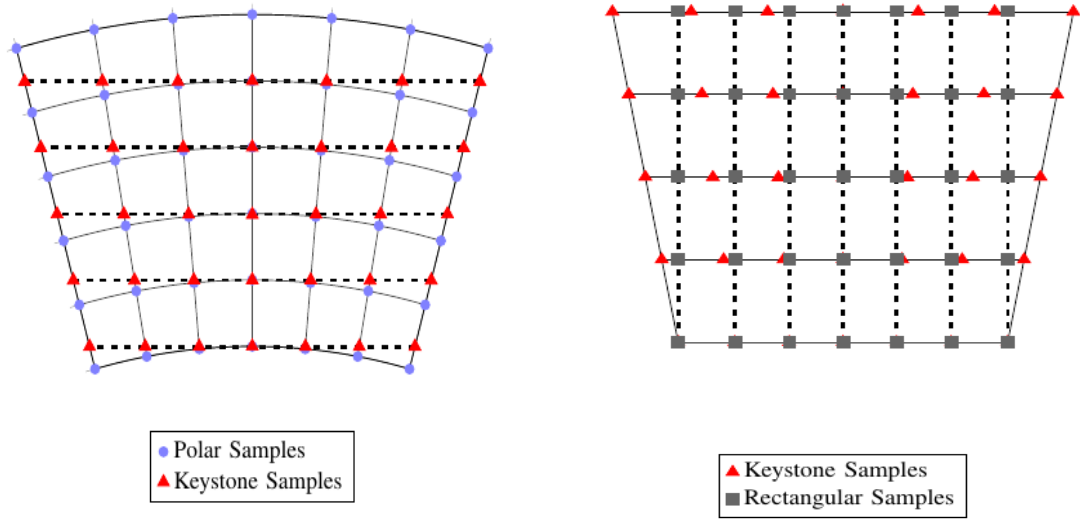


Figure 2. Polar-to-Rectangular resampling process in the PFA.

Figure 2 shows that care must be taken in the resampling process. Specifically, the size of the Fourier-domain, rectangular samples grid determines the image resolution. Likewise, the image coverage is determined by the number of samples on the rectangular grid [28]. A reduction in number of samples, or reduction in Fourier aperture will result in less coverage or resolution than the original polar data, respectively.

Another way to think about spotlight SAR image formation is to consider the convolution between the true reflectivity profile of the scene and the pointspread function (PSF) of the radar in the image domain. An example PSF can be seen in Figure 3. The PSF takes the form of a 2D sinc function due to the finite nature of the bandwidth and aperture extent. These limits can be thought of as a 2D rectangular window in the spatial frequency domain that limits the 2D Fourier transform of the scene reflectivity function via multiplication in the spatial frequency domain. After a 2D inverse FFT, the 2D rectangular window becomes a 2D sinc function and the multiplication becomes a 2D convolution. Imaging via 2D convolution with the PSF is the basis of the dropped-channel PolSAR model as presented in Chapter 3. Chapter

5 rolls back to using the PFA math in order to perform undersampling. While this research effort will exclusively use the PFA, other recovery algorithms are available for spotlight SAR, such as convolutional backprojection [21, 30], the chirp scaling algorithm [31, 32], and the Omega-k algorithm [33–35].

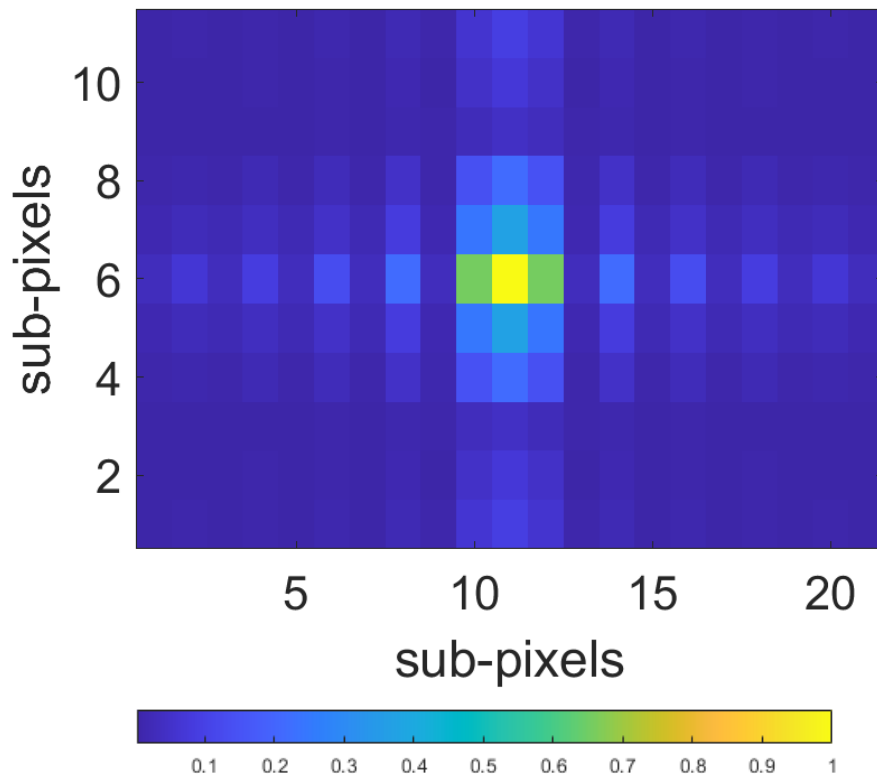


Figure 3. Example pointspread function for a spotlight SAR system.

For a more in-depth discussion of spotlight SAR background, the reader is referred to [21, 22, 28]. Spotlight SAR is an actively researched topic. Active areas of spotlight SAR research include imaging algorithms [36–39], autofocus techniques [40–42], hybrid imaging schemes [43, 44], compressed sensing techniques [7, 8, 45, 46], and polarimetric techniques [47, 48]. The measurement of multiple polarizations in PolSAR has several advantages and is integral to this research effort and thus is discussed in the next section.

2.1.2 Polarimetric SAR Background.

Polarimetric target decomposition was first formalized by Huynen [49] in his dissertation and since then several other polarimetric decompositions have been proposed [50]. The polarization, as defined by the orientation of the electric field [51], captures additional information, such as target geometry and materials [52], though for this research effort all materials are assumed to be perfect electric conductors. A common decomposition, and the one used in this dissertation is the Pauli decomposition basis defined as

$$\mathbf{P} = [\mathbf{p}_1 \quad \mathbf{p}_2 \quad \mathbf{p}_3 \quad \mathbf{p}_4] = \frac{1}{\sqrt{2}} \begin{bmatrix} 1 & 1 & 0 & 0 \\ 0 & 0 & 1 & -j \\ 0 & 0 & 1 & j \\ 1 & -1 & 0 & 0 \end{bmatrix} \quad (7)$$

where the first column (\mathbf{p}_1) represents scattering from a trihedral surface, \mathbf{p}_2 represents dihedral scattering, \mathbf{p}_3 corresponds to a rotated dihedral, and \mathbf{p}_4 captures helical-type scattering mechanisms [52]. Examples of scatterer geometry of the first three Pauli basis vectors are shown in Figure 4. In Figure 4, the axes represent the possible polarization orientations of the E-field. Specifically, the horizontal axis h represents the orientation of a horizontally polarized wave and the vertical axis v represents a vertically polarized wave.

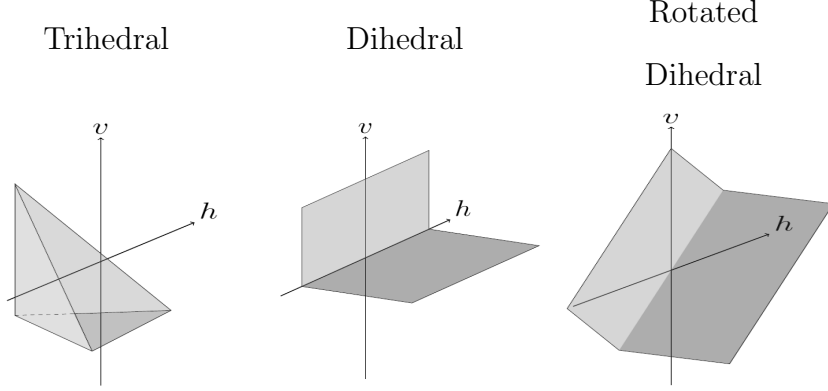


Figure 4. Canonical PolSAR Targets

A fully polarimetric SAR system requires the transmission of two orthogonal polarizations [3]. For the purposes of this research, the polarizations will be horizontal and vertical linear. The requirement of two orthogonal transmissions leads to an inherent delay of one PRI between each measurement. Since the above process must happen for each polarization channel, the pulse repetition frequency (PRF) must be doubled to maintain the alias-free cross-range image dimension of a single polarized system [3]. When the PRF is doubled, the horizontal and vertical pulses are transmitted sequentially. When a polarization is transmitted, both channels receive in order to capture the effects of target scattering in the scene.

Each polarization channel is put through the PFA individually, and the images can then be either reported separately, averaged together, or combined as a pseudo-color image [3]. This research effort will report both individual channels and a combined pseudo-color cyan-magenta-yellow (CMY) image for relevant scenes and reconstructions. An example of the reported images can be seen in Figure 5.

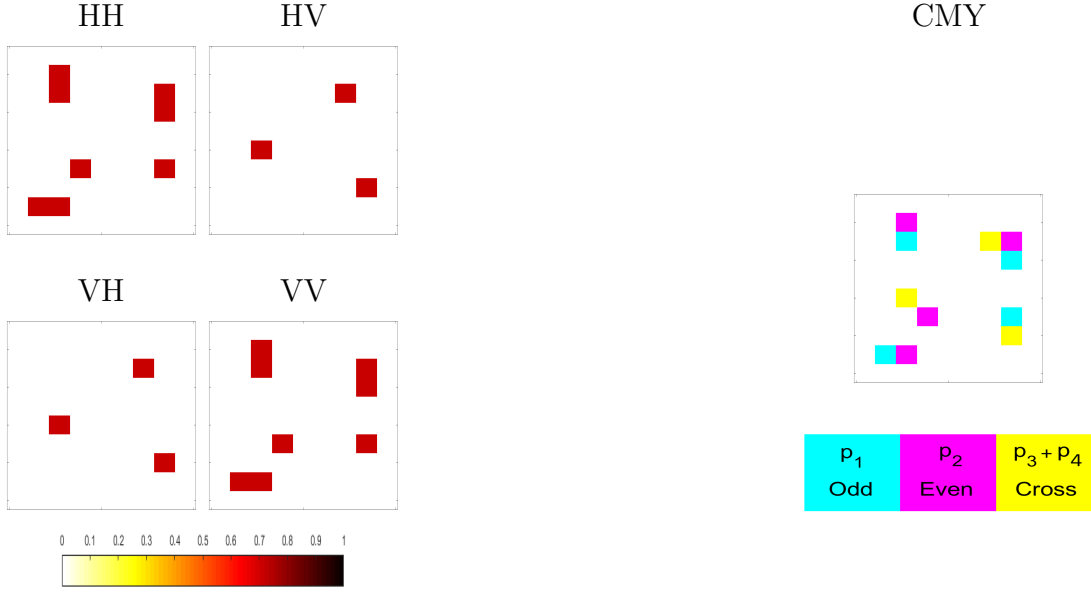


Figure 5. Two methods of reporting PolSAR images

The benefits of measuring fully polarimetric SAR scenes are not without drawbacks. Collecting additional polarization channels multiplies the data processing, storage, and transmission requirements of the system, increasing the cost and complexity of the system. Fortunately, SAR scenes tend to be sparse, meaning that there are relatively few targets in a particular area. The assumed sparsity of PolSAR means that a technique called compressed sensing [4] can be leveraged to alleviate some of the data requirements.

2.2 Compressed Sensing Background

Compressed sensing is a recent field of interest in the signal processing community, gaining traction in the 1990s and expanding to the field it is today [13]. The goal of compressed sensing is to solve the problem

$$\min_{\mathbf{b}} \|\mathbf{b}\|_0 \quad \text{subject to } \mathbf{A}\mathbf{b} = \mathbf{y}, \quad (8)$$

where $\mathbf{y} \in \mathbb{C}^m$ is observed data, $\mathbf{b} \in \mathbb{C}^N$ is the true, unknown scene data, and $\mathbf{A} \in \mathbb{C}^{m \times N}$ is an under-determined measurement matrix [4]. Here the ℓ_0 -norm ($\|\cdot\|_0$) is the total number of non-zero entries in the vector. Note that the ℓ_0 -norm is actually not actually a norm and calling it one is just a convenient abuse of notation [4]. Traditionally (8) represents an under-determined problem, which would be impossible to solve with classical linear algebra methods. However if \mathbf{b} is sparse in some domain, then compressed sensing techniques may be used to solve the problem [4]. Since ℓ_0 -minimization is an NP-hard problem, it is common to use an ℓ_1 relaxation to get a basis pursuit (BP) problem of the form

$$\min_{\mathbf{b}} \|\mathbf{b}\|_1 \quad \text{subject to } \mathbf{A}\mathbf{b} = \mathbf{y}. \quad (9)$$

The ℓ_1 -norm is a convex function, which allows the use of fast and efficient solvers [4]. Other solver algorithms are available, such as orthogonal matching pursuit (OMP) and iterative hard thresholding (IHT) [4]. The choice of a CS algorithm comes down to input sparsity, total input length, speed of the algorithm, and the ability to exploit fast matrix-vector products. For very sparse signals, OMP and IHT are extremely fast. For less sparse signals, such as those presented in the GOTCHA data set, BP algorithms can be much faster than OMP and IHT algorithms [4].

The main recovery algorithm used in this research is the BPDN algorithm, an extension of the BP algorithm. The standard form of a BPDN problem is

$$\min_{\mathbf{b}} \|\mathbf{b}\|_1 \quad \text{subject to } \|\mathbf{y} - \mathbf{A}\mathbf{b}\|_2 \leq \epsilon, \quad (10)$$

where ϵ is the tolerance. By restricting the ℓ_2 -norm of the difference between our measured data \mathbf{y} and the combination $\mathbf{A}\mathbf{b}$ to be less than some tolerance ϵ , BPDN is better suited to recover signals that have been contaminated by noise. For a more

in-depth discussion on CS algorithms, BPDN, and CS theory, the reader is referred to [4, 13].

2.2.1 Compressed Sensing in SAR.

In terms of SAR systems, there are three main domains that can benefit from undersampling and CS techniques. The fast-time range samples, the slow-time azimuth samples, and the polarization channels. While there are numerous examples of CS in fast-time undersampling [13–16, 53–61] and slow-time undersampling [17, 18, 62], as well as the recent techniques for compression across polarization channels [5–8, 63, 64], the author is unaware of any research that combines the compression of all three domains in one model. Thus, by incorporating fast-time and slow-time compression to the dropped channel PolSAR model, a new level of compressive sensing would be achieved.

The two main fast-time compression schemes that the author is aware of that also have suggested or prototype hardware are the quadrature compressive sampling architecture [59, 60, 65–68], and the Xampling architecture [56–58, 69]. These processes are also called analog-to-information sampling [58, 70, 71]. The focus of this research effort will be the quadrature compressive sampling, so the Xampling architecture will only be briefly presented for comparison.

The word Xampling is coined for the phrase “compressed sampling” and is used to describe a novel processing technique for signals in a union of subspaces [13]. A block diagram for Xampling [57] can be seen in Figure 6. The first block is called the “compressed ADC” (X-ADC) and is a combination of a compression to the analog signal and a low-rate ADC; the output are digital samples at a much lower rate than the original bandwidth [14]. The second block is the “compressed DSP” (X-DSP), which begins with a non-linear detector for determining the subspace in which the

analog signal was compressed. With the subspace identified a commercial, low-rate DSP can be used with existing algorithms to perform subspace reconstruction of the signal. A further treatment of Xampling can be found in [13, 56, 57, 69]. Additionally, hardware has been developed for Xampling and is described in [13, 55, 58].

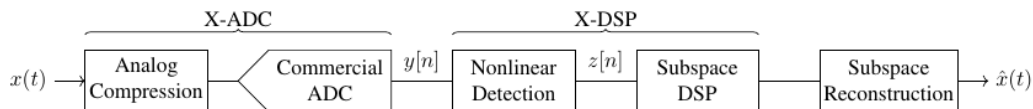


Figure 6. Xampling block diagram, adopted from [57, Fig 1]

An alternative to Xampling is a technique known as quadrature compressive sampling (QuadCS) [59] and is used in [60, 66] to perform the fast-time sub-Nyquist sampling portion of the sub-Nyquist SAR system. The QuadCS architecture is an evolution of the random demodulation analog-to-information conversion (AIC) process [59, 61, 70, 71]. A block diagram of QuadCS can be seen in Figure 7 adapted from [59, Fig 1].

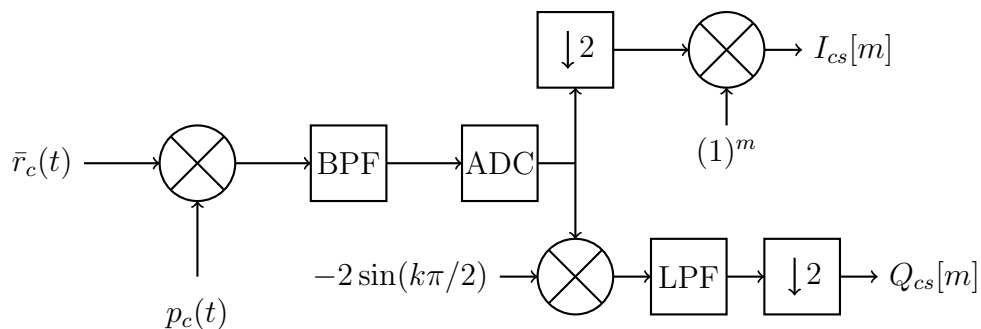


Figure 7. Sub-Nyquist Receiver adapted from [60]

In Figure 7, BPF stands for bandpass filter, LPF stands for low-pass filter, ADC stands for analog-to-digital converter, $\bar{r}_c(t)$ is the receiver signal, and $p_c(t)$ is the chipping sequence. The chipping sequence is used to randomly modulate the received signal and spread the received signal's spectral information across the entire spectrum

of the chipping sequence [61]. The chipping sequence is defined as

$$p_c(t) = \xi_k, \quad t \in \left[\frac{k}{B_p}, \frac{k+1}{B_p} \right), \quad k = 0, 1, \dots \quad (11)$$

where $\xi_k = 1$ or -1 and $B_p \geq B$ is the chipping bandwidth [59,61]. Thus, the chipping sequence randomly flips between $+1$ or -1 at or above the Nyquist rate of the received signal. The sequence in Figure 8 shows the effect of the chipping sequence on a pure tone signal. In the left column, the effect is shown in the time-domain and on the right the effect is shown on half of the spectrum. Moving down each column, the pure-tone received signal (top row) and the chipping sequence (middle row) are shown. On the bottom row, the result of the mixing operation is shown. The bottom row of Figure 8 is the input to the bandpass filter in Figure 7; however, for the example in Figure 8 a low pass filter is used [61]. The low pass filter cut-off is shown in bottom right sub figure of Figure 8 as a black line. The bandpass filter cut-off is at 100 Hz, well below the 512 Hz frequency of the input signal.

Figure 9 shows the single-sided frequency domain spectrum the measured signal. In [61], an accumulator which sums the demodulated signal for the inverse of the low-rate sampling frequency and samples the result is used as the low-pass filter. The low-rate sample rate is much lower than Nyquist sample rate and has a dependence of the number of significant frequencies in the received signal. Note that the single-sided spectrum of the measured signal goes to 50 Hz, whereas the spectrum in Figure 8 goes to 1024 Hz. Figure 10 shows the single-sided spectrum of the signal recovered with BP as

$$\min_{\mathbf{x}} \|\hat{\mathbf{x}}\|_1 \quad \text{subject to } \mathbf{H}\hat{\mathbf{P}}_c \mathbf{x} = \tilde{\mathbf{y}}^{cs}. \quad (12)$$

In (12), matrix $\hat{\mathbf{P}}_c$ is a toeplitz matrix that performs convolution with the frequency-domain chipping sequence shown in the middle row of Figure 8 [61]. Matrix \mathbf{H} per-

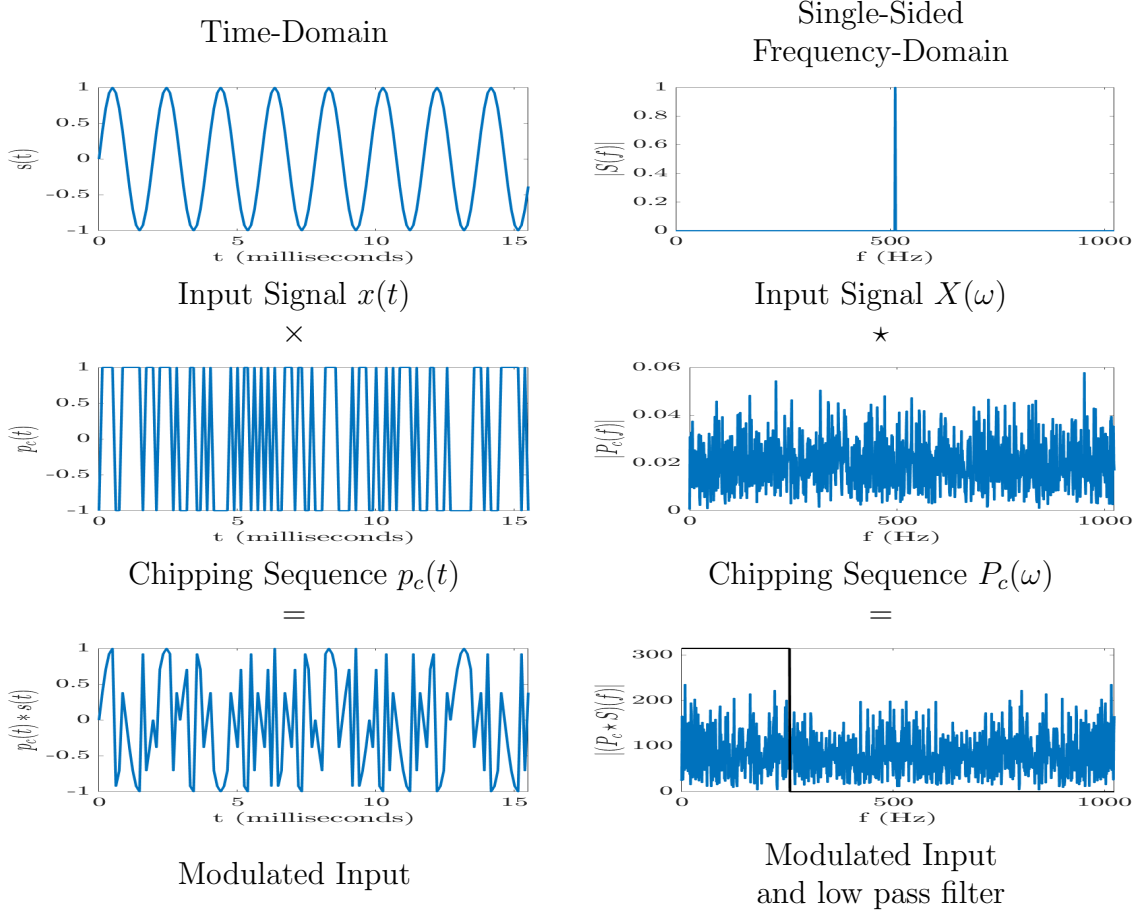


Figure 8. Demonstration of the effects of the chipping sequence on a pure tone. The black line represents the low-pass filter cut-off.

forms the low-pass filtering and accumulation operation, shown as the black line in the bottom row of Figure 8. The input spectrum on the top row of Figure 8 is \mathbf{x} , and the measured signal $\tilde{\mathbf{y}}^{cs}$ is shown in Figure 9. The BP solution $\hat{\mathbf{x}}$ is shown in Figure 10.

The frequency spike of the original signal is clearly visible. More details on the math required to set up the BPDN problem for the random demodulator can be found in [61]. The reader should think of the chipping sequence as a random, known noise that is mixed with the received signal in order to spread the tones across the entire spectrum. Then the low-pass filter is used for antialiasing, low-rate sampling is used to collect the signal and CS techniques can then be used to recover [61].

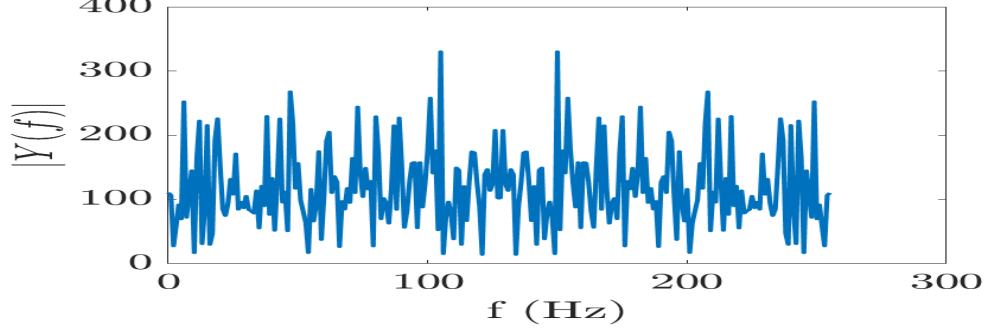


Figure 9. Measured signal after low pass filtering/integrating

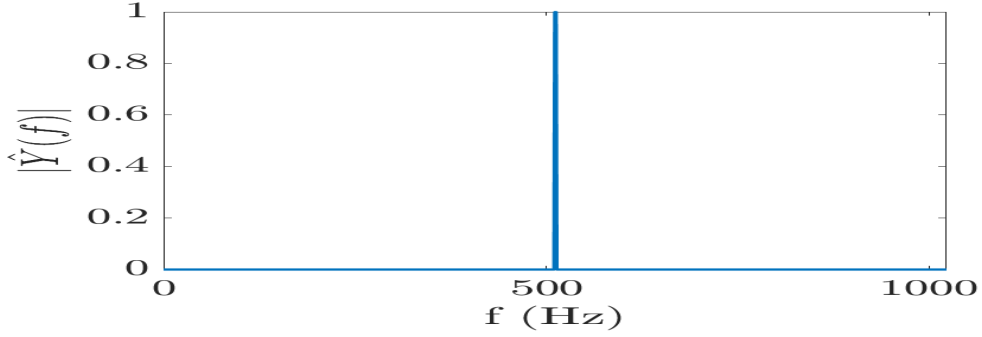


Figure 10. One sided spectrum of the recovered signal

In [59], the random demodulation model from [61] is merged with quadrature sampling to get the QuadCS model. In the merger, the low-pass filter is replaced by a bandpass filter as shown in Figure 7. The frequency-domain measurement model in [59] can be written as

$$\tilde{\mathbf{y}}^{cs} = \mathbf{R}\hat{\mathbf{P}}_c\hat{\mathbf{D}}\mathbf{x} + \eta \quad (13)$$

where \mathbf{x} is the length- N_r complex reflectivity vector, η is the length- N_r measurement noise, and $\tilde{\mathbf{y}}^{cs}$ is the length- M_r sub-Nyquist sampled radar echo, $\hat{\mathbf{D}} = [\hat{d}_{mn}] \in \mathbb{C}^{N_r \times N_r}$ is the frequency-domain waveform-matching dictionary with elements defined as

$$\hat{d}_{ln} = N_r^{-1/2} \hat{\psi}_n(e^{j(-\pi+2\pi(m-1)/N_r)}) \quad (14)$$

where $\hat{\psi}_n(e^{j\omega})$ is the discrete-time Fourier transform of Nyquist sampling sequence

and $l = 0, 1, \dots, N_r - 1$ and $n = 0, 1, \dots, N_r - 1$ [59]. The matrix $\hat{\mathbf{P}} = [\hat{p}_{ln}] \in \mathbb{C}^{N_r \times N_r}$ describes the convolution with the chipping sequence with elements

$$\hat{p}_{ln} = N_r^{-1/2} \rho[((l - n))_{N_r}] \quad (15)$$

where $((k))_{N_r}$ denotes $(k \text{ modulo } N_r)$ and the elements $\rho[\cdot]$ are the Fourier coefficients of the elements of the chipping sequence. The bandpass filtering and low-rate sampling are defined by $\mathbf{R} = [r_{ml}] \in \mathbb{R}^{M_r \times N_r}$ with

$$r_{ml} = \begin{cases} M_r^{-1/2} & l = (N_r - M_r)/2 + m \\ 0 & \text{else} \end{cases} \quad (16)$$

where $m = 0, 1, \dots, M_r - 1$. For a more in-depth mathematical analysis of the QuadCS algorithm, the reader is referred to [59]. In [60, 66] the QuadCS model was extended to SAR data. However, [60, 66] only looks at fast-time undersampling.

In [60], the authors state that slow-time undersampling is easily accomplished via observations at a random subset of azimuth locations. The method described in [17, 18, 62] gives two options for slow-time undersampling via reduction in transmitted pulses. The first is transmitting fewer pulses at random intervals. The second uses a time jitter of amount ζ_n for the n th sample such that the echo is produced at $nP_T + \zeta_n$ where P_T is the sampling period [18]. In this research effort, a random subset of pulses will be used.

The measurement model in [18] can be written as

$$\tilde{\mathbf{s}} = \mathbf{R}_S \mathbf{M} \mathbf{x} + \boldsymbol{\eta} \quad (17)$$

where \mathbf{R}_S is the slow-time restriction operator that chooses $M_s \leq N_s$ random slow-

time samples, and $\mathbf{M} = [\mathbf{M}_1, \dots, \mathbf{M}_{N_s}]^T$ is the observation matrix that maps the reflectivity profile to sampled measurements, $\mathbf{x} \in \mathbb{C}^{N_r N_\phi \times 1}$ is the vectorized reflectivity profile, and $\tilde{\mathbf{s}} = [\mathbf{s}_1, \dots, \mathbf{s}_{N_s}]^T$ is the undersampled, vectorized phase histories where each \mathbf{s}_i is the fast-time samples at the observation angle ϕ_i [18]. In [18], it was shown that perfect reconstruction could occur using only 40% of the original data. It should be noted that using a random subset of slow-time pulses could cause issues for anisotropic targets; however, a treatment of extended scatterers in the undersampling model is beyond the scope of this dissertation. There are two other papers on sub-Nyquist SAR that seem to achieve the compression in a similar way, namely [15] and [16]. The method in [15] seems closer to compression than compressive sensing as it reduces the number of echos after measurement. The method in [16] appears rather similar to the method in [17, 18], but with some structure to the randomness. For this research effort, we will focus on the combination of the methods in [59, 60] and [17, 18, 62]. In Chapter 5, fast-time undersampling, slow-time undersampling, and polarimetric undersampling will be combined into one, highly compressed PolSAR model.

2.3 Antenna Design Background

Antennas are a critical part of any radar system. Antennas are required to transmit and receive the pulses that then get measured and manipulated by the radar and signal processing system. In order to operate efficiently and effectively, the antenna must be carefully designed around a set of desired parameters [72]. In order to discuss the design and performance of an antenna, those parameters must be defined.

Figure 11 shows the usual geometry used when discussing antennas. When an antenna radiates electromagnetic energy to transmit a signal, the properties of that radiation are described as the antenna's *radiation pattern* [73]. The full radiation

When testing linearly polarized antennae, it is common to describe the performance in terms of principle planes, also called E-plane and H-plane patterns [73]. In terms of measurements, patterns cuts are taken along lines of constant θ and ϕ in spherical coordinates. To relate constant θ and ϕ cuts to the principal plane cuts, the beam axis must lie in either the equator ($\theta = 90^\circ$) or one of the poles ($\theta = 0^\circ$ or $\theta = 180^\circ$) of the spherical coordinate system defined with respect to a physical surface on the antenna [75]. Since the E-plane defines the direction of the polariza-

tion [51, 73], the orientation of the antenna in the test chamber will determine how the E-plane and H-plane are related to the θ cut and ϕ cut.

Another important design and measurement metric is known as the S-parameters. The scattering matrix formed by the S-parameters completely describes an RF network as seen at its ports [76]. Specifically, the S-parameters relate incident voltage waves to reflected voltage waves at the ports [76]. The S-parameters are given in terms of S_{ij} , representing the amount of power received at port i relative to the power input at port j with all other ports terminated in a matched load. Of particular importance is the S_{11} parameter, which is also known as the reflection coefficient [76]. The reflection coefficient (or Γ_{11}) relates how much of the power delivered to port 1 is reflected back, thus a low S_{11} shows that most of the power is radiated from and/or absorbed by the antenna and very little is reflected back. The S-parameters are measured using a vector network analyzer, which displays the S-parameters as a function of frequency. For an antenna to be considered well matched, the S_{11} parameter would ideally be lowest (≤ -15 dB) at the designed center frequency and low (≤ -10 dB) over the desired bandwidth (Jeff Massman, personal communication, July 2021).

For a 2-port antenna, such as a dual polarized antenna, the S_{21} and S_{12} parameters can give insight into the amount of crosstalk in the antenna design. A high S_{21} parameter is indicative of a large amount of power transferring from port 1 to port 2. While the actual crosstalk performance of the antenna will be determined by the realized gain of the θ and ϕ cut patterns at boresight, the S-parameters can provide some intuition on the crosstalk performance during the design process. The realized gain accounts for losses in the model (such as the S-parameters) and correlates to the gain value that is measured when testing a physical antenna.

2.3.1 Typical Spotlight SAR Antenna Types.

The two most common types of radar antennas are phased array antennas and reflector antennas [20]. In order to keep the antenna beam pattern focused on the same point for a collection run, a spotlight SAR antenna must either be mechanically or electronically steered to face to scene center [77]. With the use of mechanical steering, both reflector and phased array antennas are able to be used for spotlight SAR. The choice of antenna type is driven by the platform's size and capabilities. Typically airborne applications have fewer restrictions due to the size of the platform, but for satellites and small unmanned aerial vehicles, phased arrays are the usual choice [77]. The microstrip patch antenna is one of the most common elements in phase array design due to their low cost and ease of manufacture [78]. Due to its low cost, ease of manufacture, and prevalence in SAR systems, a microstrip antenna is chosen for the proof-of-concept antenna design in Chapter IV. Design of a phased array is more complicated and expensive [78, 79] and is beyond the scope of this research effort, so a single element is chosen.

2.3.2 Microstrip Antenna Design Background.

Low profile, light weight, and easy, accurate fabrication make microstrip antennae popular choices for many applications [80]. First conceived in 1953, microstrip antennas did not start receiving attention until the 1970s [73]. Depending on mode selection, microstrip antennas can operate in both side- and end-fire radiation modes [73]. By arranging microstrip antennae in an array configuration, beam pattern synthesis, electronic beam scanning, and increased directivity are possible [73, 78].

At the most basic level, a microstrip antenna is a combination of a radiating patch and a ground plane separated by a type of dielectric substrate. While the radiating patch can take on numerous different shapes to suit different properties [81–88], the

most basic example is the rectangular patch of width W and length L , separated from the ground plane by a substrate of height h [79]. Given a substrate with relative permittivity ϵ_r the length, width and height are usually designed by

$$\begin{aligned} L &< \lambda_0/2\sqrt{\epsilon_r} \\ W &< \lambda_0/\sqrt{\epsilon_r} \\ h &\cong \lambda_0/100 \end{aligned} \tag{18}$$

where λ_0 is the free-space wavelength of the design frequency [89]. Figure 12 shows the usual geometry of the standard rectangular patch microstrip antenna. The radiating edges are separated a distance L and the non-radiating edges are separated by W [79]. Common feed methods are 50Ω feed pin, direct-feed microstrip transmission line, aperture coupling, and transmission line inductance [73]. In all feed methods, feed line thickness, feed inset, aperture shaping, or other techniques must be used to match the impedance of the feed method to the input impedance of the the antenna [73,79]. Figure 12 shows an example of a pin-fed, single-polarized microstrip antenna design to demonstrate the basic layout of a microstrip antenna.

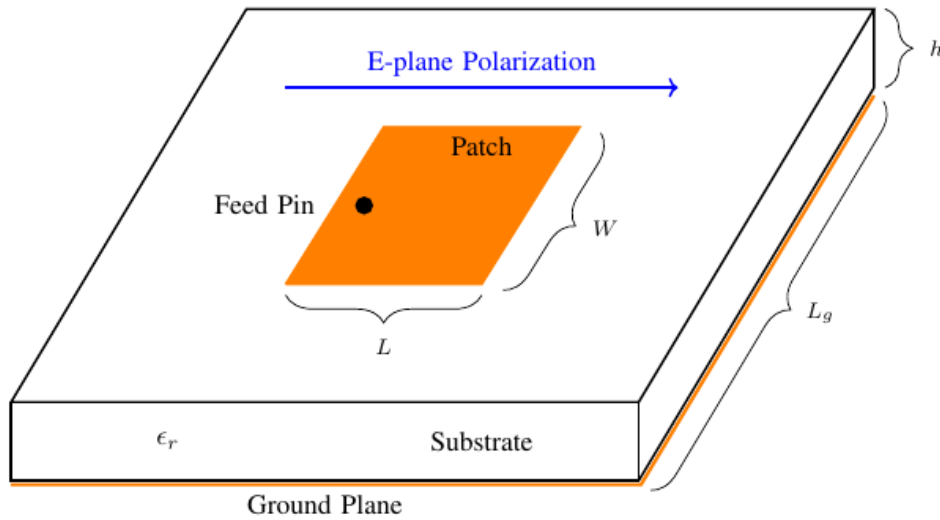


Figure 12. Sample layout of microstrip antenna

Patch antennas typically have broad patterns with a beam area (Ω_A) of about π steradians and a directivity (D) of 4 [89]. For comparison, the horn antenna is another common radar antenna type. A typical horn antenna directivity is in the teens with much sharper beam areas [73, 89]. The directivity and beam area of microstrip antennas can be improved using an array configuration [73]. The bandwidth of a patch antenna is approximated as

$$B \approx \frac{f_r}{Q} \approx \frac{4f_r^2 h}{c\sqrt{\epsilon_e}}, \quad (19)$$

where the quality factor Q is defined as

$$Q = \frac{c\sqrt{\epsilon_e}}{4f_r h}, \quad (20)$$

with f_r as the resonant frequency, and ϵ_e as the effective dielectric constant of the substrate [80]. The location of the feed port determines the polarization orientation of a rectangular microstrip antenna, as shown in Figure 12. Dual polarization can be achieved via orthogonal feed points as shown in Figure 13.

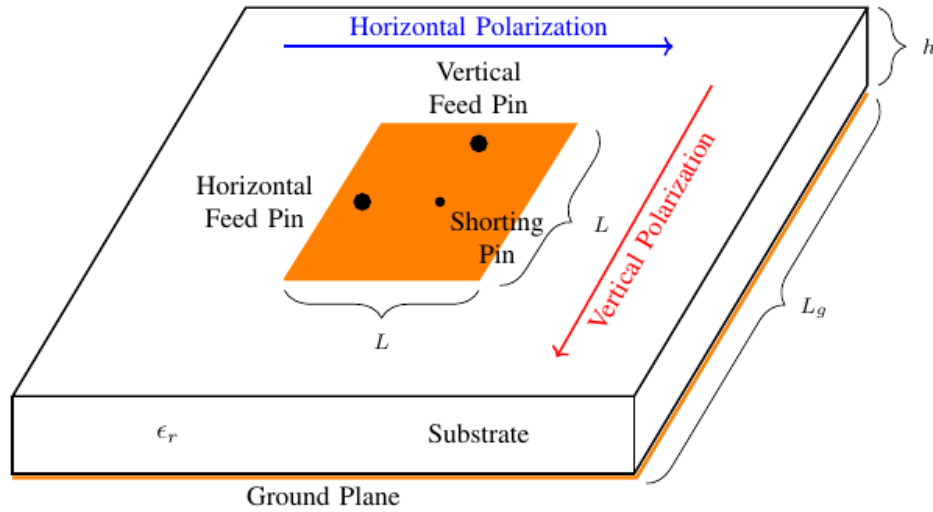


Figure 13. Sample layout of a dual-pol microstrip antenna

2.3.3 Antenna Crosstalk.

An important parameter for this research effort is the system crosstalk, which is assumed to be solely caused by the antenna. The total system crosstalk can be decomposed into the crosstalk caused by the transmit and receive antenna as

$$\mathbf{C} = \mathbf{C}_T \otimes \mathbf{C}_R^T \quad (21)$$

where

$$\mathbf{C}_T = \begin{bmatrix} t_{HH} & t_{HV} \\ t_{VH} & t_{VV} \end{bmatrix} \quad (22)$$

is the transmit antenna's crosstalk matrix. For a monostatic assumption, the transmit and receive crosstalk matrices are assumed to be equal ($\mathbf{C}_T = \mathbf{C}_R$). In order to translate signal processing crosstalk values to antenna measurement parameters, let Port 1 correspond to the Horizontal Pin and Port 2 be the Vertical Pin in Figure 13. The S-parameters can provide a basic idea of the crosstalk performance by looking at the S_{21} and S_{12} parameters. For example, if S_{21} is high then a large amount of the V channel is cross contaminating into the H channel.

To get the actual matrix values for \mathbf{C}_T , the boresight ($\theta = 90^\circ$, $\phi = 0^\circ$) realized gain value is used. The boresight measurement is chosen to avoid angular-dependent crosstalk definitions [90] for simplicity of the model. Since polarization is determined by the orientation of the E-field, the E-field measurements will determine the values in \mathbf{C}_T .

To measure the gain values, the test antenna is placed in a chamber and set to transmit a known signal. A calibrated, dual-pol antenna is used to receive the signal and a port network analyzer connected to the calibrated receiving antenna reports

the values. Thus, the transmit crosstalk matrix can be re-written as

$$\mathbf{C}_T = \begin{bmatrix} t_{HH} & t_{HV} \\ t_{VH} & t_{VV} \end{bmatrix} = \begin{bmatrix} \text{Port 1 co-pol} & \text{Port 1 x-pol} \\ \text{Port 2 x-pol} & \text{Port 2 co-pol} \end{bmatrix} \quad (23)$$

where Port 1 co-pol is the boresight, realized E-field gain transmitted by the test antenna's Horizontal port and received by the Horizontal port of the receiving antenna. Port 1 x-pol is then the boresight, realized E-field gain that is measured by the receiving antenna when the test antenna is set to transmit from the Horizontal port. Naturally, when the test antenna is set to transmit from the Vertical port then Port 2 co-pol is the E-field gain measured by the receiving antenna's Vertical port and Port 2 x-pol is the E-field gain measured by the receiving antenna's Horizontal port. Chapter 4 shows the specific design process of a pin-fed, dual-polarized, high-crosstalk microstrip antenna based on the results found in Chapter 3. Chapter 4 then details the construction and measurement of a prototype antenna and compares the modeled values with the real, measured values.

III. Dropped-Channel PolSAR CS Model Robustness

Recent works [5–8] have applied CS to the PolSAR problem in the polarimetric domain. In [5–8], Jackson and Lee-Elkin showed that by using antenna crosstalk information and CS techniques, it is possible to omit processing of an entire polarimetric channel and recover the channel information afterwards from the system crosstalk information present in the remaining channels. This dissertation provides an analysis of the crosstalk levels over which Jackson and Lee-Elkin’s PolSAR model can provide acceptable recovery performance in order to help determine potential system tolerances. We use Monte Carlo trials over random scenes, as well as simulated scenes based on the GOTCHA data set [29] to show recovery performance via Basis Pursuit Denoising (BPDN) [4] at different crosstalk levels. By determining the levels of crosstalk over which the dropped-channel PolSAR CS model is effective, we can better estimate the need for a novel antenna design. Additionally, by identifying a region of crosstalk levels that produce accurate recovery results, we ease the burden of a future antenna design problem.

There are many CS approaches to reduce data in SAR systems. Some compress in the fast and slow time dimension [9,10,12,15–18,53]. Others perform super resolution (SR) of the SAR image [91,92] which theoretically lowers data requirements in relation to a higher resolution system. Works [9,10,12,15–18,53,91,92] are assumed to operate on a single channel; however, applying SAR CS to channels individually could alter polarimetric ratios. Previous efforts for PolSAR also look at fast and slow time sampling strategies such as in [93]. Others such as [94, Ch. 7] assume each channel has the same sparsity support, which is not necessarily true. To maintain integrity of the SAR model, we need to process all polarimetric channels together. Prior to Jackson and Lee-Elkin’s work [5–7], using CS to reduce number of measured polarimetric channels had not been considered.

The dropped-channel PolSAR model from [5–8] relies on system crosstalk; however, PolSAR systems are normally designed to have good isolation between channels to mitigate the crosstalk [95,96]. Real-world crosstalk levels are typically higher than the design goal [97], sometimes up to -10 dB [98], which may enable dropped-channel PolSAR. The typical design goals of PolSAR systems and the variability in current systems and antennas leads us to ask, over what range of crosstalk values does Jackson and Lee-Elkin’s method work? The goal of this chapter is to determine how robust the dropped-channel PolSAR CS method from [7,8] is to various levels of crosstalk.

3.1 Dropped-Channel PolSAR CS

The dropped-channel PolSAR CS model [7,8], as the name implies, drops a polarimetric channel from the receiver processing chain but estimates the data using sparse recovery techniques. In a PolSAR system, the signal is immediately contaminated with antenna crosstalk on both transmission and reception, prior to a channel drop operation. Channel dropping occurs prior to analog-to-digital conversion (ADC), enabling hardware and computational savings in the receiver. Since the dropped information is still received by the antenna in the form of crosstalk, CS techniques are able to recover the unprocessed channel.

Begin by assuming a sparse, vectorized input of unknown scene reflectivities $\mathbf{x}_m \in \mathbb{C}^{N_p N_x N_y \times 1}$ accounting for $N_x \times N_y$ total sub-pixels over N_p polarization channels [7,8]. Further assume the scene reflectivity is corrupted by random clutter $\mathbf{w} \in \mathbb{C}^{N_p N_s N_r \times 1}$. The combination of unknown reflectivities and clutter is then mapped to a vectorized stack of $M_p < N_p$ images output $\mathbf{y}_m \in \mathbb{C}^{M_p M_x M_y \times 1}$ consisting of $M_x \times M_y$ pixels per polarization channel.

The measurement model from [7, 8] is written as

$$\mathbf{y} = (\mathbf{J}\mathbf{C} \otimes \mathbf{A}_1)(\mathbf{x} + \mathbf{w}) \quad (24)$$

$$= (\mathbf{J}\mathbf{C} \otimes \mathbf{A}_1)(\mathbf{P} \otimes \mathbf{S})\mathbf{b} + \tilde{\mathbf{w}} \quad (25)$$

$$= \mathbf{A}\mathbf{b} + \tilde{\mathbf{w}} \quad (26)$$

where

$$\tilde{\mathbf{w}} = (\mathbf{J}\mathbf{C} \otimes \mathbf{A}_1)\mathbf{w} \quad (27)$$

is the imaged clutter and

$$\mathbf{A} = (\mathbf{J}\mathbf{C} \otimes \mathbf{A}_1)(\mathbf{P} \otimes \mathbf{S}) \quad (28)$$

is the measurement matrix, comprised of the imaging matrix times the dictionary.

The scene reflectivity, as in [7, 8, 63], is defined as

$$\mathbf{x} = (\mathbf{P} \otimes \mathbf{S})\mathbf{b} \quad (29)$$

where $\mathbf{P} \in \mathbb{C}^{N_p \times Q}$ is a dictionary of Q possible polarization responses, $\mathbf{S} \in \mathbb{C}^{N_x N_y \times S'}$ is a dictionary of S' spatial responses, and $\mathbf{b} \in \mathbb{C}^{Q S' \times 1}$ is a coefficients vector. If the scene also contained extended targets, an extended spatial dictionary like the one defined in [63] could be used. As long as the spatial dictionary is well matched to the expected targets in the scene, the coefficients vector \mathbf{b} can be represented sparser than by assuming all targets are sums of point targets. For this dissertation, we will use a point target spatial dictionary $\mathbf{S} = \mathbf{I}_{N_x N_y}$ and let the Pauli basis be used for \mathbf{P} . Since all targets are assumed to be point targets, an identity matrix is a well-matched spatial dictionary.

The imaging matrix in (24) is comprised of the channel selection matrix \mathbf{J} , the channel crosstalk matrix \mathbf{C} , and the single channel measurement matrix \mathbf{A}_1 which

performs 2D convolution of the scene reflectivity \mathbf{x} with the radar PSF. The version of the dropped-channel PolSAR model in (24) assumes that each channel has the same PSF. Matrix \mathbf{J} starts as an $N_p \times N_p$ identity matrix, with each row representing a channel. To drop a channel, the corresponding row is removed leaving an $M_p \times N_p$ channel selection matrix.

At the heart of the model is the $N_p \times N_p$ channel coupling matrix \mathbf{C} , which captures crosstalk that occurs at both the transmit and receive antennas as well as over the transmit/receive hardware channels. The information contained in the crosstalk is vital to the success of the CS technique in recovering the dropped channel. As in [7, 8], we assume that the coupling is not dependent on frequency, time, or angle for computational simplicity. Further, we assume a monostatic system. Since we are primarily interested in the crosstalk level, we introduce a slight notational change from [7, 8], inspired by Van Zyl's crosstalk model [1, 98, 99]. The transmit crosstalk matrix can then be written as

$$\mathbf{T} = \begin{bmatrix} t_{HH} & \delta_1 \\ \delta_2 & t_{VV} \end{bmatrix} \quad (30)$$

where δ_1 and δ_2 are the crosstalk parameters. We then normalize the total power of each channel such that $|t_{HH}|^2 + |\delta_1|^2 = 1$ and $|\delta_2|^2 + |t_{VV}|^2 = 1$ for conservation of power as in [7, 8].

We can now build the composite system crosstalk matrix as

$$\mathbf{C} = \mathbf{T} \otimes \mathbf{R}^T \quad (31)$$

$$= \mathbf{T} \otimes \mathbf{T}^T \quad (32)$$

$$= \begin{bmatrix} \frac{t_{HH}}{\|\mathbf{t}_1\|_2} & \frac{\delta_1}{\|\mathbf{t}_1\|_2} \\ \frac{\delta_2}{\|\mathbf{t}_2\|_2} & \frac{t_{VV}}{\|\mathbf{t}_2\|_2} \end{bmatrix} \otimes \begin{bmatrix} \frac{t_{HH}}{\|\mathbf{t}_1\|_2} & \frac{\delta_1}{\|\mathbf{t}_1\|_2} \\ \frac{\delta_2}{\|\mathbf{t}_2\|_2} & \frac{t_{VV}}{\|\mathbf{t}_2\|_2} \end{bmatrix}^T \quad (33)$$

$$= \begin{bmatrix} \frac{t_{HH}^2}{\|\mathbf{t}_1\|_2^2} & \frac{\delta_2}{\|\mathbf{t}_2\|_2} \frac{t_{HH}}{\|\mathbf{t}_1\|_2} & \frac{\delta_1 t_{HH}}{\|\mathbf{t}_1\|_2^2} & \frac{\delta_1}{\|\mathbf{t}_1\|_2} \frac{\delta_2}{\|\mathbf{t}_2\|_2} \\ \frac{\delta_1 t_{HH}}{\|\mathbf{t}_1\|_2^2} & \frac{t_{HH}}{\|\mathbf{t}_1\|_2} \frac{t_{VV}}{\|\mathbf{t}_2\|_2} & \frac{\delta_1^2}{\|\mathbf{t}_1\|_2^2} & \frac{\delta_1}{\|\mathbf{t}_1\|_2} \frac{t_{VV}}{\|\mathbf{t}_2\|_2} \\ \frac{t_{HH}}{\|\mathbf{t}_1\|_2} \frac{\delta_2}{\|\mathbf{t}_2\|_2} & \frac{\delta_2^2}{\|\mathbf{t}_2\|_2^2} & \frac{t_{HH}}{\|\mathbf{t}_1\|_2} \frac{t_{VV}}{\|\mathbf{t}_2\|_2} & \frac{\delta_2 t_{VV}}{\|\mathbf{t}_2\|_2^2} \\ \frac{\delta_1}{\|\mathbf{t}_1\|_2} \frac{\delta_2}{\|\mathbf{t}_2\|_2} & \frac{\delta_2 t_{VV}}{\|\mathbf{t}_2\|_2^2} & \frac{\delta_1}{\|\mathbf{t}_1\|_2} \frac{t_{VV}}{\|\mathbf{t}_2\|_2} & \frac{t_{VV}^2}{\|\mathbf{t}_2\|_2^2} \end{bmatrix} \quad (34)$$

where \otimes represents the Kronecker product, and $\|\mathbf{t}_1\|_2$ and $\|\mathbf{t}_2\|_2$ represent the ℓ_2 norm of the first and second rows of \mathbf{T} , respectively. Recall the monostatic assumption, allowing us to replace \mathbf{R} with \mathbf{T} in (31).

As in [7, 8], the rows in (34) represent each of the four PolSAR channels. The elements along the diagonal represent the signal response (i.e., HH, HV, etc). The off-diagonal entries represent the channel crosstalk. Thus, the first row represents the HH channel. The first element of the first row represents the signal response. The other three elements represent the amount of HV, VH, and VV coupled into the HH channel.

As in [98], the parameter δ_1 captures the crosstalk when the horizontal polarization is transmitted or received and δ_2 does the same for the vertical polarization. As such, δ_1 and δ_2 will be two of the free parameters in our robustness search grid to identify crosstalk that enables successful compressive sensing of the polarization channel dimension. Since phase crosstalk is difficult to design in an antenna system [75], we limit \mathbf{C} to real values for an initial system performance analysis. However,

phase crosstalk exists in practice and must be accounted for. We perform a second system analysis with complex \mathbf{C} at selected points of interest identified in the initial performance analysis.

To capture the effects of the radar imaging system on the scene reflectivity, point spread functions (PSFs) are used. Specifically, the single channel, 2D point spread convolution operator matrix $\mathbf{A}_1 \in \mathbb{C}^{M_s M_r \times N_s N_r}$ is a block diagonal matrix that performs a 2D convolution via matrix multiplication. As in [7], all channels are assumed to have the same PSF. In the interest of determining the recovery robustness of the model, we vary \mathbf{A}_1 based on three different point spreads. Each point spread corresponds to a different SAR aperture extent in degrees. As in [64], when a smaller angular extent is used, we over-sample the PSF in the azimuth direction to keep the size of \mathbf{A}_1 consistent without changing the cross-range resolution. For this work, a 10 degree angular extent is assumed to represent the $N_s N_r$ subpixels. As such, the 2.5 and 5 degree PSFs are over-sampled by a factor of 4 and 2 respectively to keep the total size of the \mathbf{A}_1 matrices equal. Note that bandwidth variations are not addressed or assumed, however the effects would be similar. The reader is referred to [64] for a treatment of bandwidth variations related to the dropped-channel PolSAR model. The PSF variations for three different aperture extents are shown in Figure 14.

By assuming that the scene reflectivity is spatially sparse, efficient CS techniques can recover the dropped channel. Since radar measurements are contaminated by clutter, basis pursuit denoising (BPDN) can both recover the dropped channel and remove the clutter. The BPDN problem is

$$\hat{\mathbf{b}} = \arg \min_{\mathbf{b}} \|\mathbf{b}\|_1 \text{ s.t. } \|\mathbf{y} - (\mathbf{J}\mathbf{C} \otimes \mathbf{A}_1)(\mathbf{P} \otimes \mathbf{S})\mathbf{b}\|_2 \leq \epsilon \quad (35)$$

where ϵ is an error tolerance value. We solve (35) using the `spg11` algorithm [100,101]. As in [7], we set the BPDN error radius ϵ to ensure that the ϵ ball contains the ℓ_2

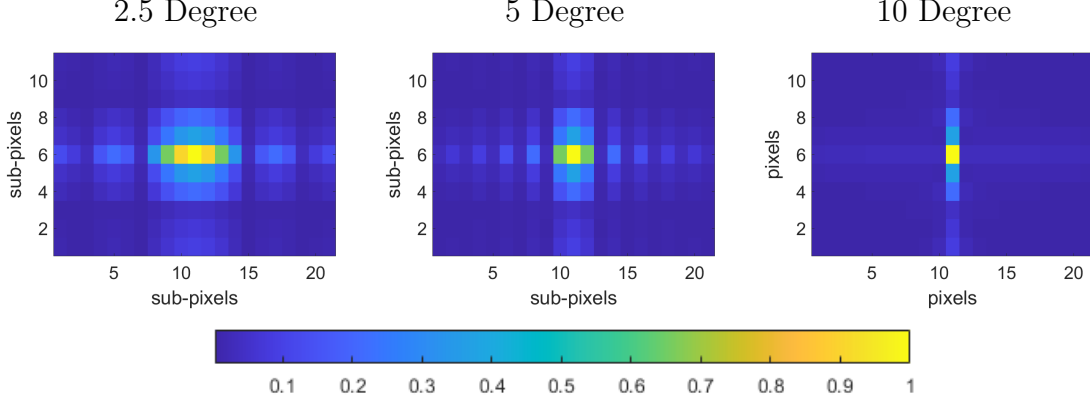


Figure 14. PSF for 2.5°, 5°, and 10° apertures, corresponding to 36.99 cm, 18.49 cm, and 9.25 cm cross-range resolution for center frequency 9.2881 GHz and grazing angle 0°.

norm of the imaged clutter $\tilde{\mathbf{w}}$ with a 95% probability.

In order to guarantee recovery, measurement matrix \mathbf{A} should satisfy the restricted isometry property (RIP) [4]. Unfortunately, the RIP is nearly impossible to verify in deterministic measurement matrices [102]. A common replacement metric for the RIP is mutual coherence, defined as

$$\mu_{\mathbf{A}} = \max_{1 \leq i \neq j \leq N_p N_s N_r} |\mathbf{a}_i^H \mathbf{a}_j|, \quad (36)$$

where $\mathbf{a}_1, \dots, \mathbf{a}_{N_p N_s N_r} \in \mathbb{C}^{N_p N_s N_r}$ are the normalized columns of the measurement matrix \mathbf{A} [4]. A small coherence has been shown to guarantee the recovery of basis pursuit problems. A key assumption in (36) is that the columns of \mathbf{A} are ℓ_2 -normalized [4]. Due to the underlying structure in (24), normalizing the columns of \mathbf{A} corrupts the point spread function structure. The mutual coherence results are included for completeness in Section III even though the dropped-channel PolSAR model doesn't lend to mutual coherence being a useful metric. Several alternatives were attempted, such as statistical RIP [103], restricted isometry constants (RICs) [4], and various matrix norms. None of these alternatives proved to be useful as a predictive metric of

performance for the PolSAR CS model. Ultimately, a new metric called the Signal-to-Crosstalk Ratio (SXR), is defined in Section 3.2.1 and used for predicting and measuring the performance of the PolSAR CS model.

3.2 Experiment 1: Simulated Point Target Scenes

Previous papers suggest that a high crosstalk may be required for (35) to accurately reconstruct a dropped channel [5–8, 63, 64]. Commercial antennas are typically designed with a goal of low crosstalk [85, 95, 104]. By determining the crosstalk range over which acceptable recovery performance is achieved, we can determine if a novel antenna design is needed. To measure robustness, we will use both simulated data of point target scenes and GOTCHA sub-scenes [29].

3.2.1 Measuring Robustness.

To provide a quantitative look at the robustness of the drop-channel PolSAR CS model, we perform a Monte Carlo trial on random simulated point target scenes. In [7], the simulated scene is fixed and random draws are performed over \mathbf{C} to find a suitable crosstalk matrix. Then a fixed \mathbf{C} is used in an analysis over randomly populated \mathbf{b} vectors. Here, we have a grid of fixed \mathbf{C} matrices and randomize the scene layout and target density level. Scene size and other fixed parameters and their values can be found in Table 1. For each target density level shown in Table 1, we generate 400 random point target scenes at that target density level. The point

targets have a random polarization chosen from the Pauli basis

$$\mathbf{P} = [\mathbf{p}_1, \mathbf{p}_2, \mathbf{p}_3, \mathbf{p}_4] = \frac{1}{\sqrt{2}} \begin{bmatrix} 1 & 1 & 0 & 0 \\ 0 & 0 & 1 & -j \\ 0 & 0 & 1 & j \\ 1 & -1 & 0 & 0 \end{bmatrix}, \quad (37)$$

where $j = \sqrt{-1}$. Each point is chosen to exactly align with one of the Pauli basis vectors. For each scene, we apply the crosstalk $|\delta_i|e^{j\angle\delta_i}$ shown in Table 1 and analyze the performance metrics.

For the point target scenes, performance metrics are the relative error on \mathbf{b}

$$E = \frac{\|\mathbf{b}_{true} - \hat{\mathbf{b}}\|_2^2}{\|\mathbf{b}_{true}\|_2^2}, \quad (38)$$

the mutual coherence, and the signal-to-crosstalk ratio (SXR), defined as

$$SXR = \frac{\sum_{i \in M} |c_{i,i}|^2}{\sum_{i \in M} \sum_{j \in N_p, j \neq i} |c_{i,j}|^2}, \quad (39)$$

where $c_{i,j}$ is the \mathbf{JC} matrix element in the i th row and j th column. The underlying PSF structure of \mathbf{A}_1 makes mutual coherence an unreliable predictive metric, however mutual coherence is included in the results for completeness. We introduce the SXR in (39) as an alternative, predictive metric for the dropped-channel PolSAR model as the SXR can be computed from just the crosstalk matrix.

For the recovery to be a good representation of the true scene, we expect the mean of (38) across the Monte Carlo trials to be low. We consider the results to be acceptable if the average relative error on \mathbf{b} (38) across all Monte Carlo trials of the recovered \mathbf{b} vector is less than or equal to 0.1. For the first experiment, we assume crosstalk is real by using the values labeled $|\delta_i|$ from Table 1 in (34) to form the \mathbf{C}

matrix. However, phase crosstalk will exist in the system. To determine the effects of phase crosstalk, we choose four real crosstalk pairs from the Monte Carlo results that define the borders of the robustness region and apply a grid of phase crosstalk to those select pairs.

Table 1. Simulation Parameters

Parameter	Sample Values
Target Density (%)	[1,2,3,4,5,7,10]
Aperture Extent (°)	[2.5,5,10]
J	$\begin{bmatrix} 0 & 1 & 0 & 0 \\ 0 & 0 & 1 & 0 \\ 0 & 0 & 0 & 1 \end{bmatrix}$
SCR (dB)	40
Scene Size	2.5m x 2.5m (Pt Tgt) 30m x 30m (GOTCHA)
Bandwidth:	622MHz
$ \delta_i $	[0.0126, 0.0200, 0.0316, 0.0501, 0.0794, 0.1259, 0.1995, 0.3162, 0.5012, 0.7943, 0.8913]
$\angle\delta_i$	[0, 0.5712, 1.1424, 1.7136, 2.2848, 2.8560, 3.4272, 3.9984, 4.5696, 5.1408, 5.7120]

3.2.2 Simulated Point Target Results.

The dropped-channel PolSAR model is quite robust over the regions examined. That is, a large portion of the search grid produced average ℓ_2 recovery errors at or below the 0.1 threshold to be considered successful recoveries. A threshold of 0.1 is chosen based on qualitative observations as the point at which more significant errors such as polarimetric shifts and false positives are seen. Further, the results in Section 3.2.2.3 show that inclusion of phase in the crosstalk does not lead to any significant negative impacts. Thus, the antenna design goal is any antenna with the desired magnitude, as any phase is acceptable.

3.2.2.1 Deterministic Results.

To help validate the model and give some insight into expected results in the Monte Carlo trials, three deterministic scenes are used over the range of PSF and $|\delta_i|$ values in Table 1. An initial gauge on the robustness of the model is obtained by looking at the performance metrics over the deterministic scenes. The robustness is then further determined over the next three experiments using Monte Carlo runs on random scenes at different sparsity levels. Figure 15 shows the true reflectivity of each of the three deterministic scenes. Each scene in Figure 15 is designed to test or challenge the dropped-channel PolSAR in some way. Scene 1 is a basic scene to verify recovery, Scene 2 is meant to test PSF blurring in a more complex scene with a higher target density. Scene 3 is specifically designed to challenge the cross-range blurring that occurs at the lower aperture extents. Thus, the combination of a 2.5 degree aperture extent and Scene 3 is the most challenging in this set. These scenes are examined with and without dropping a channel.

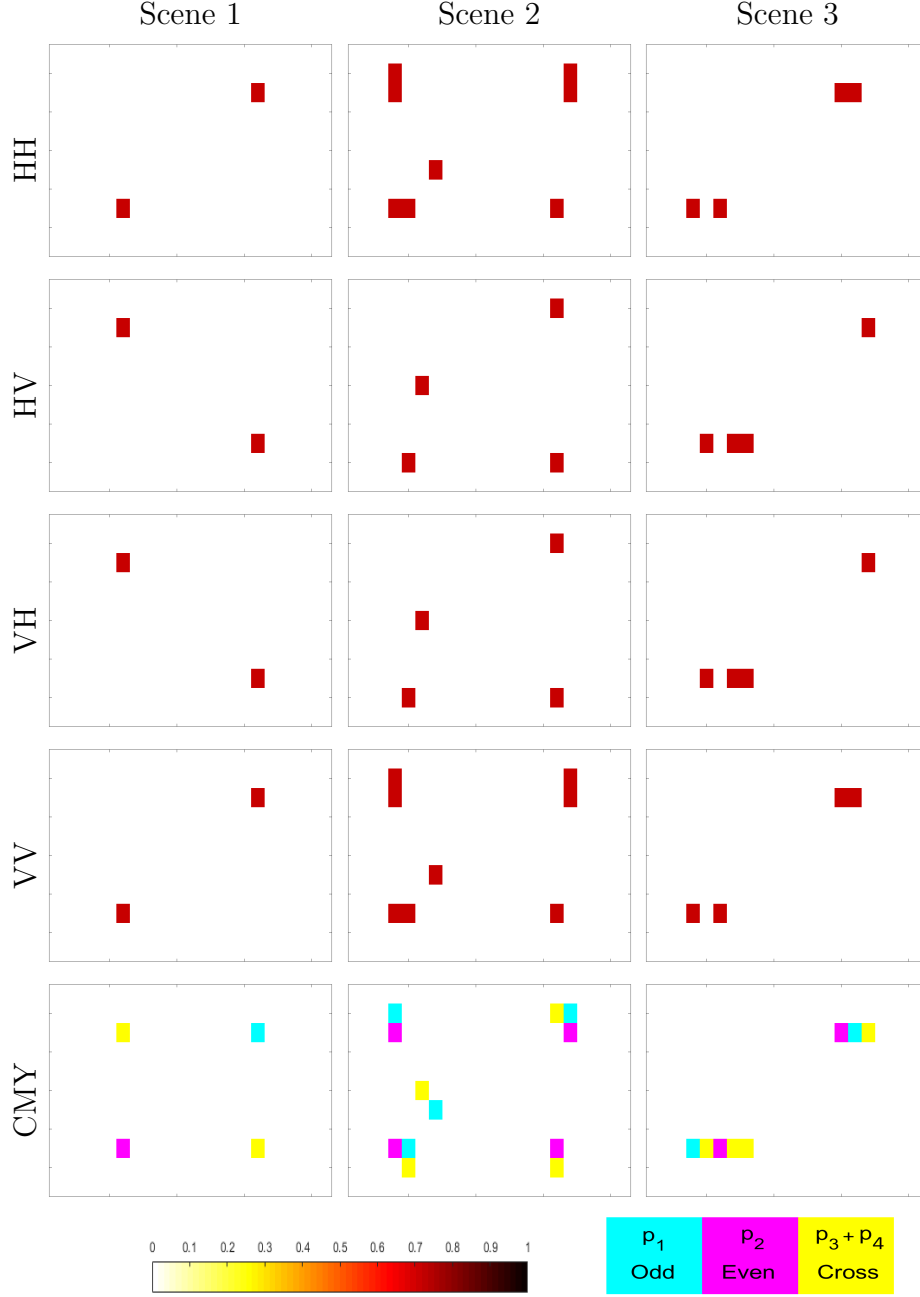


Figure 15. Truth images for all deterministic scenes

Figure 16 shows the error on \mathbf{b} of the recovered reflectivity for each zero-phase crosstalk combination in at each PSF in Table 1 for each scene without a channel drop. The scenes were evaluated without a channel drop first to give an idea of the performance and as a sanity check on the simulation setup. The next set of results will

include the HH channel drop. Figure 17 shows the success rate corresponding to the results in Figure 16. Recall that the recovery is considered successful if the relative error on \mathbf{b} is less than or equal to 0.1. A threshold of 0.1 is chosen based on qualitative observations as the point at which more significant errors such as polarimetric shifts and false positives are seen. Since these scenes are deterministic, no variations in target density are considered and there are no Monte Carlo trials. Since only one iteration is run at each combination, a yellow square represents a success, and a blue square represents a failure.

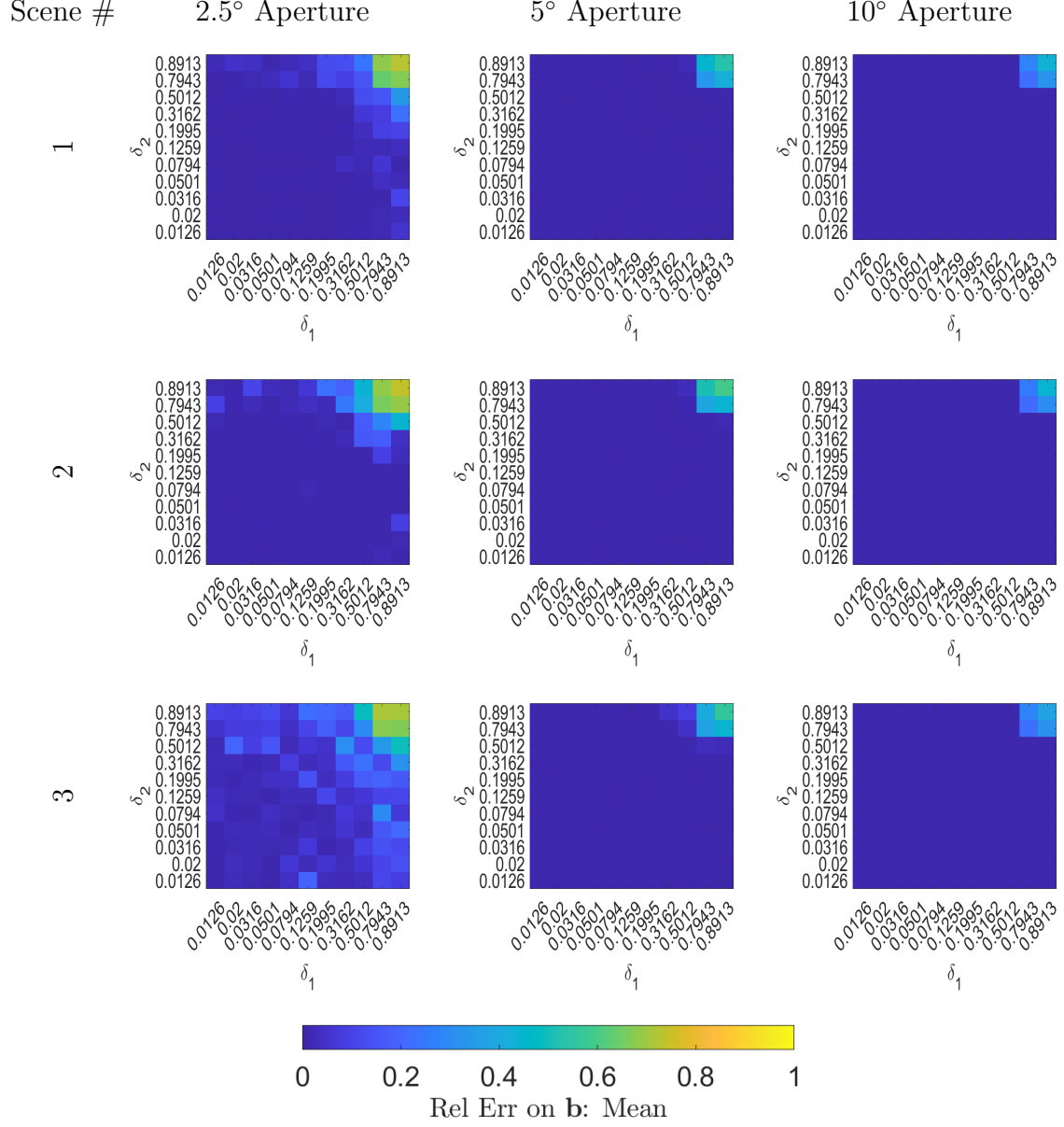


Figure 16. Relative error on b (38) across crosstalk, scene, and PSF combinations for deterministic scenes, no channel dropped.

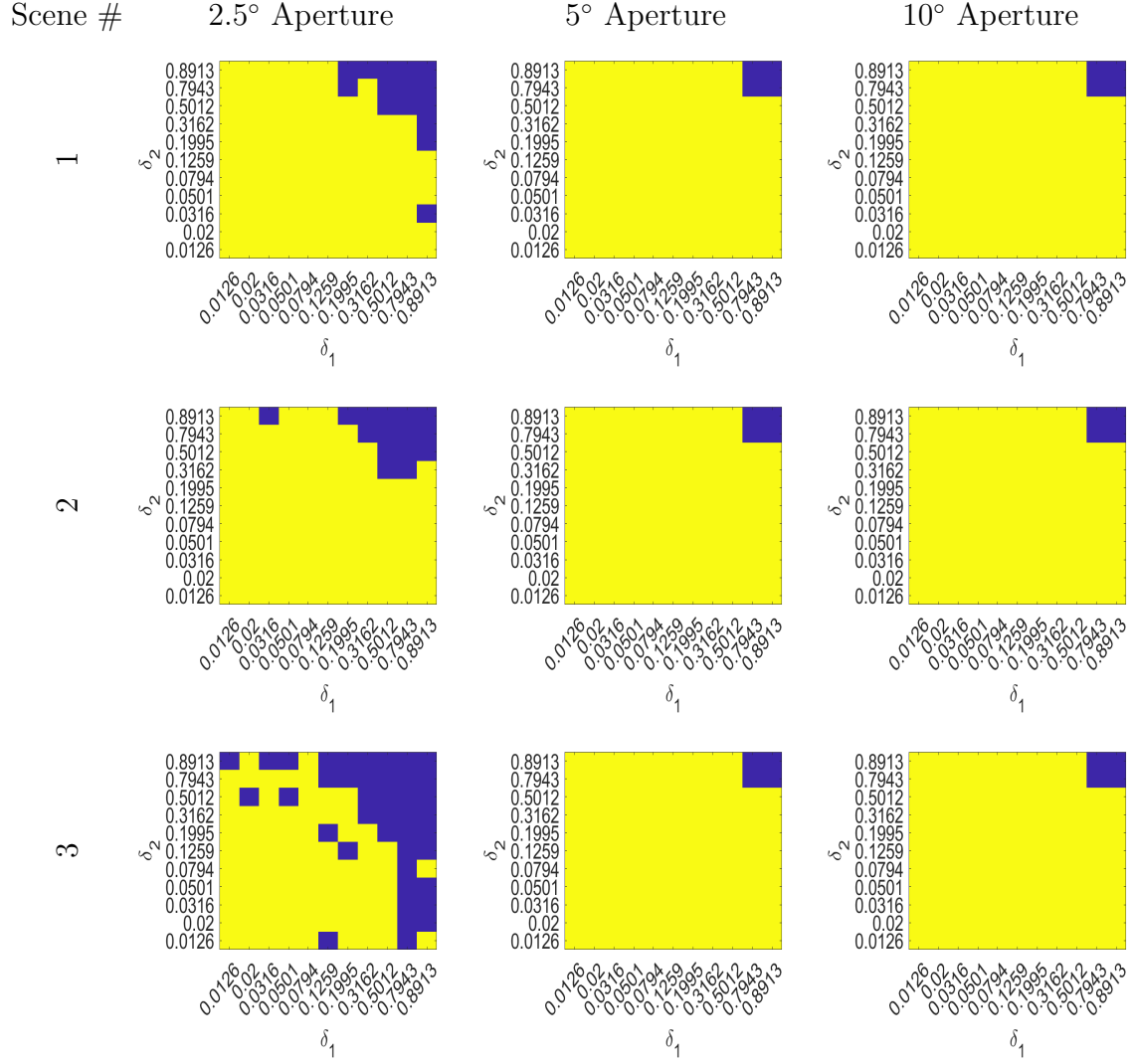


Figure 17. Success rate across crosstalk, scene, and PSF combinations for deterministic scenes, no channel dropped. A yellow square represents a success, and a blue square represents a failure.

The large areas of low relative error on \mathbf{b} in Figure 16 and large amount of yellow in Figure 17 point to large robustness regions. As a sanity check, Figures 18–20 show the truth, observation, and BPDN recovery for Scene 2 in each aperture extent at the middle crosstalk pair, where $\delta_1 = \delta_2 = 0.1995$.

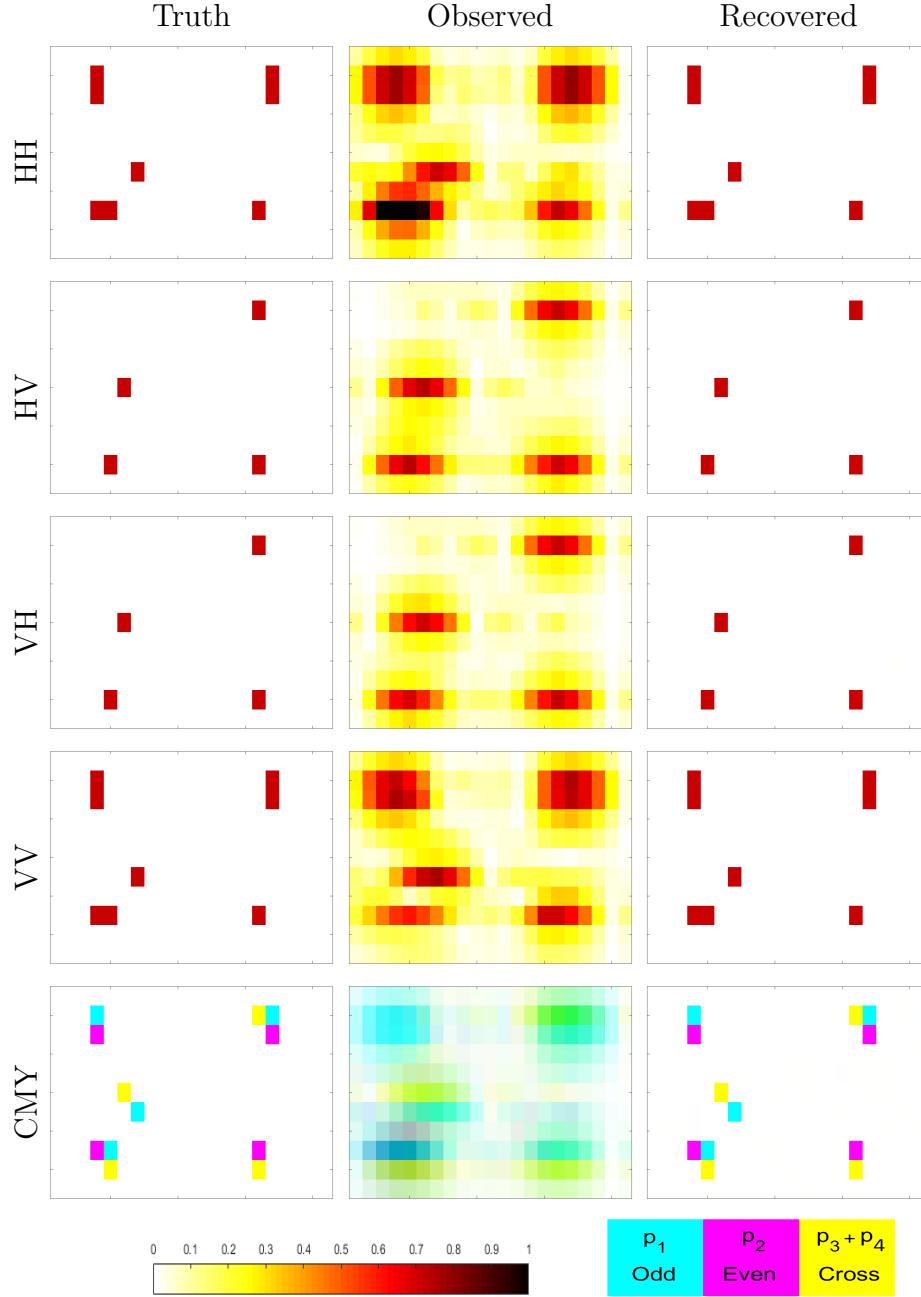


Figure 18. Truth, observed, and recovered scenes for Deterministic Scene 2 using $\delta_1 = \delta_2 = 0.1995$ and a 2.5° aperture extent, no channel dropped

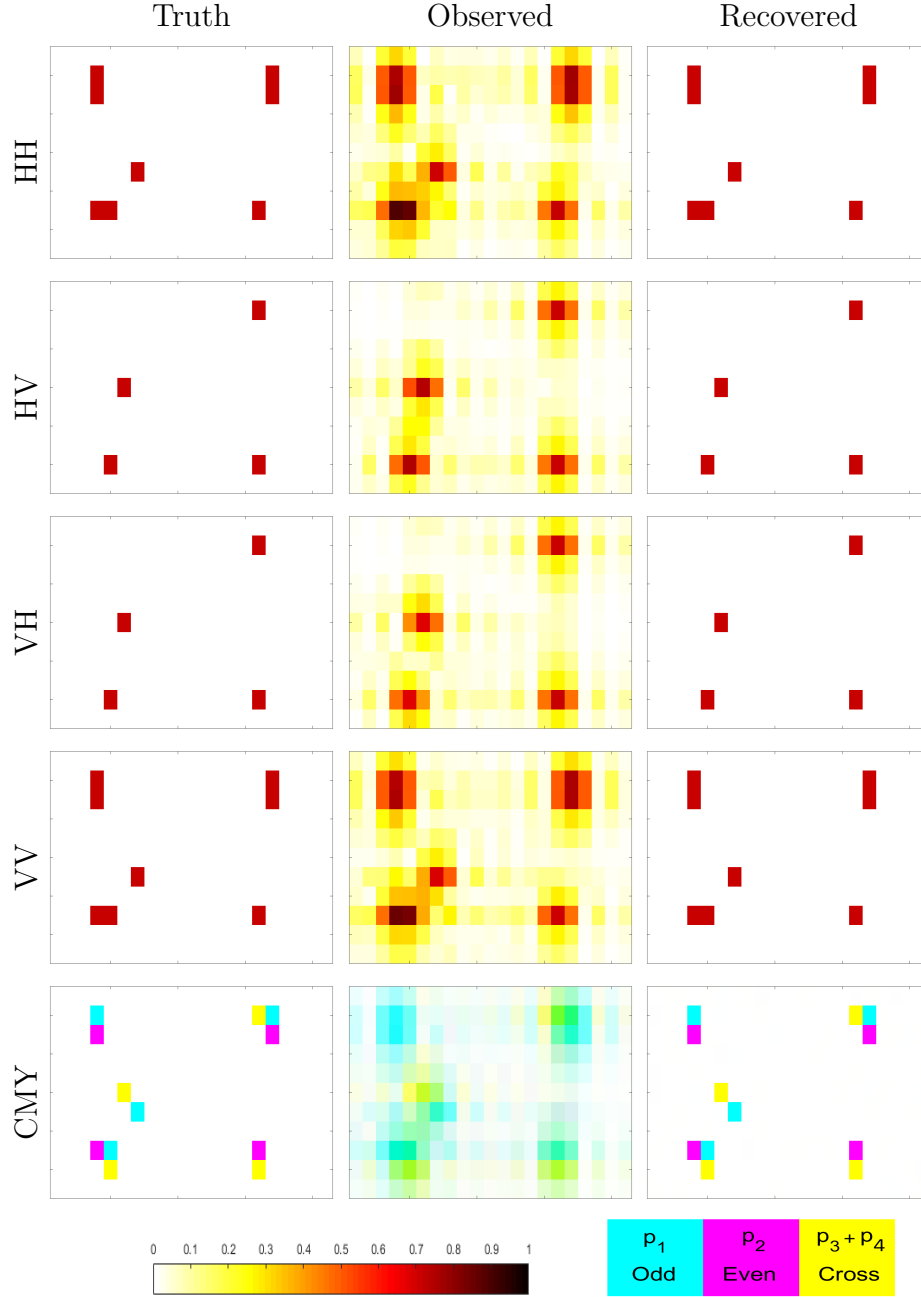


Figure 19. Truth, observed, and recovered scenes for Deterministic Scene 2 using $\delta_1 = \delta_2 = 0.1995$ and a 5° aperture extent, no channel dropped

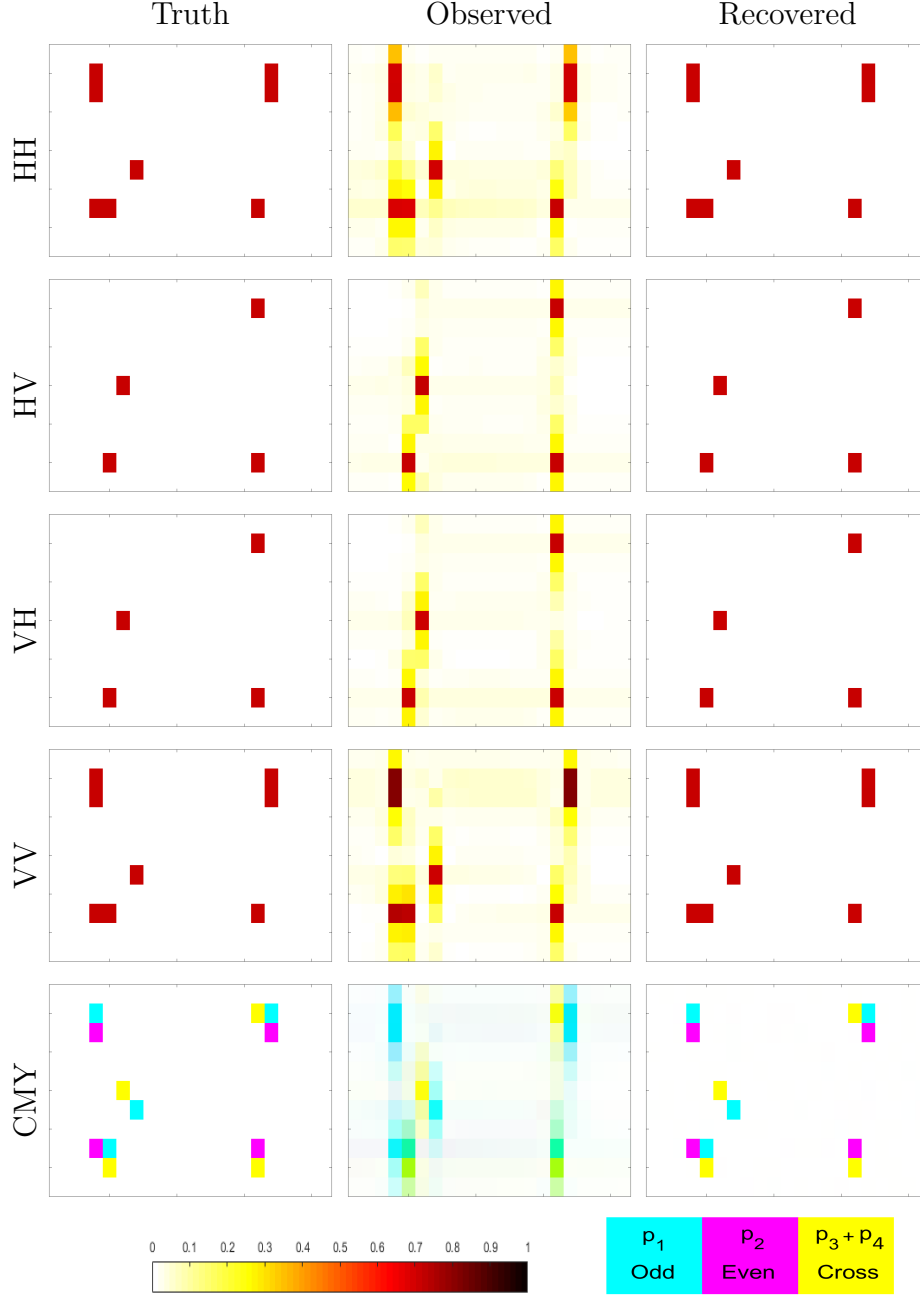


Figure 20. Truth, observed, and recovered scenes for Deterministic Scene 2 using $\delta_1 = \delta_2 = 0.1995$ and a 10° aperture extent, no channel dropped

The results in Figures 18–20 are expected. Despite the heavy blurring from the lower aperture extents, the recoveries are very good. Since no channel is dropped and the SCR is 40 dB, all BPDN really needs to do is deconvolve the PSF. Even still, higher

levels of crosstalk show the ability to over-contaminate the scene, demonstrating that there is an upper bound to the level of crosstalk the dropped-channel PolSAR model can handle under these assumptions.

With the results in Figures 18–20 looking as expected, the next step is to repeat with a channel dropped. The HH channel is chosen for consistency. and the experiment is repeated with the rest of the assumptions remaining the same. Figure 21 shows the relative error on \mathbf{b} across the crosstalk, scene, and PSF combinations. Figure 22 shows the success rate corresponding to Figure 21. As before, yellow is a success and blue is a bust of the threshold.

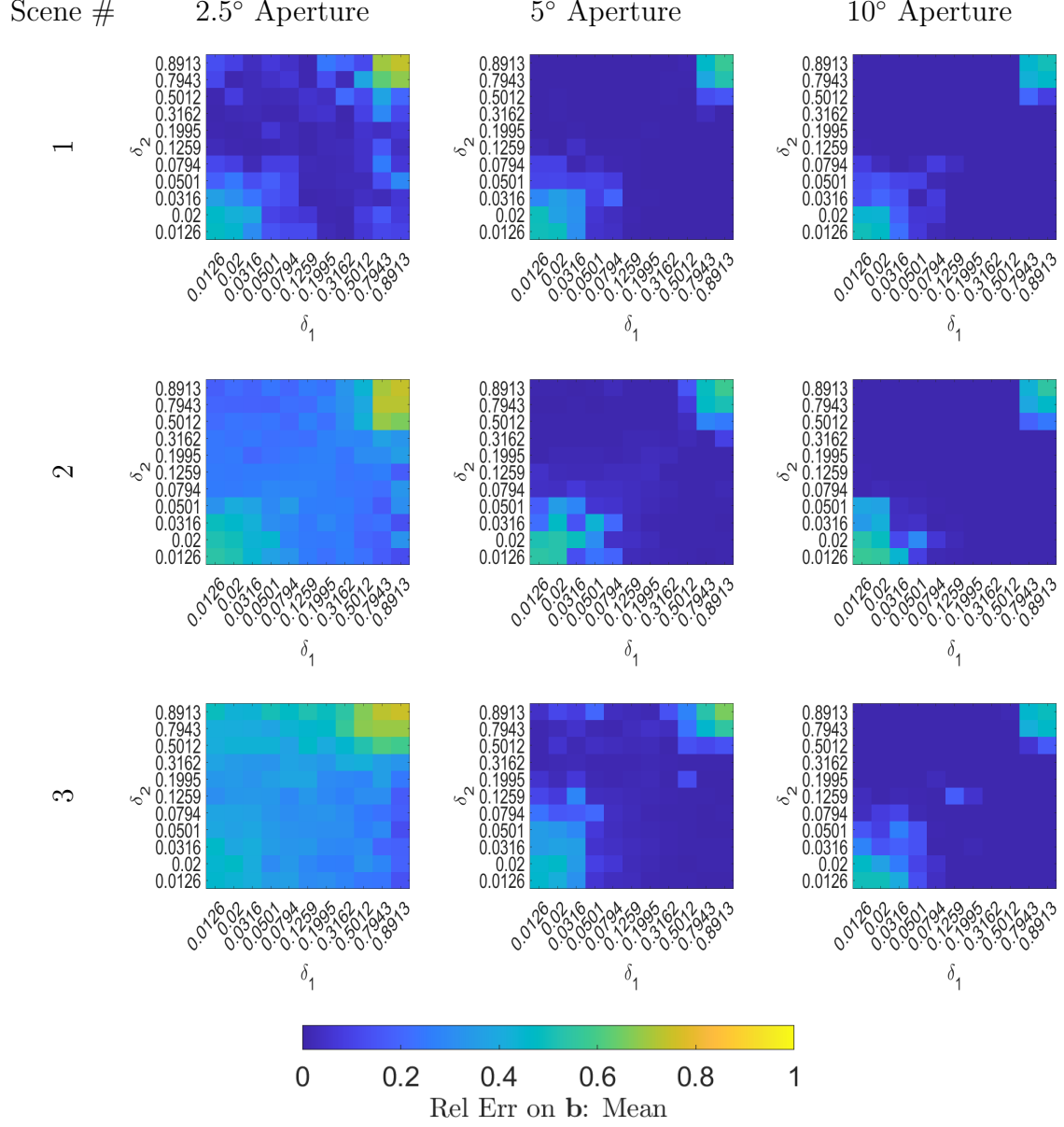


Figure 21. Relative error on b (38) across crosstalk, scene, and PSF combinations for deterministic scenes, HH channel dropped.

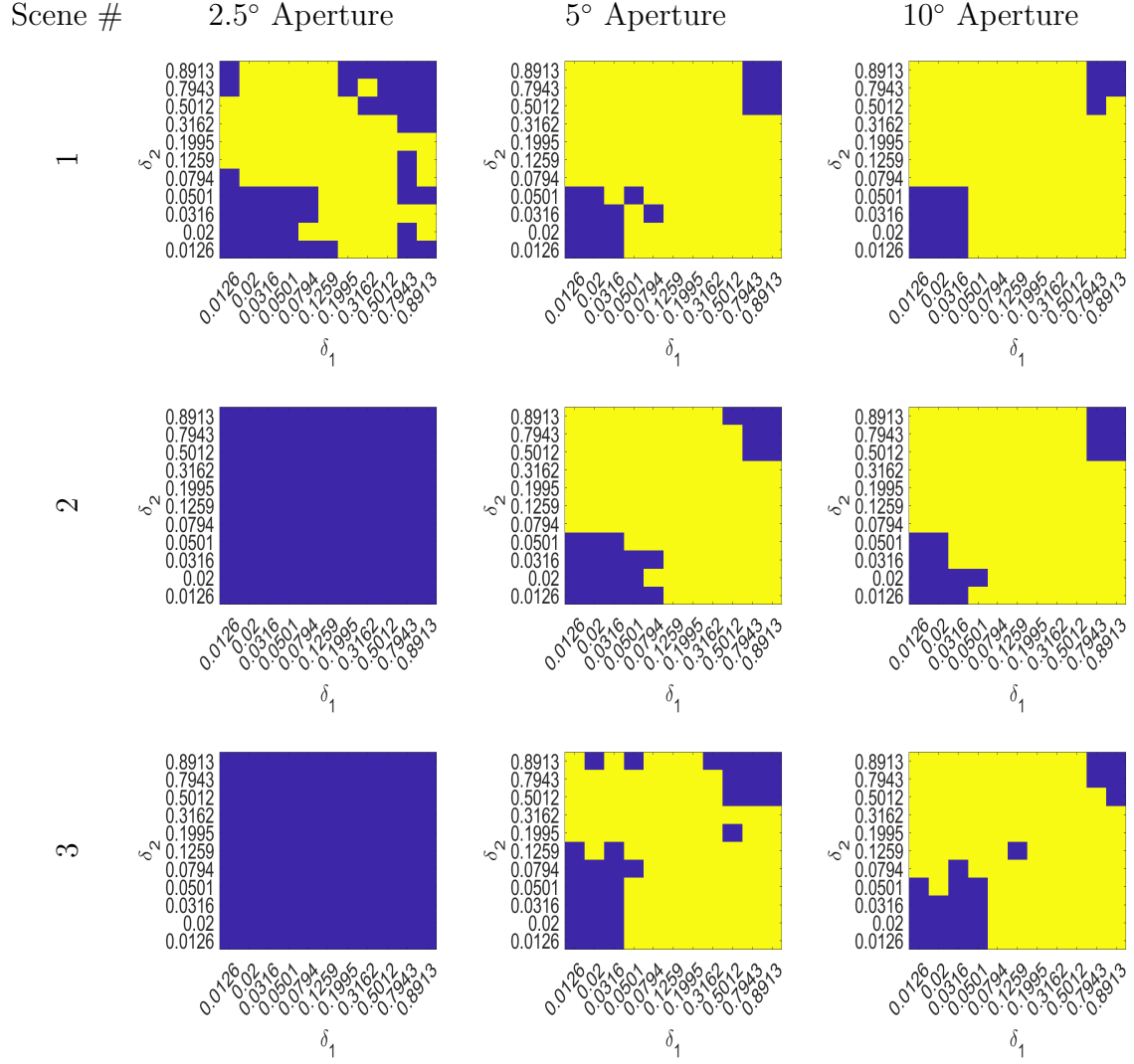


Figure 22. Success rate across crosstalk, scene, and PSF combinations for deterministic scenes, HH channel dropped. A yellow square represents a success, and a blue square represents a failure.

Here a very noticeable degradation in robustness is expected and observed. Recall that Scenes 2 and 3 are specifically designed to challenge the model. Looking at the relative error on \mathbf{b} in Figure 21 and more clearly the success rate in Figure 22, a lower bound has started to emerge. Particularly, the 5 and 10 degree aperture extents start to show a clear region of low crosstalk that does not lead to successful recoveries. Also of note is that the 2.5 degree aperture extent causes tremendous issues with Scenes 2 and 3, yielding no successful recoveries.

Figures 23–25, again made using Scene 2 and crosstalk pair $\delta_1 = \delta_2 = 0.1995$, help demonstrate the issues leading to the smaller success region. Specifically, Figure 23 shows the blurring in the cluster of targets in the bottom left corner. The blurring in the lower left target cluster is enough to lead to an unsuccessful recovery. The extreme crossrange blurring by the PSF along with the horizontally adjacent even and odd targets makes for a difficult recovery when the HH channel is dropped. Moving up to the 5 degree PSF is enough of a reduction in crossrange blur to allow the lower left cluster to be successfully recovered as shown in Figure 24.

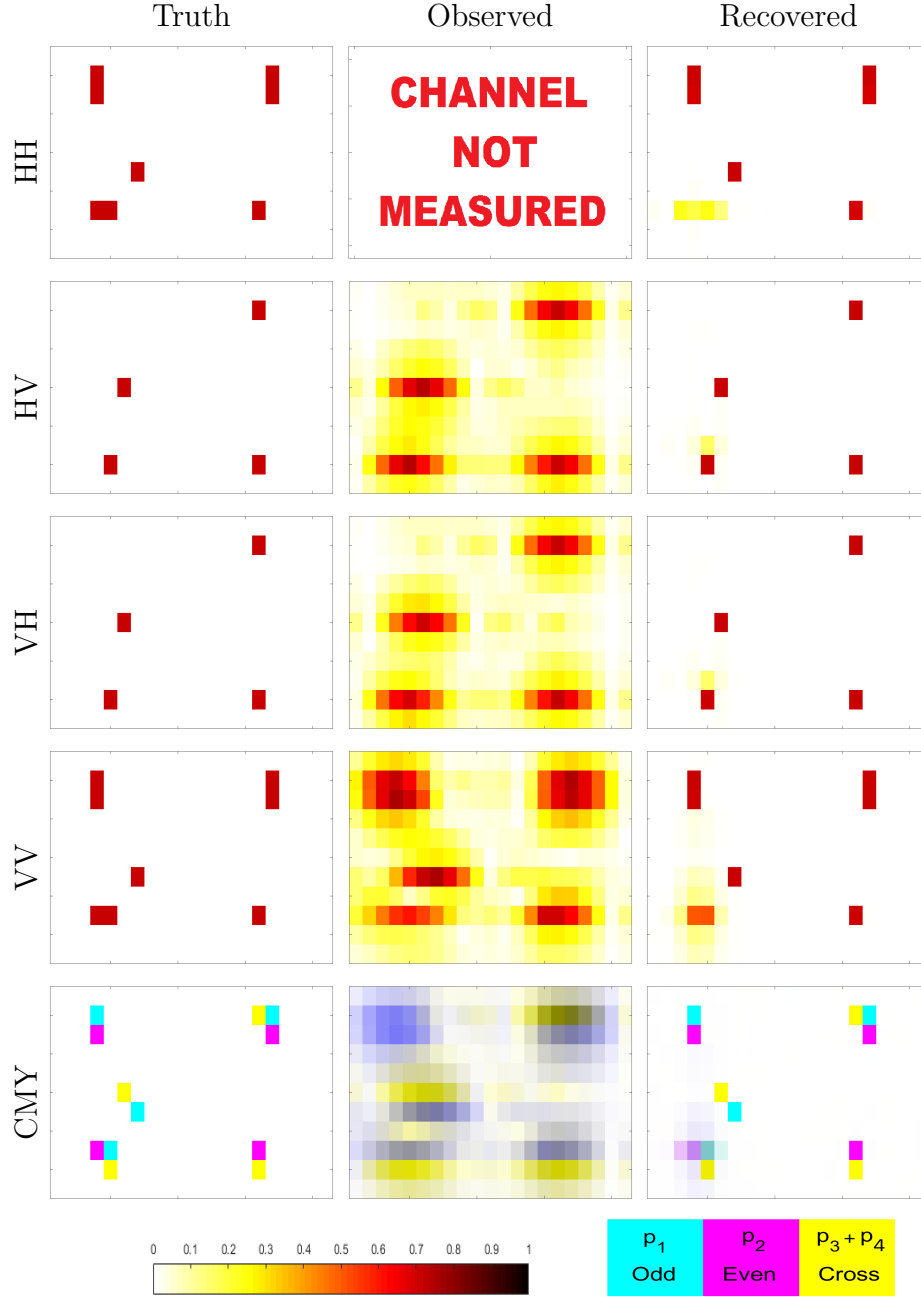


Figure 23. Truth, observed, and recovered scenes for Deterministic Scene 2 using $\delta_1 = \delta_2 = 0.1995$ and a 2.5° aperture extent, HH channel dropped

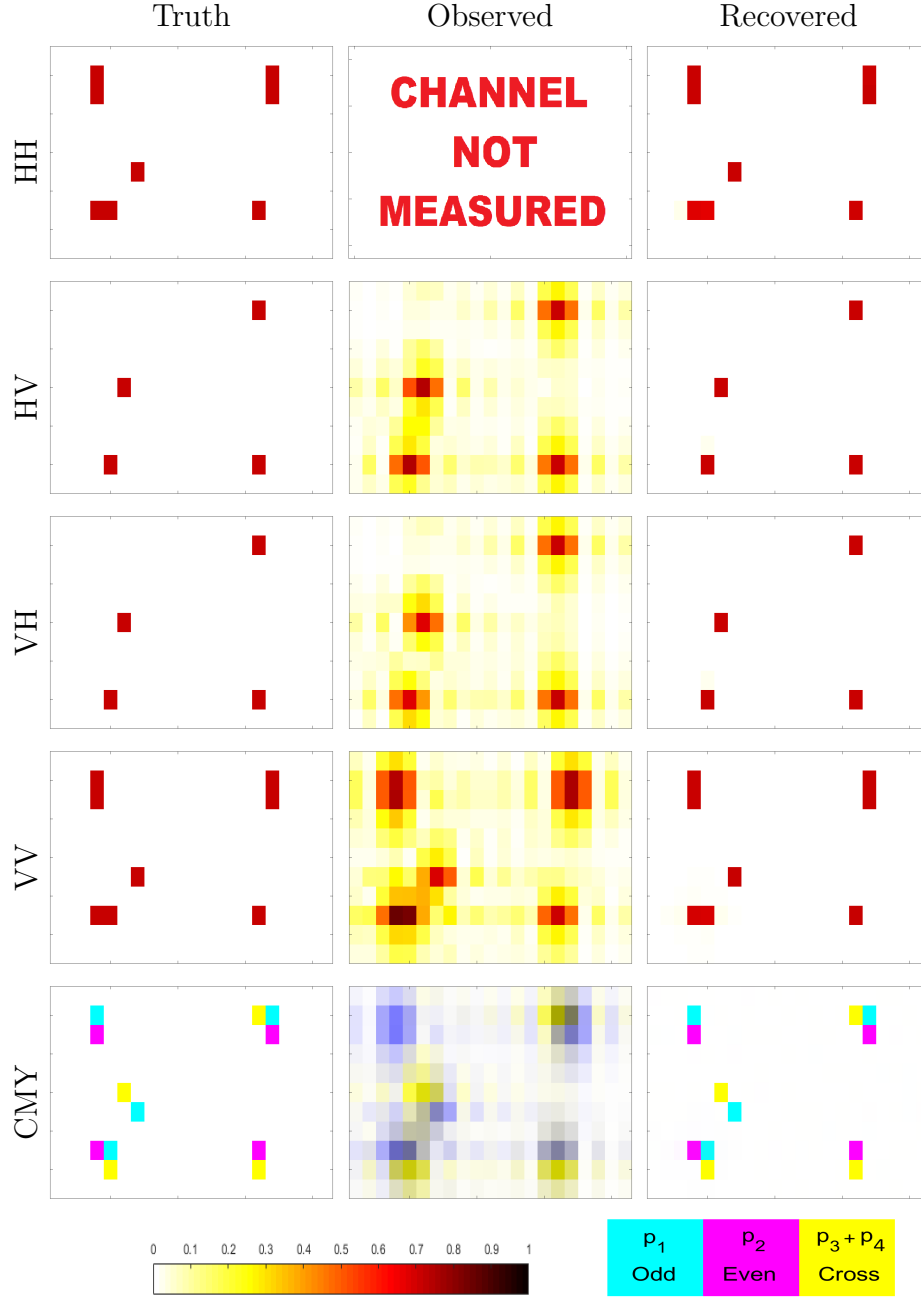


Figure 24. Truth, observed, and recovered scenes for Deterministic Scene 2 using $\delta_1 = \delta_2 = 0.1995$ and a 5° aperture extent, HH channel dropped

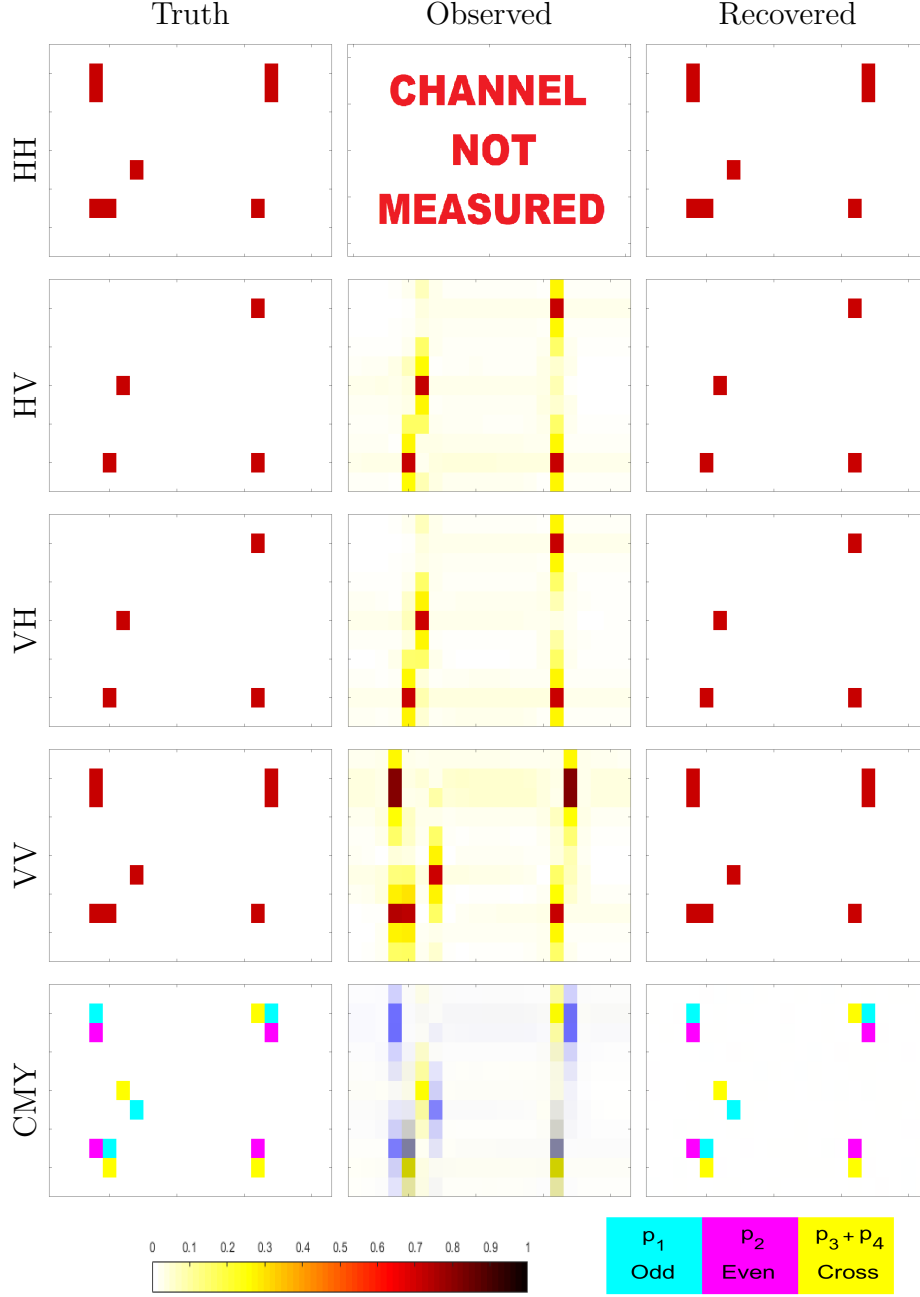


Figure 25. Truth, observed, and recovered scenes for Deterministic Scene 2 using $\delta_1 = \delta_2 = 0.1995$ and a 10° aperture extent, HH channel dropped

The deterministic results help show that the model is working as intended. Additionally, the use of fixed scenes has provide some insight into what can be expected with the following experiments. The beginnings of the robustness region have begun

taking shape, which shows that the search region is large enough to show the bounds. However, the unsuccessful regions are small, showing that the search grid is not oversized resulting in unnecessary computation time. Random scenes are required to more accurately determine the robustness region.

3.2.2.2 Zero-Phase Results.

Since phase crosstalk is difficult to design in an antenna [75], the first set of Monte Carlo trials assumes that the crosstalk is real, taking magnitude values from Table 1 and $\angle\delta_i = 0$. BPDN recovery (35) is tested over the aperture extents and target density percentages in Table 1. At each combination of PSF, target density, $|\delta_1|$ and $|\delta_2|$, 400 random point target scenes are generated by randomly setting coefficients in \mathbf{b} to one or zero. An example of the random scenes can be seen in Figure 26, which is taken at 3% target density relative to the composite \mathbf{b} vector. Note that for the synthetic scenes, the randomly-selected values in \mathbf{b}_{true} are set to 1 when generated. The HH channel is dropped and BPDN is used to recover the dropped channel. Figure 27 shows a sampling of the results at selected target density levels. As the number of targets increases, so does the average relative ℓ_2 recovery error. Despite the increased average ℓ_2 recovery error in scenes with higher target densities, a generally clear region can be seen over which the recovery error is low and thus that BPDN with the dropped-channel PolSAR model is successful. A total of 121 crosstalk combinations are searched in the zero-phase experiment; of those, 92 are found to provide recovery error below the 0.1 threshold. Thus, the robustness region is 76% of the total region searched.

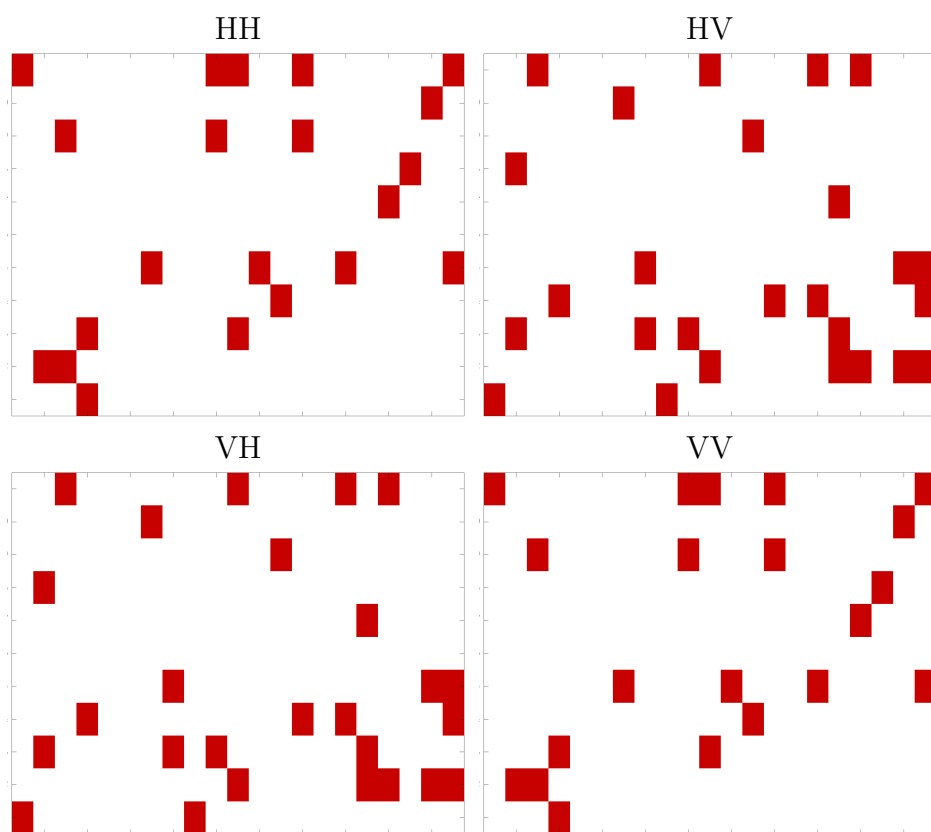


Figure 26. Example random point target scene, 5% target density in b

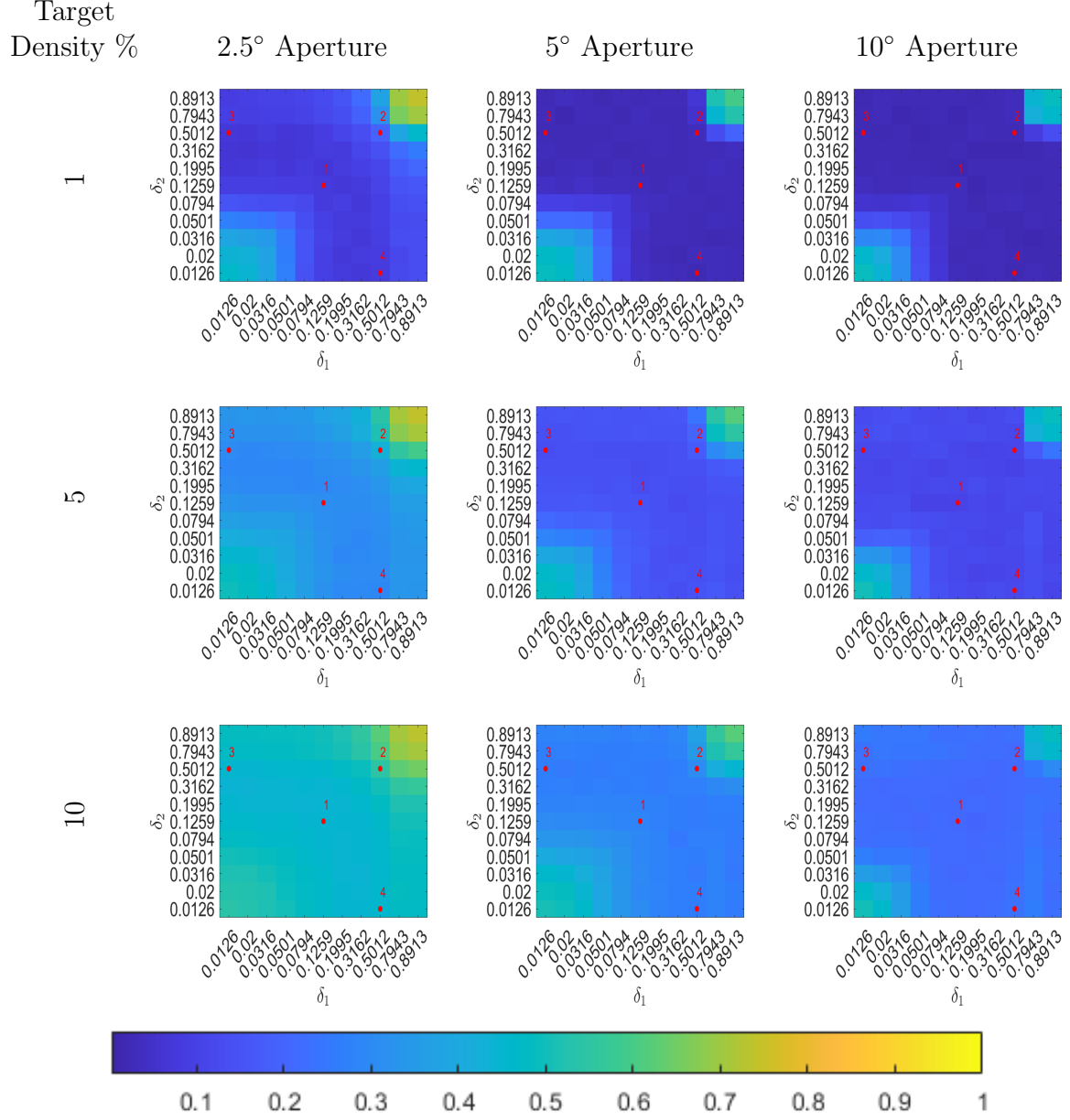


Figure 27. Average of relative fit (38) across Monte Carlo trials - Target Density Levels 1, 5, 10%

Naturally, increasing the target density raises the average relative error on \mathbf{b} . Figures 28–31 show a generally clear region over which BPDN recovery in the dropped-channel PolSAR model is successful as defined by the threshold on recovery error. Of the 121 crosstalk combinations searched in the zero-phase experiment, 92 provide successful recovery with (38) below the 0.1 threshold. That is, 76% of the total search region lies within the robustness region [105]. Additionally, Figures 28–31 show the target density limits of the $\mathbf{T} = \mathbf{R}$ dropped-channel PolSAR model. After 3% target density, recovery performance degrades across the entire range. Naturally the degradation is more noticeable in the 2.5 degree aperture extent. Even though the larger aperture extents degrade slower, Figures 30 and 31 show the clear decline in successful recoveries across the Monte Carlo trials to the point that the region is barely visible in the 10% target density case.

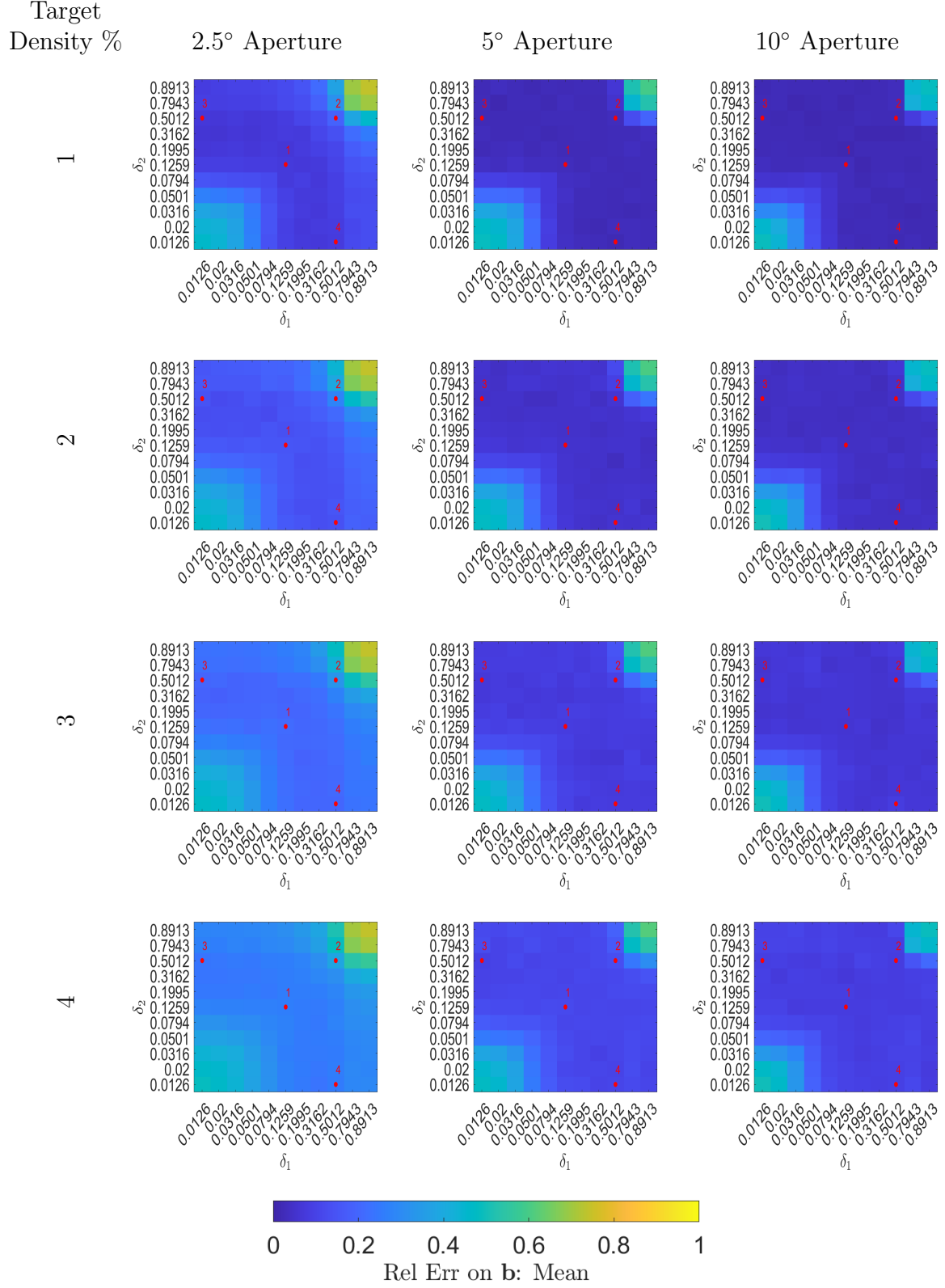


Figure 28. Average of relative fit (38) across Monte Carlo trials - Target Density Levels 1-4%

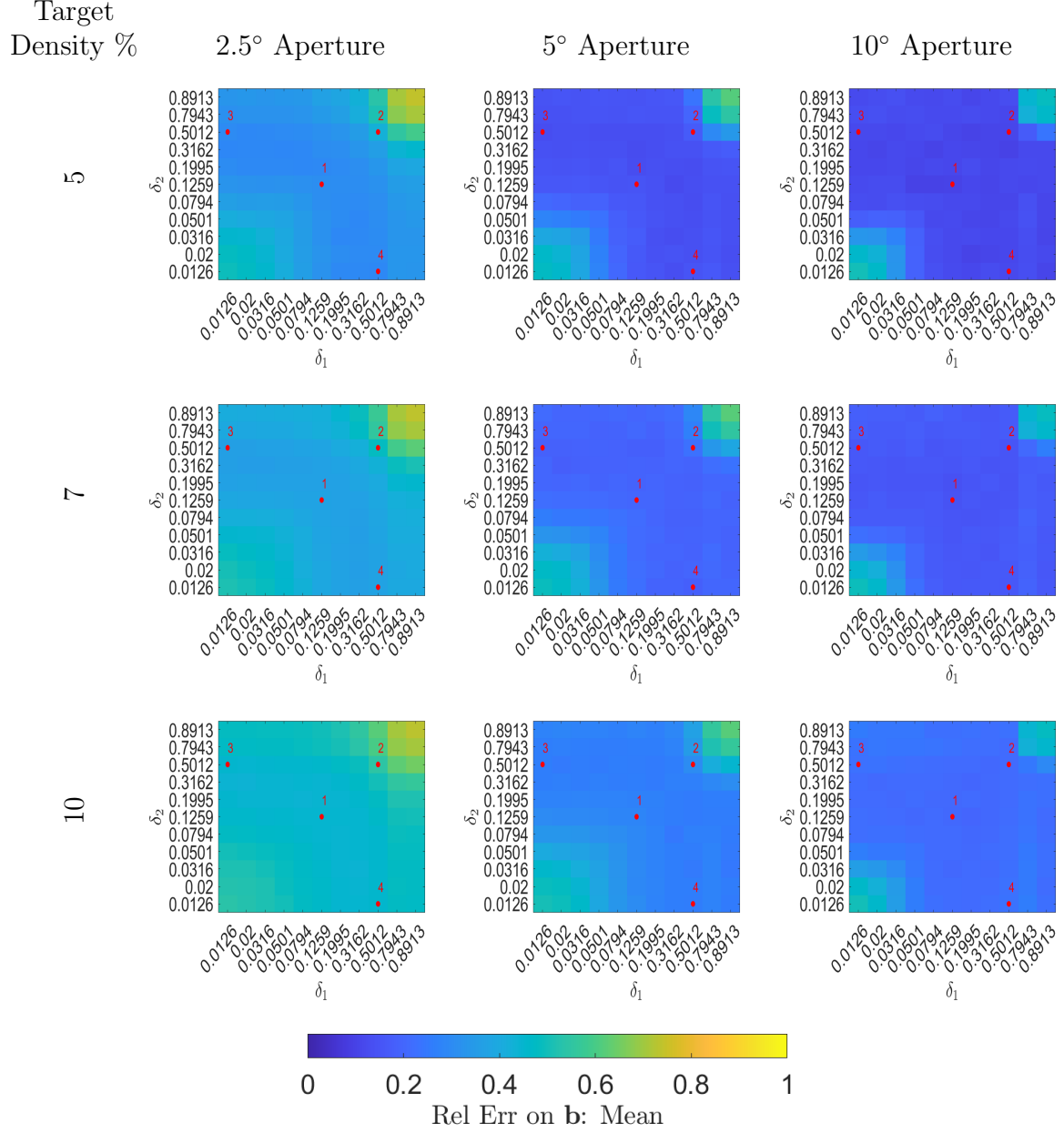


Figure 29. Average of relative fit (38) across Monte Carlo trials - Target Density Levels 5, 7, and 10%

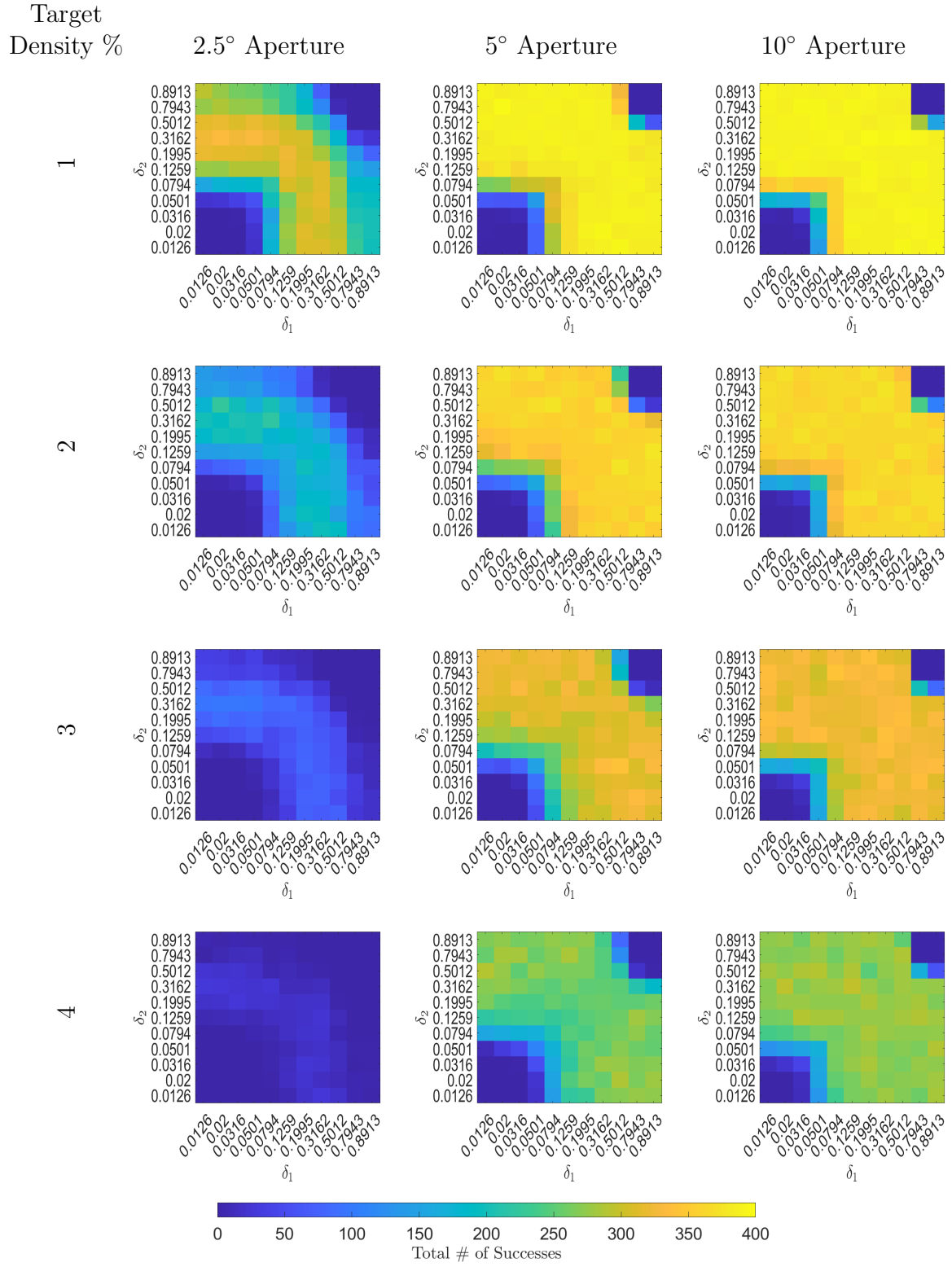


Figure 30. Total success rate across Monte Carlo trials - Target Density Levels 1-4%

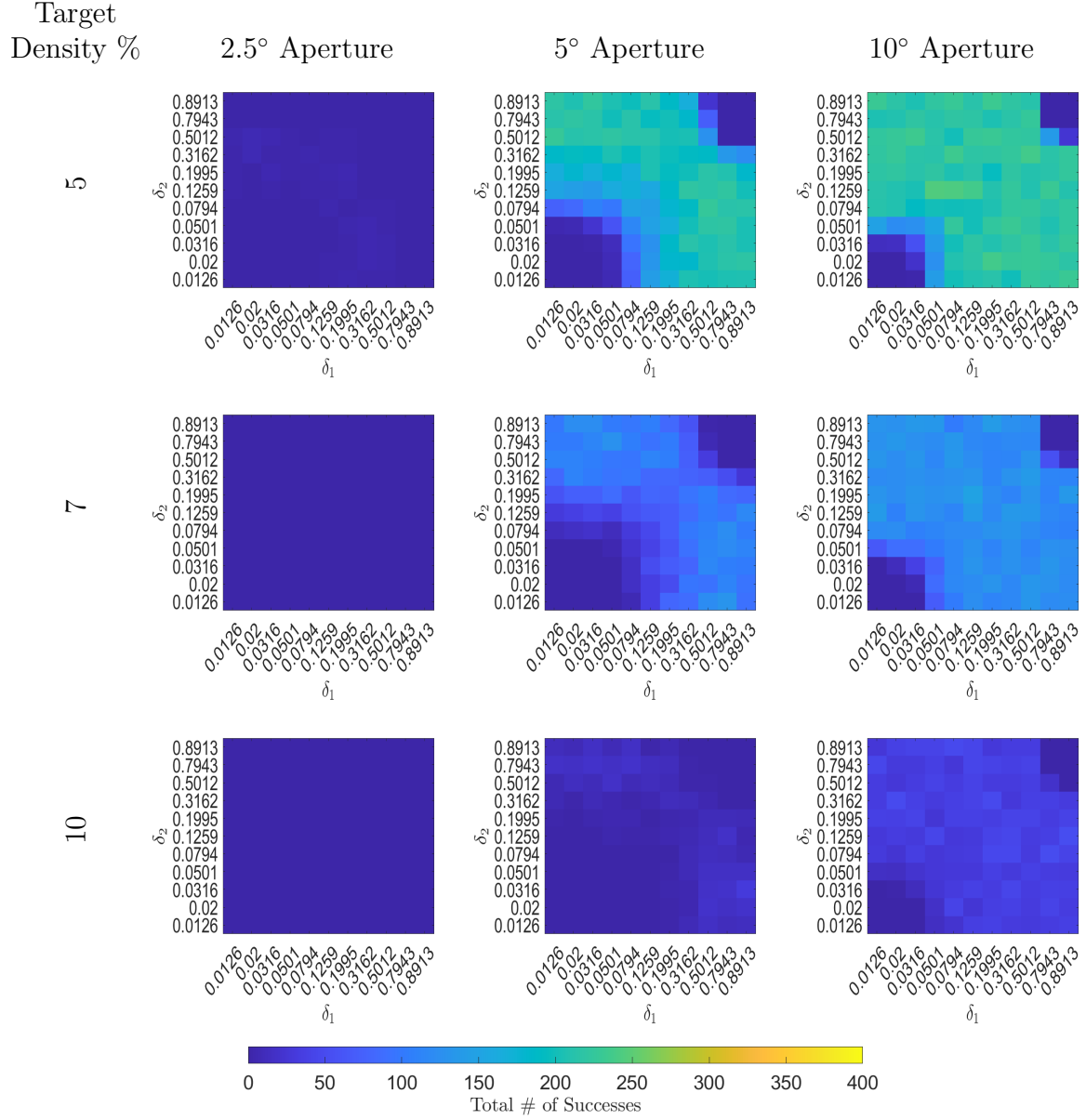


Figure 31. Total success rate across Monte Carlo trials - Target Density Levels 5, 7, and 10%

From Figures 28 and 29, four crosstalk pairs are selected to define the bounds of the robustness region. Figure 32 highlights the entire robustness region using the 2.5 degree aperture extent, 1% target density results. The 2.5 degree aperture extent is used for the highlight as it represents the most pessimistic results. Figure 27 shows that larger aperture extents may yield larger robustness regions. Two points on the anti-diagonal, and two points towards either corner are selected to represent the region of interest, as shown in Figure 32. Table 2 shows the values and errors of the selected points. The overall average relative error on \mathbf{b} in Table 2 is the average error over the Monte Carlo trials of the crosstalk point across all aperture extents and target density levels. The 1% target density average relative error on \mathbf{b} in Table 2 is the average relative error on \mathbf{b} of the Monte Carlo trials across all aperture extents for the 1% target density level. Since the overall average includes target density levels above what the model can recover, the overall error may be skewed above the 0.1 threshold. However the 1% target density case is well within the sparsity limits of the model and thus is under the 0.1 threshold.

Table 2. Crosstalk Points to Define Robustness Region

Pair #:	δ_1 :	δ_2 :	Overall Average ℓ_2 Error	1% Target Density ℓ_2 Error
1	0.1259	0.1259	0.1684	0.0448
2	0.5012	0.5012	0.2071	0.0794
3	0.5012	0.0126	0.1619	0.0381
4	0.0126	0.5012	0.1572	0.0386

Table 2 shows that the average of the relative error in the 1% target density case across all PSFs for the selected points is well below the 0.1 threshold for good recovery. Pair 2 is skewed high due to the 2.5 degree PSF. A look at Point 2 in Figure 27 for the 2.5 degree PSF, shows that the error has already begun trending up. The combination of the blurry PSF (2.5 degree in Figure 14) and significant degradation in recovery performance above 3% target density drives higher recovery

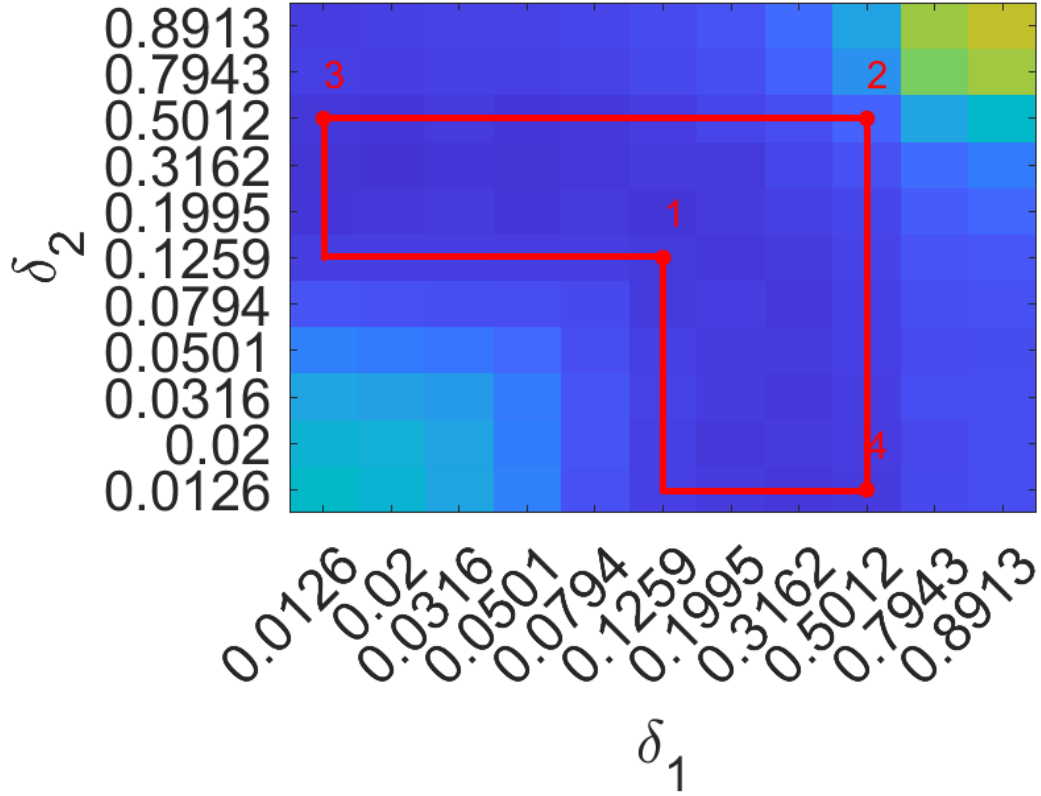


Figure 32. Highlight of the robustness region using the 2.5 degree aperture extent, 1% target density results.

error. In general, the points selected in Table 2 are representative of various portions of the robustness region. The selected points will thus be used for both the phase crosstalk testing and the GOTCHA sub-scene testing.

The top row of Figure 33 shows an overall average of the relative fit (38) results for each PSF across all seven target density levels listed in Table 1. Above a 3% target density level, recovery performance degrades above the 0.1 threshold as seen in the bottom row of Figure 33. The decline in higher target density levels makes the overall average results look more pessimistic; however, the robustness region is still clear in Figure 33.

The mutual coherence for each PSF and crosstalk combination is shown in the middle row of Figure 33. Note that the mutual coherence does not match up with

the error results. Typically, a low mutual coherence guarantees low error recovery. Since the measurement matrix \mathbf{A} from (35) had to be normalized first to compute mutual coherence, the structure of the model is fundamentally altered for (36). Thus, Figure 33 shows that low error recovery does not imply a low mutual coherence as the measurement matrices are now different between (35) and (36). As with the RIP, the structure of measurement matrix \mathbf{A}_1 is too non-random for mutual coherence to be a usable metric for dropped-channel PolSAR CS model.

The bottom row of Figure 33 shows the average relative ℓ_2 error (38) as a function of target density for the crosstalk robustness region boundary points identified in Figures 27 and 32. Predictably, the average relative error on \mathbf{b} rises with target density, which correlates with a drop in sparsity. Generally, a 3% target density is the upper limit for the model to stay within the 0.1 threshold.

Figure 34 shows the surface plots comparing the average recovery error with the SXR level with the x- and y-axis being the $|\delta_1|$ and $|\delta_2|$ values, the z-axis being the average relative error on \mathbf{b} for the target density level, and the color axis being the SXR value in dB. The top row is the surface plots for the 1% target density case. The bottom row is the overall average results across all target density levels, corresponding to the top row in Figure 33. Figure 34 more clearly shows the valley in recovery error and the corresponding SXR values. As before, the recovery error floor is lower in the 1% target density case due to the model breaking down in the higher target density levels. Additionally, we see that the recovery error floor lowers as the aperture extent is increased. Figure 34 also shows that the region of acceptable recovery performance coincides with SXR values between -8 dB and +10 dB. On the low crosstalk side (near peak in plots), above +10 dB SXR we see a marked rise above the 0.1 acceptance threshold. On the high crosstalk side (rear peak), we see a rapid spike above the recovery threshold when SXR drops below -8 dB, indicating that too much crosstalk

information is confusing the BPDN algorithm and damaging recovery performance. Good recovery over a wide range of crosstalk values eases the antenna design problem by allowing room for manufacturing tolerances and modeling errors.

Figure 35 shows slices of the SXR surface plots in Figure 34. The vertical slice is from the left-most column, along the axis labeled δ_2 in Figure 34 and the anti-diagonal slice is self-explanatory. Figures 34 and 35 show that acceptable recovery performance coincides with SXR values between -8 dB and +10 dB [105]. Comparing Figure 35 with Figure 34, note that the large spike in relative error on the high crosstalk side corresponds to a low SXR while the low crosstalk spike has a high SXR. The SXR range that correlates to successful recovery is then useful in determining the impact of adding phase values to the crosstalk matrix.

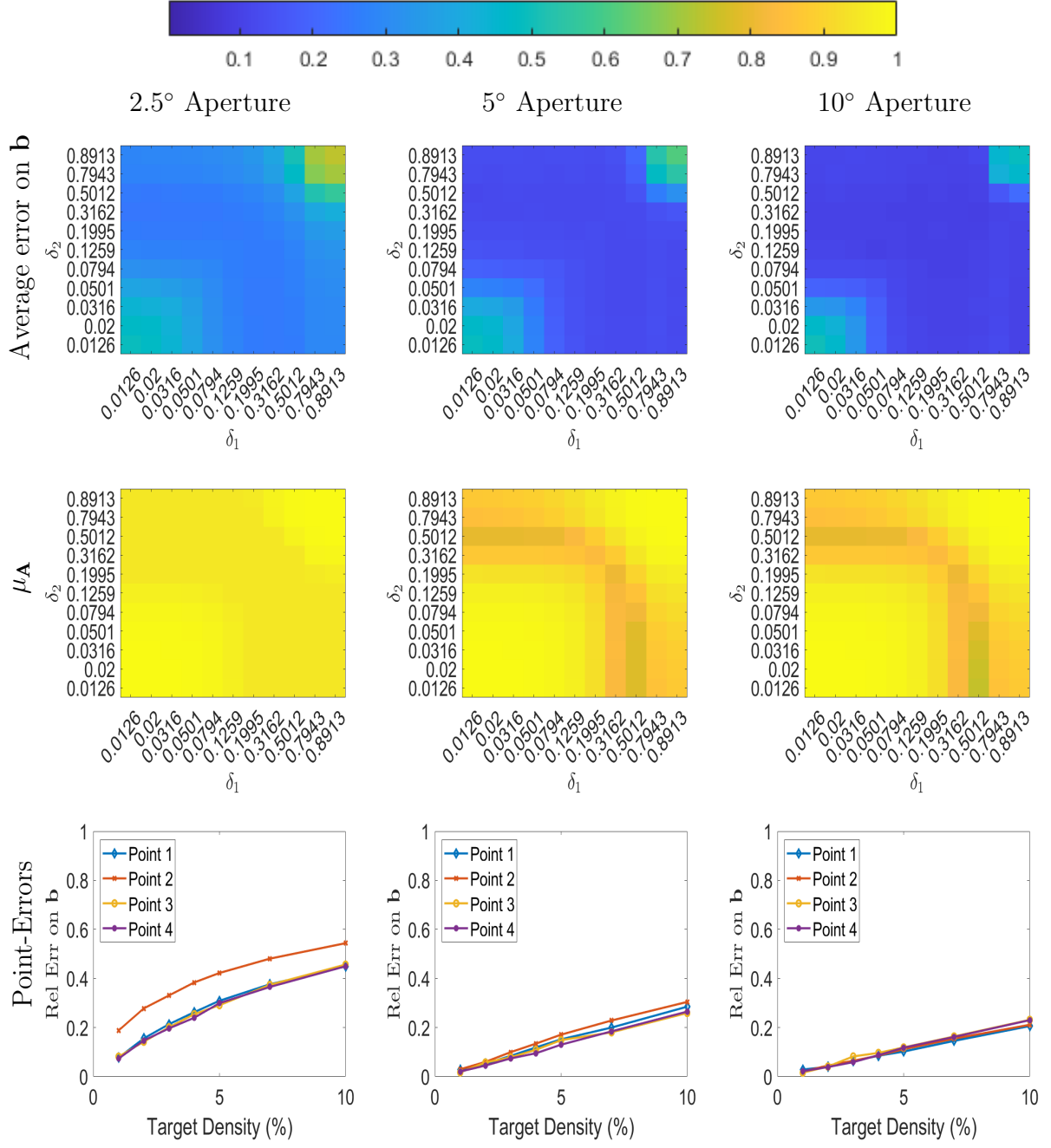


Figure 33. Overall average ℓ_2 -error (38) and mutual coherence for each aperture extent

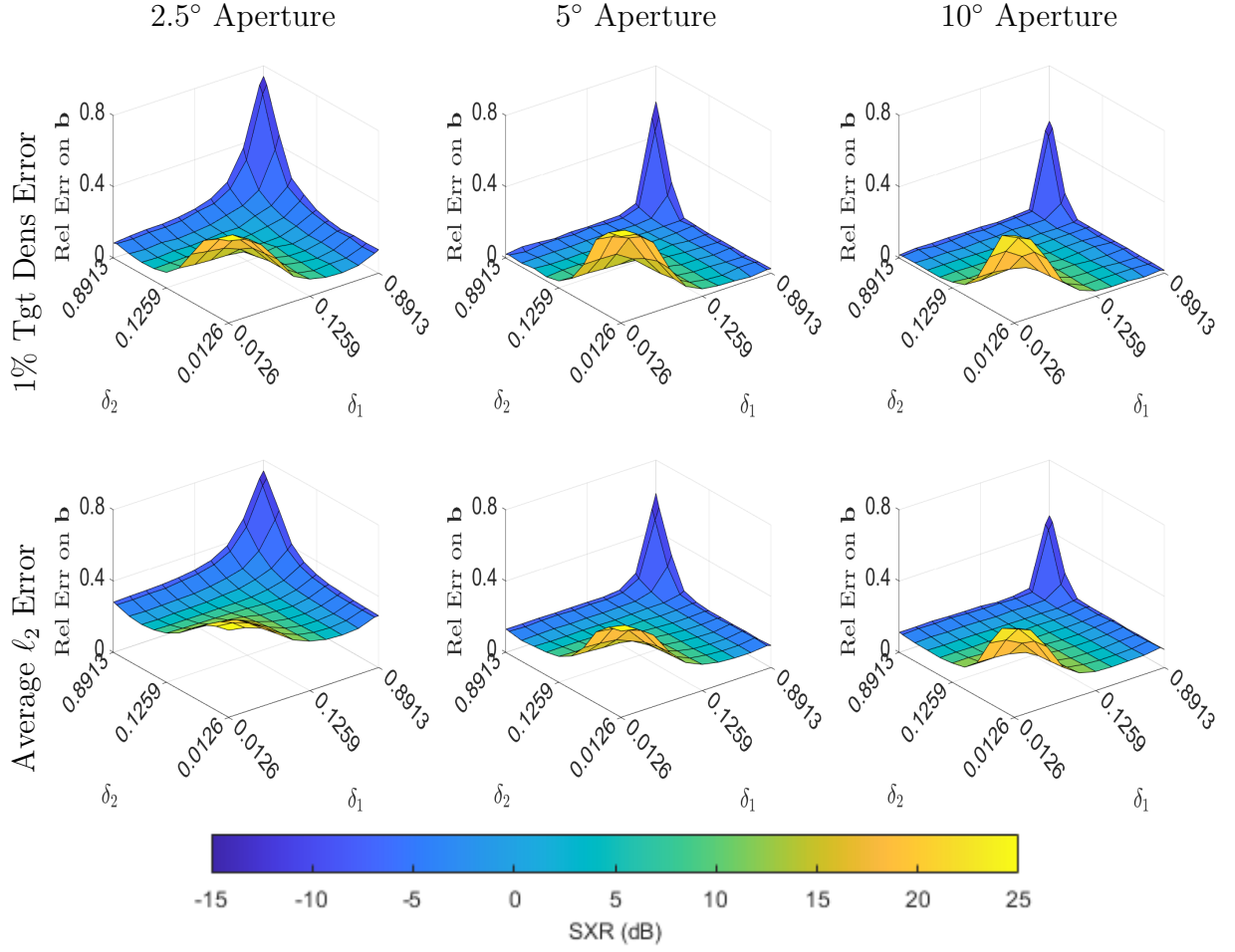


Figure 34. Surface plots comparing average relative error on \mathbf{b} and SXR for zero-phase crosstalk across all aperture extents for 1% target density and averaged across all sparsity levels listed in Table 1.

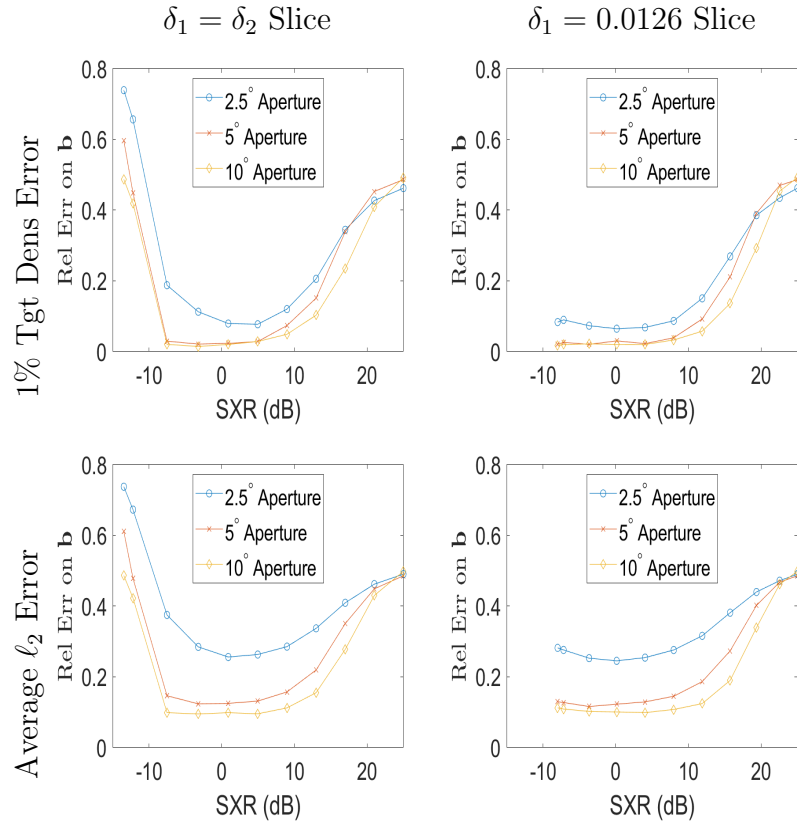


Figure 35. Anti-Diagonal and Vertical slices of SXR surface plots in Figure 34 showing error on \mathbf{b} as a function of SXR.

3.2.2.3 Complex-Valued Results.

The next set of Monte Carlo trials includes phase in the crosstalk values, using phase values from Table 1. Intuitively, we do not expect a significant impact from the inclusion of phase. With \mathbf{y}_{obs} , \mathbf{A} , and \mathbf{b} already being complex-valued, we would not expect a complex \mathbf{C} to further spread or contract the columns of \mathbf{A} in (24) to provide more or less accurate results, respectively. To reduce computational load, the phase grid is only applied to the four crosstalk pairs identified from the real crosstalk results in Figure 27. Figure 36 shows the surface plots of the average recovery error across Monte Carlo trials and SXR results over the grid of phase crosstalk levels. In Figure 36, the x- and y-axis labels are the phase values of the crosstalk prior to channel normalization, the z-axis is the average relative error on \mathbf{b} of the Monte Carlo trials, and the color axis is the SXR in dB. In the interest of space, only the 1% target density results are displayed as surface plots. As in the zero phase case, all target density levels in Table 1 are tested and used to generate the values in Figures 37–40.

In Figure 36, the $(x, y) = (0, 0)$ point is the reference point and thus has the same recovery error and SXR as its corresponding point in Figure 34. A change to SXR that would bring the value out of the robustness SXR range of -8 to +10 dB or an increase in average relative error on \mathbf{b} above the 0.1 recovery threshold would indicate a significant negative impact to recovery. A decrease in average relative fit is a positive impact on performance. To aid with visualization of the change in ℓ_2 error, Table 3 shows the minimum, maximum, and average signed error differences between the the grid points and the reference point for each aperture extent and crosstalk pair. In Table 3, a positive difference signifies a larger ℓ_2 recovery error than the reference point.

Looking at Figure 36, no noticeable variations in SXR are observed. Each value remains close to or equal to the reference point, which are all within the robustness

region. Additionally, the average recovery error does not appear to change much. The notable exception is the second crosstalk pair for the 2.5 degree aperture PSF. Figure 27 shows that crosstalk pair two is on the fringe of the robustness region, and the smallest aperture extent does not help the case. However, the same pair in Table 3 shows that the majority of the grid points actually have a lower average recovery error than the reference point. Even the few high points are only an increase of 4% or less, indicating that the addition of phase information to the crosstalk is a net benefit to the point at best and not a significant detriment at worst. The rest of Table 3 shows that average and even max error differences are small, and even the highest error difference is under +5%. Thus the errors with the inclusion of phase crosstalk remain inside ± 1 standard deviation of the distribution used to generate the random scenes and there is no evidence of significant negative impact when phase information is included in the crosstalk. Without the requirement of a specific phase crosstalk, the antenna design problem is further simplified.

Table 3. Signed Error Difference of each Aperture Extent and Crosstalk Pair Shown in Figure 36.

Crosstalk Pair	2.5 Degree			5 Degree			10 Degree		
	Min	Avg	Max	Min	Avg	Max	Min	Avg	Max
1	-0.0220	0.0037	0.0475	-0.0124	0.0052	0.0329	-0.0098	0.0056	0.0310
2	-0.1363	-0.0756	0.0364	-0.0133	0.0015	0.0329	-0.0074	0.0083	0.0217
3	-0.0115	0.0088	0.0316	-0.0053	0.0103	0.0250	-0.0102	0.0047	0.0226
4	-0.0219	-0.0040	0.0191	-0.0102	0.0037	0.0213	-0.0121	0.0017	0.0199

3.2.2.4 $\mathbf{T} \neq \mathbf{R}$ Results.

Figures 28 and 29 show a clear drop in recovery performance above a 3% target density level when $\mathbf{T} = \mathbf{R}$ is assumed. However, prior work in [6, 7] suggests that the model in (35) can work for higher target density scenes. In [6, 7] it is not assumed that $\mathbf{T} = \mathbf{R}$, so for a brief comparison, an example where $\mathbf{T} \neq \mathbf{R}$ is examined to determine if relaxing the assumption would improve recovery performance. To

maintain the monostatic assumption, we can assume that some active components are added to the antenna design to help achieve the desired crosstalk values. The example examined comes from [7, Eqn 18] and is restated below for clarity.

$$\begin{aligned}
\mathbf{C} &= \mathbf{T} \otimes \mathbf{R}^T \\
&= \begin{bmatrix} t_{HH} & \delta_1 \\ \delta_2 & t_{VV} \end{bmatrix} \otimes \begin{bmatrix} r_{HH} & \delta_3 \\ \delta_4 & r_{VV} \end{bmatrix} \\
&= \begin{bmatrix} 0.78 & -0.6201 + 0.0695i \\ 0.6802 + 0.2030i & 0.7098 \end{bmatrix} \\
&\quad \otimes \begin{bmatrix} 0.93 & -0.0220 - 0.3713i \\ -0.0220 - 0.3713i & 0.93 \end{bmatrix}
\end{aligned} \tag{40}$$

To test the robustness of the crosstalk matrix in (40), a small shift in magnitude and phase is added to each of the δ values. Specifically, $\delta_{i,new} = \delta_{i,init} + 0.1 \exp(j \frac{(k-1)\pi}{4})$ for $i = 1, \dots, 4$, $k = 1, \dots, 8$. As before, the channels are then normalized with the new δ values to conserve power. The offsets are applied equally to $\{\delta_1, \delta_3\}$ and to $\{\delta_2, \delta_4\}$ to maintain the difference ratio between \mathbf{T} and \mathbf{R} . A total of $8 \times 8 = 64$ crosstalk combinations surrounding the original crosstalk matrix (40) are used as test points for robustness. As with the $\mathbf{T} = \mathbf{R}$ cases, each crosstalk combination is run over three aperture extents and seven target density levels. At each crosstalk level, target density, and aperture extent, 400 random scenes are recovered via BPDN.

Figures 37 and 38 show the average recovery error (38) for each target density level and aperture extent. Figures 39 and 40 show the success rate corresponding to Figures 37 and 38. The axes labels Cidx₁ and Cidx₂ enumerate the values $k = 1, \dots, 8$ used to shift the phase to $\{\delta_1, \delta_3\}$ and $\{\delta_2, \delta_4\}$, respectively, as described in the previous paragraph. A quick comparison with Figures 28–31 show a significantly lower

average recovery error and higher success rate into the higher target density levels. As expected, the 2.5 degree aperture extent degrades the quickest, however the success rate doesn't uniformly go to zero until the 10% target density. For comparison, in the $\mathbf{T} = \mathbf{R}$ case, the 2.5 degree aperture extent shows very little success in the 5% target density and no success in the 7% target density case. For the other aperture extents, the recovery performance remains good through 10% target density, indicating that letting $\mathbf{T} \neq \mathbf{R}$ increases the sparsity limit of the model.

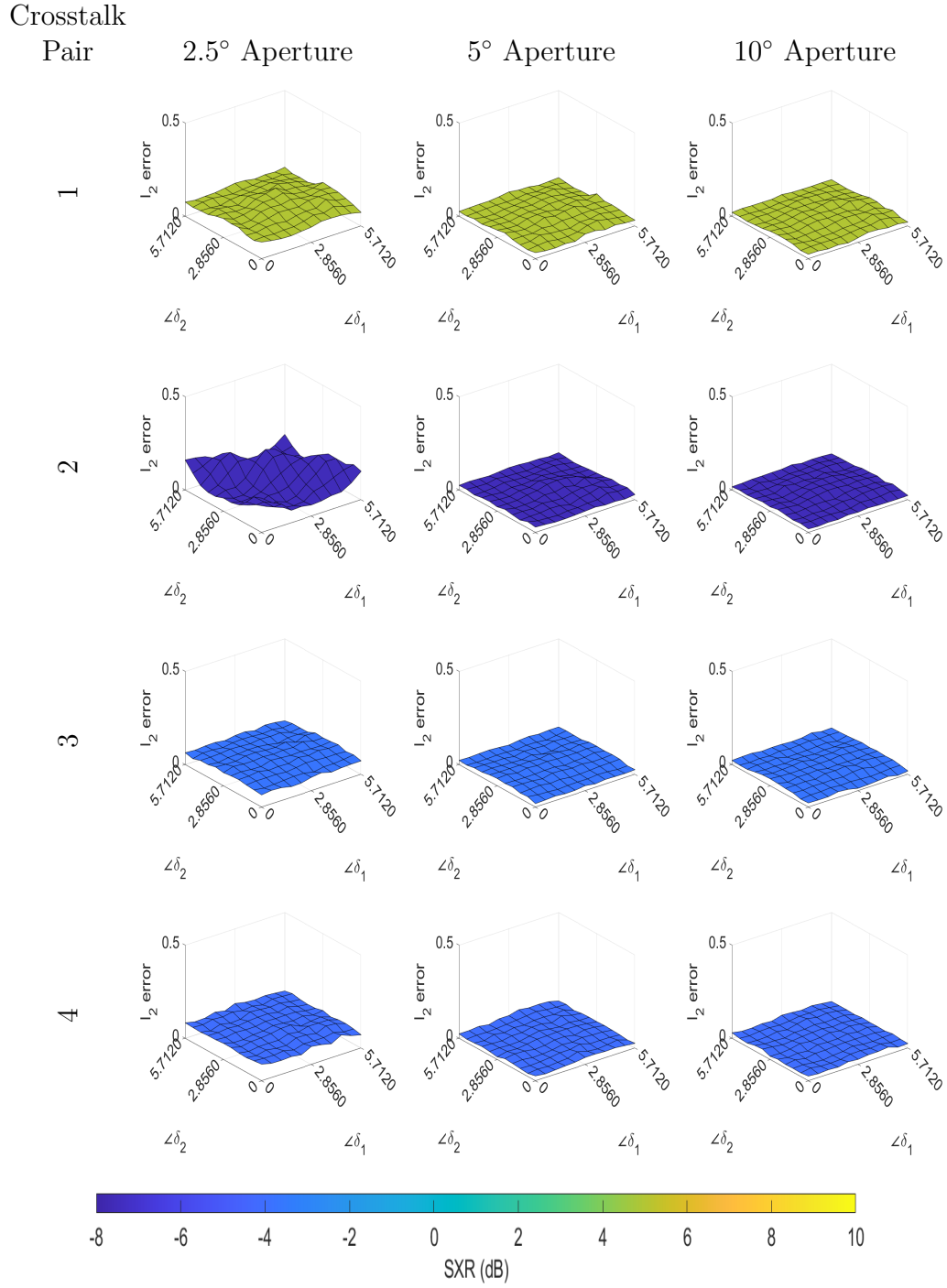


Figure 36. Surface plots of each PSF and Crosstalk Pair showing average relative error on b and SXR for Complex Crosstalk - 1% Target Density.

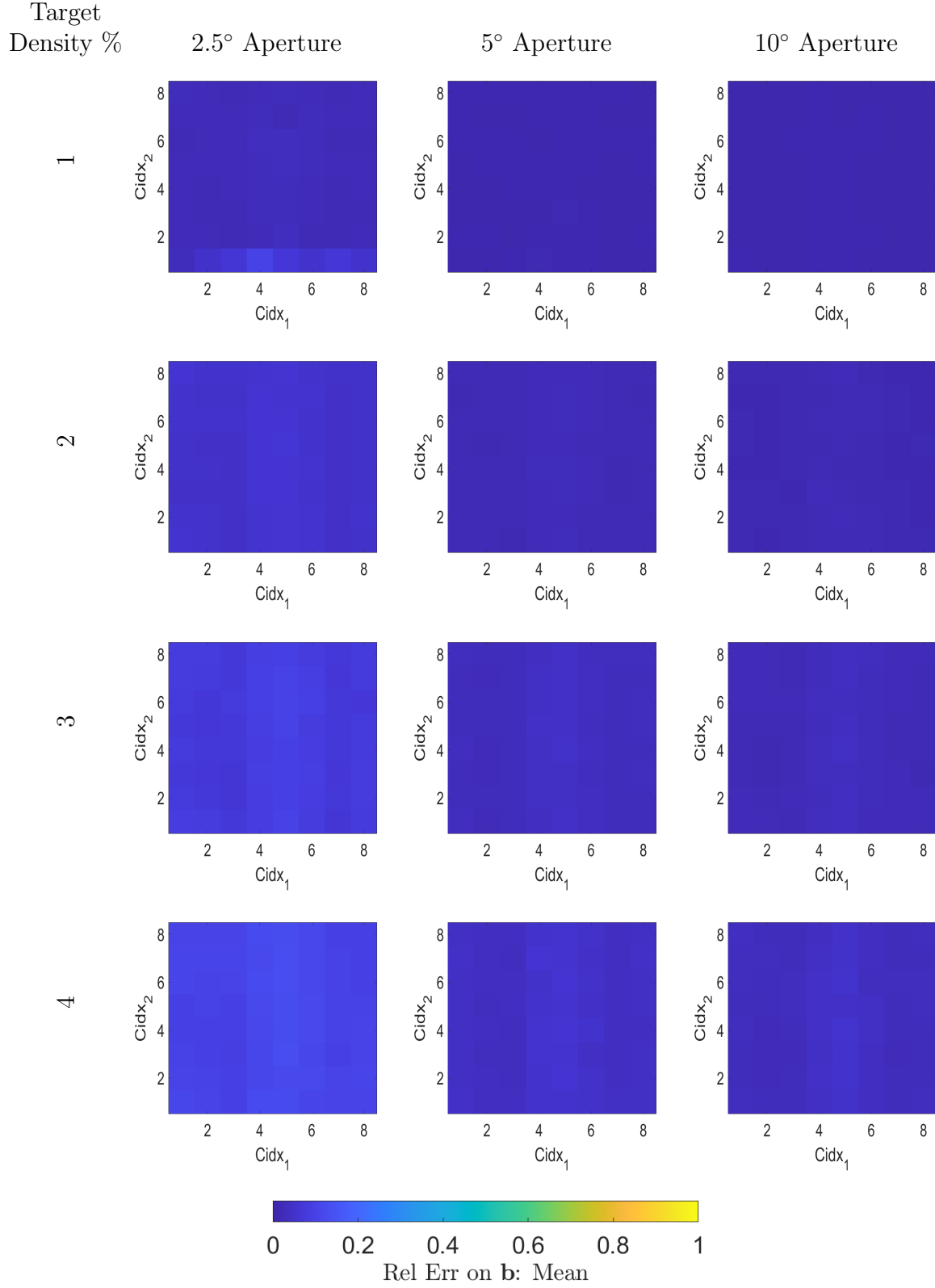


Figure 37. Average of relative fit (38) across Monte Carlo trials - Target Density Levels 1-4% - $T \neq R$ case

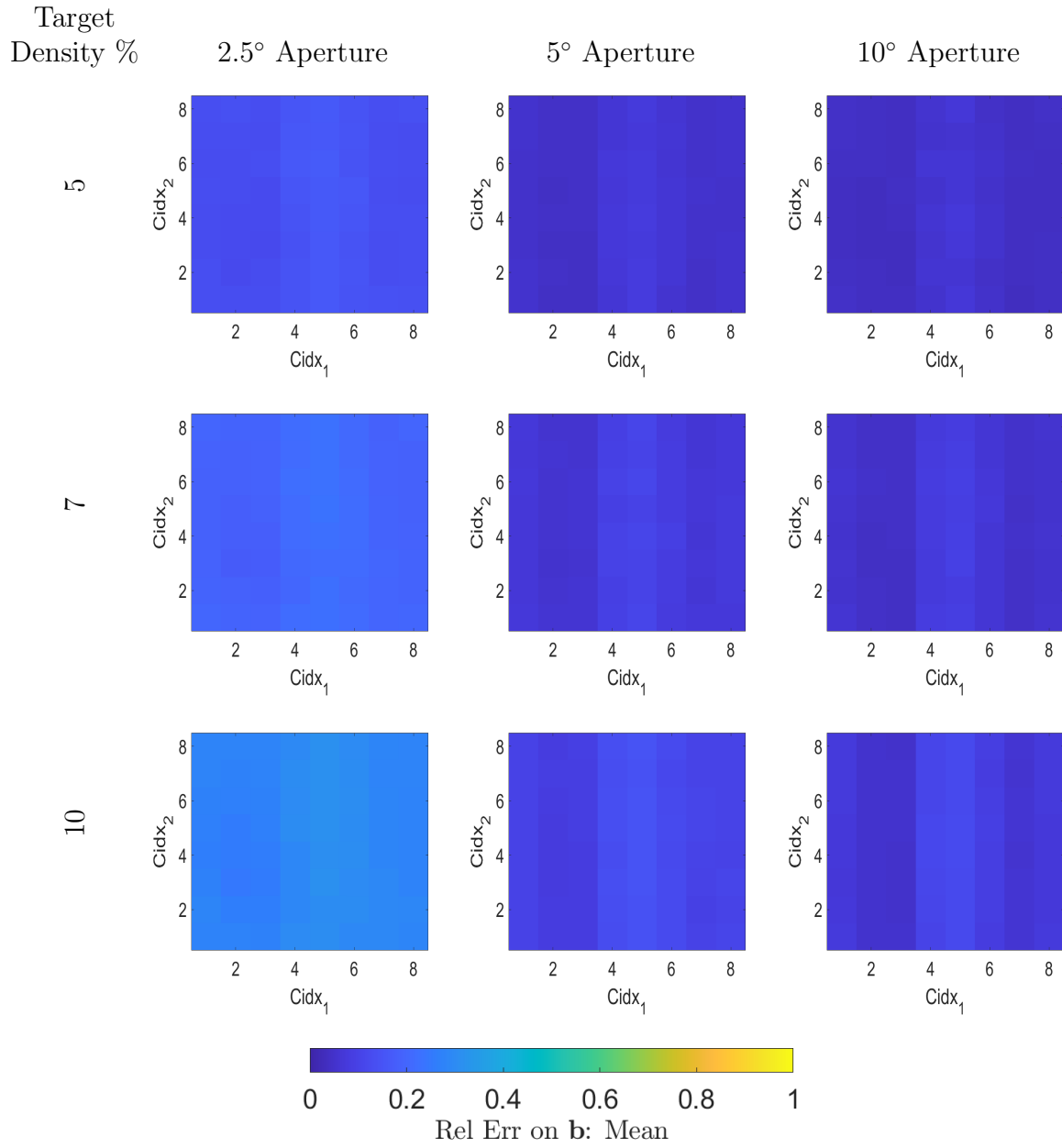


Figure 38. Average of relative fit (38) across Monte Carlo trials - Target Density Levels 5, 7, and 10% - $T \neq R$ case

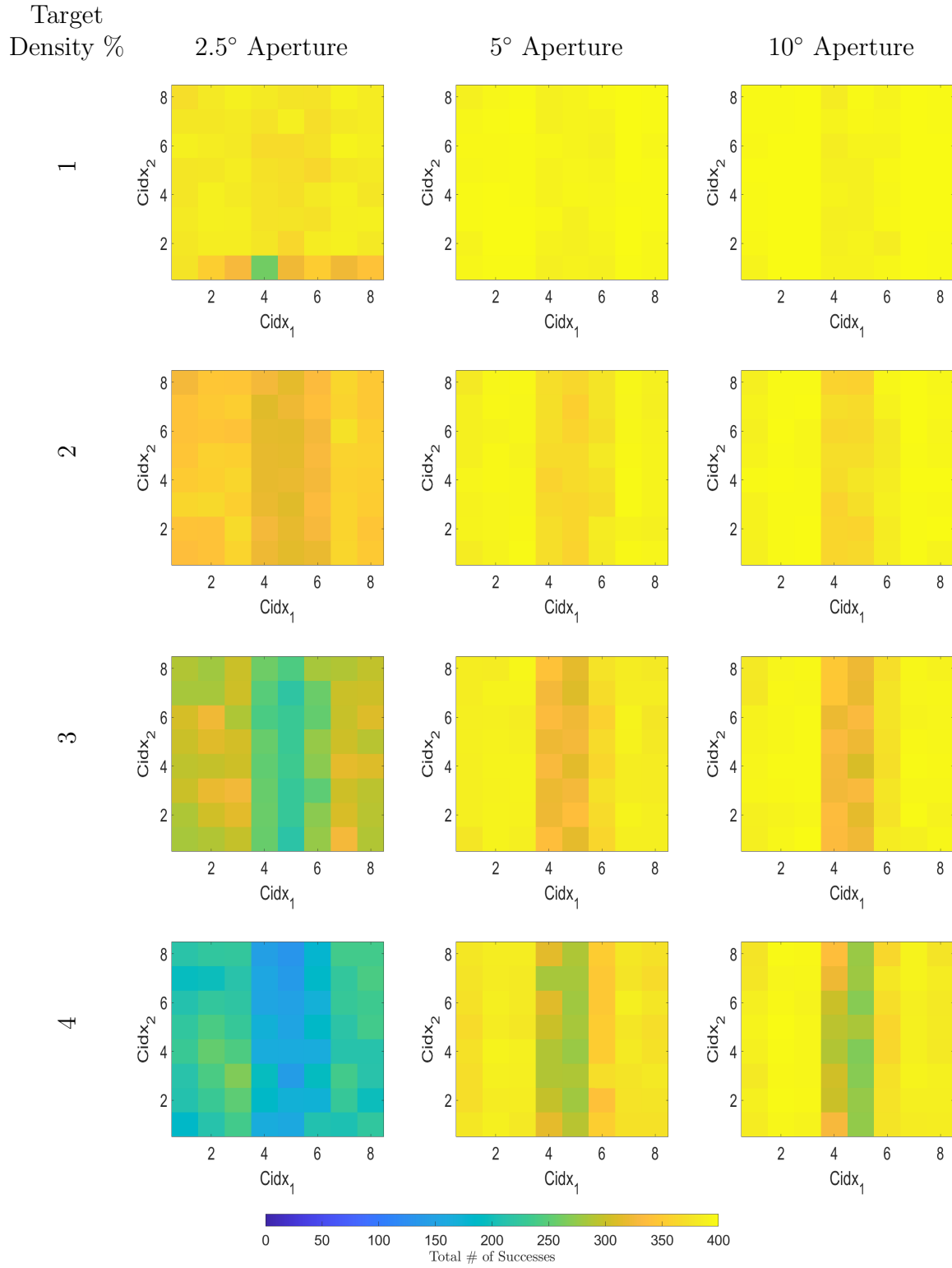


Figure 39. Total success rate across Monte Carlo trials - Target Density Levels 1-4% - $T \neq R$ case

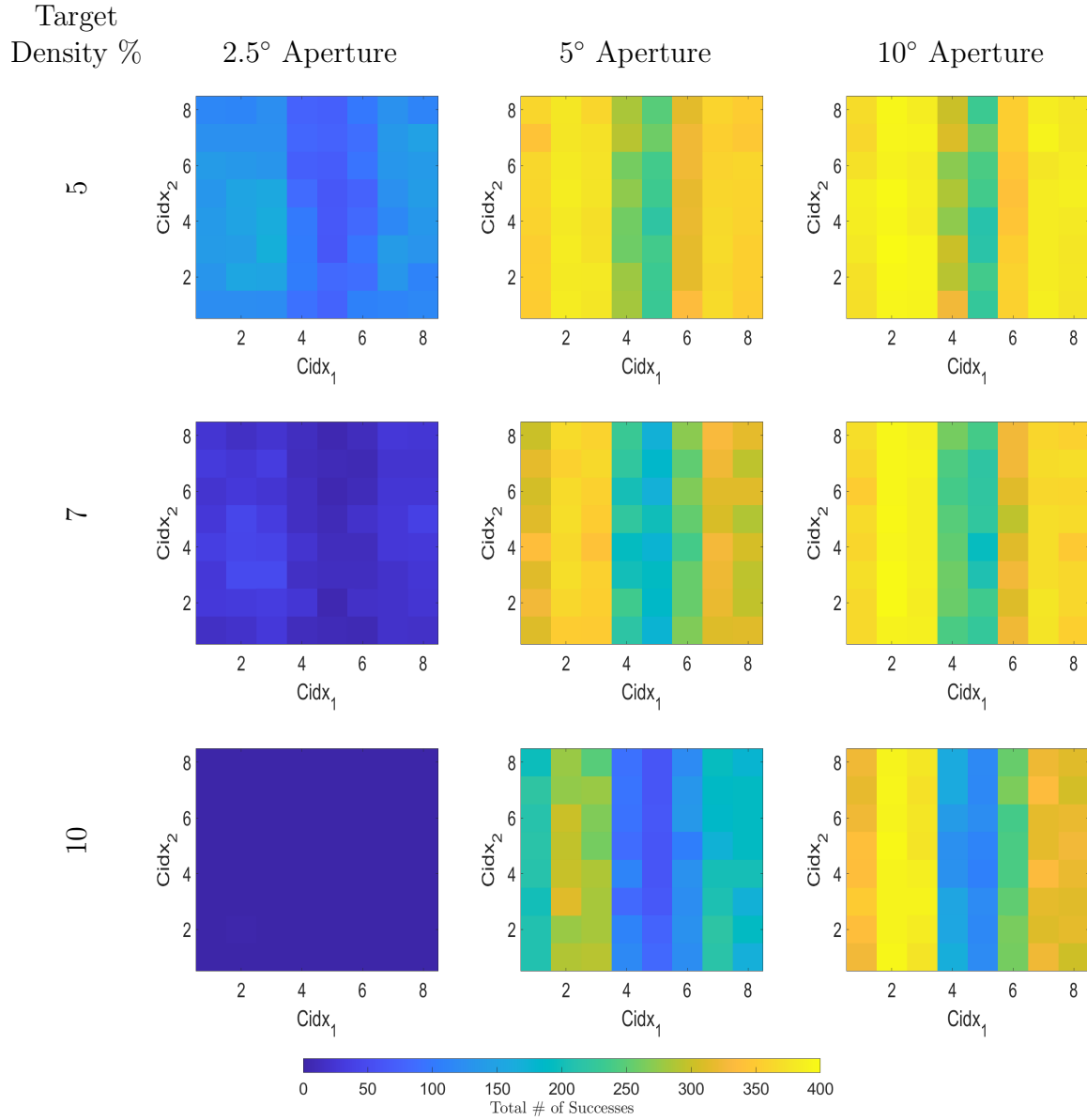


Figure 40. Total success rate across Monte Carlo trials - Target Density Levels 5, 7, and 10% - $T \neq R$ case

The top row of Figure 41 shows the relative error on \mathbf{b} averaged over all target density levels in Table 1 for each aperture extent. Although the $\mathbf{T} = \mathbf{R}$ case failed to recover dense target scenes, the $\mathbf{T} \neq \mathbf{R}$ average ℓ_2 -error is very low. Comparing to the top row of Figure 33, the results in Figure 41 have lower maximum values, indicating that the crosstalk matrix in (40) is in a robustness region. The bottom row of Figure 41 shows the mean error on \mathbf{b} values of select points at each target density. The points chosen are the four corners of the average error on \mathbf{b} plots in the top row of Figure 41. The reference point is point 4 from Figure 33, which is the best performing $\mathbf{T} = \mathbf{R}$ point. Comparing with the bottom row of Figure 33, the results in Figure 41 are closer together and overall lower. The amount of reduction in average error on \mathbf{b} is easily seen by comparing the reference point to the selected points in Figure 41. For any target density level above 1%, a significant improvement in average error on \mathbf{b} is observed in each PSF. By relaxing the requirement that $\mathbf{T} = \mathbf{R}$, higher target density scenes can be successfully recovered.

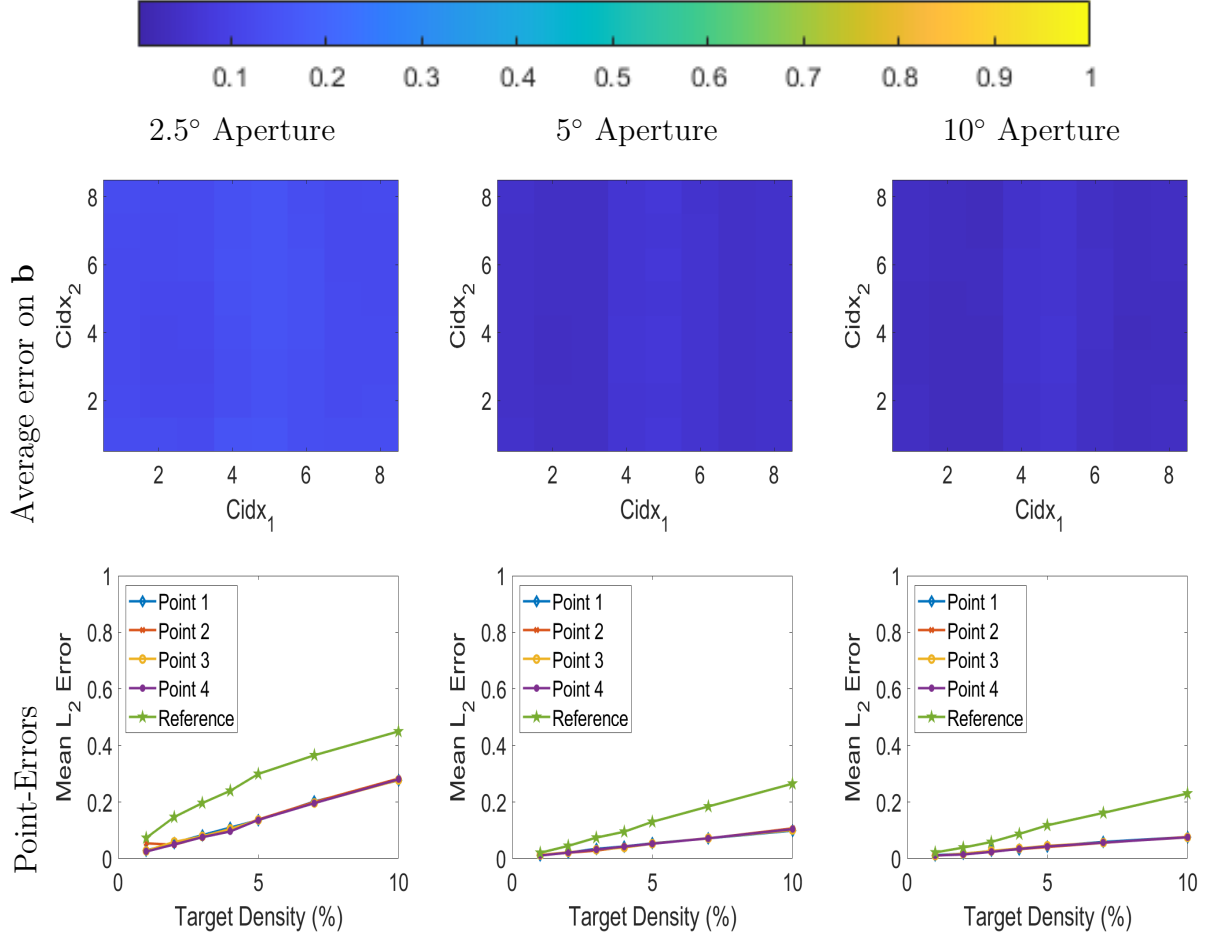


Figure 41. Overall average relative error on \mathbf{b} for each aperture extent, $\mathbf{T} \neq \mathbf{R}$ case. Reference line is Point 4 (best performance) from $\mathbf{T} = \mathbf{R}$ case in Figure 33.

3.3 Experiment 2: Simulated GOTCHA Scenes

Next, we consider dropped-channel polarization recovery on a realistic scene from the GOTCHA data set [29]. To provide a variety of targets to test recovery performance we choose a large segment: the calibration scene in the upper left corner. To keep performance metrics consistent, a truth vector is needed to compute the relative error on \mathbf{b} (38). To make a GOTCHA sub-scene truth vector we first use the polar format algorithm (PFA) [28] to generate an observation vector (\mathbf{y} in (24)). At each sub-aperture step, BPDN is performed using the corresponding PSF, no channel drops ($\mathbf{J} = \mathbf{I}_4$), and no crosstalk ($\mathbf{C} = \mathbf{I}_4$). That is, the pseudo-truth scenes in Figure 42

are created by combining the full 360 degree GOTCHA aperture using sub-aperture step sizes corresponding to the aperture extents in Table 1. Once all sub-apertures are evaluated, the results are coherently integrated in \mathbf{x} and the pseudo-truth vectors \mathbf{b}_{ref} are produced via $\mathbf{b}_{ref} = (\mathbf{P} \otimes \mathbf{S})^H \mathbf{x}$ where $(\cdot)^H$ denotes the conjugate transpose. Note that using the adjoint to produce \mathbf{b}_{ref} works because $\mathbf{S} = \mathbf{I}$ and \mathbf{P} is orthonormal, meaning that $(\mathbf{P} \otimes \mathbf{S})$ is also orthonormal. While the error in \mathbf{b} will be the same as in \mathbf{x} due to the linear mapping between \mathbf{x} and \mathbf{b} , vector \mathbf{b} was chosen to keep the comparison of results between the point target scenes and the GOTCHA scenes as similar as possible. These pseudo-truth vectors are then used in (38) when computing the recovery error to provide consistent results that are comparable to the synthetic scene results. Pseudo-truth images $\mathbf{y} = \mathbf{A}\mathbf{b}_{ref}$ are shown in the top row of Figure 42.

Having ruled out significant impact of phase crosstalk to recovery performance, the GOTCHA results are run using zero-phase crosstalk at the points shown in Figure 27 and enumerated in Table 2 over all three aperture extents. The GOTCHA scenes analyzed by putting the pseudo-truth vector generated in the previous paragraph through the BPDN model (35) with the inclusion of crosstalk (\mathbf{C} as in (34)) and dropping the HH-channel. The results are shown in Figure 42 using a synthetic CMY scheme with cyan representing the first column of (37) (odd bounce), magenta representing the second column of (37) (even bounce), and yellow representing the third and fourth columns of (37) (real and imaginary cross-polarized) combined. Of note, since all four channels are used, we are not using the auto-focused GOTCHA data, which only exists for the co-pol channels. By not using the auto-focused data, the CMY results may appear shifted polarimetrically (i.e. the top hat should be more magenta).

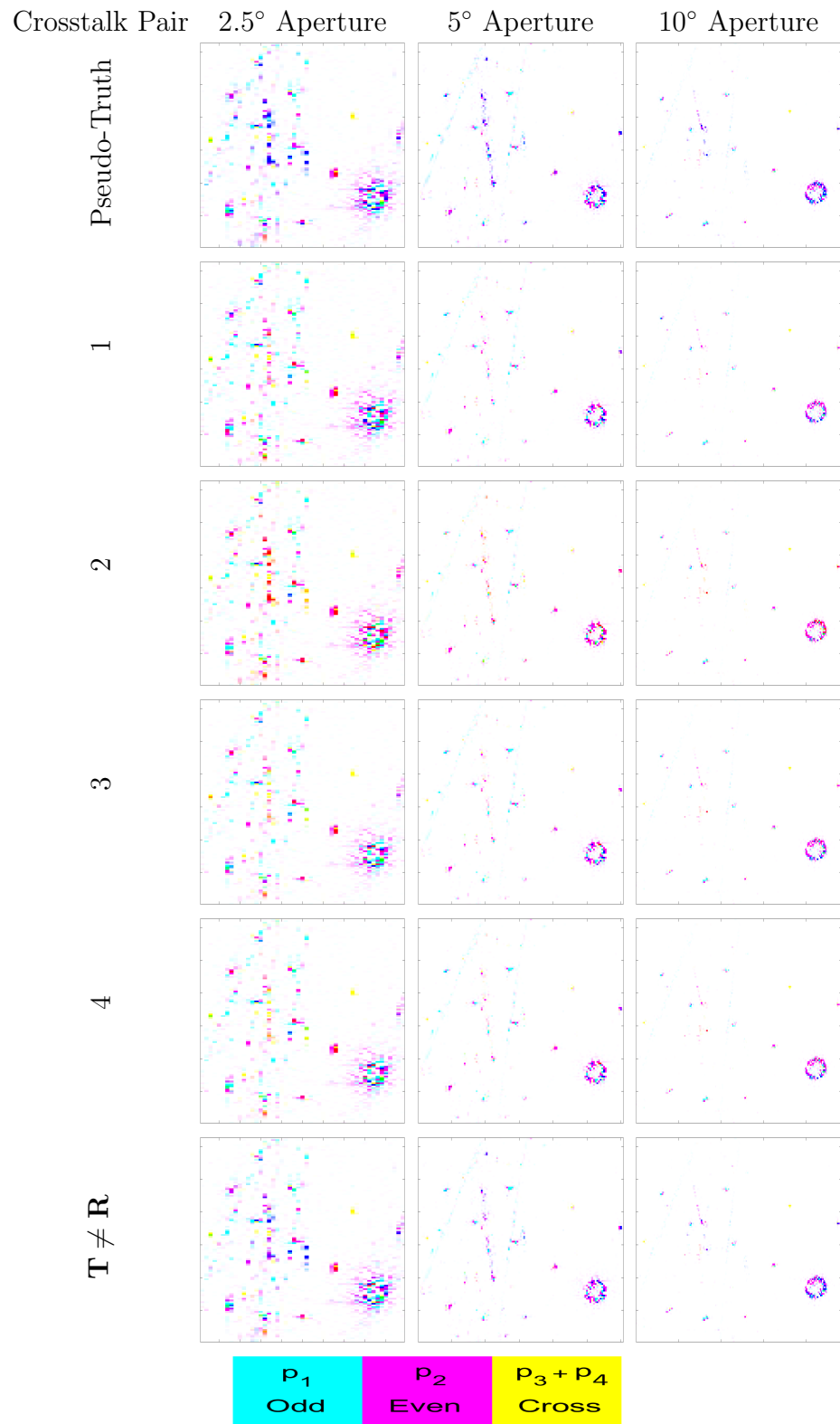


Figure 42. GOTCHA Calibration Sub-scene CMY Results

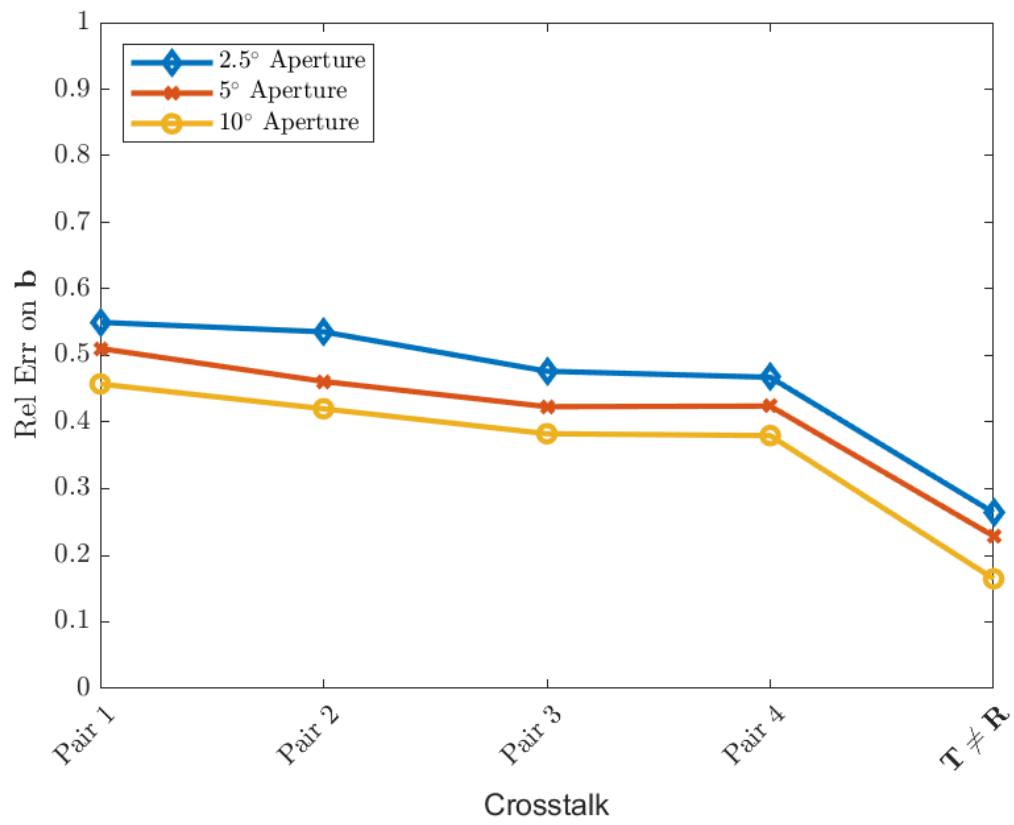


Figure 43. Relative ℓ_2 error of GOTCHA sub-scene for each crosstalk pair.

Figures 42 and 43 show generally poor recovery of the pseudo-truth scene for the $\mathbf{T} = \mathbf{R}$ robustness points in pairs 1–4 and good recovery for the $\mathbf{T} \neq \mathbf{R}$ case. The first 4 crosstalk pairs show a polarimetric shift in the recovery compared to the reference image. The shift is indicative of a poor recovery of the dropped HH channel. Further evidence of a poor recovery can be seen in the lower intensity of crosstalk pairs 1–4. Despite excellent performance on the synthetic scenes, the top four crosstalk points struggle with the GOTCHA-like sub-scene. The approximate target density of the GOTCHA scene is 13%.

In the $\mathbf{T} = \mathbf{R}$ cases, there may not be enough diversity in the crosstalk values to sufficiently spread the information such that it can be recovered via BPDN when so many targets are so close together in small areas of the scene. When the restriction of $\mathbf{T} = \mathbf{R}$ is relaxed, a better recovery is achieved. Comparing the $\mathbf{T} \neq \mathbf{R}$ case in the bottom row of Figure 42 to the pseudo-truth shows a significantly lower error. The evidence of polarimetric shifting and reduced target intensity are absent from the $\mathbf{T} \neq \mathbf{R}$ results which are shown in Figure 41 to be more robust to denser target scenes than the $\mathbf{T} = \mathbf{R}$ case.

3.4 Conclusions

The dropped-channel PolSAR CS method demonstrates excellent robustness – 76% of the magnitude-only crosstalk point tests achieved an average relative recovery error of less than 0.1. Furthermore, the inclusion of phase information did not cause any significant negative impact to the recovery performance. Thus, it is safe to use the zero-phase results as a guide for a future antenna design knowing that any phase crosstalk will be acceptable for the system. The performance drops above 3% sparsity in the $\mathbf{T} = \mathbf{R}$ recoveries for the simulated point target scenes, along with the improved performance of the $\mathbf{T} \neq \mathbf{R}$ recovery at higher target densities further inform the need

for either two antennas, or the inclusion of active components in a single antenna for application in real-world scenarios. While a good robustness region is identified, the corresponding crosstalk values of that region are much higher than design crosstalk of typical radar antennae. We have determined that a novel antenna design would be beneficial to the dropped-channel PolSAR model and have shown a forgiving area of crosstalks over which that antenna could be designed to. Determining the robustness of the model removes a significant burden from the antenna design problem. Knowing a larger robustness region exists gives more leeway to antenna design parameters and more allowances for manufacturing defects and mismatches.

We observed that the mutual coherence is not a useful predictive metric for the dropped-channel PolSAR model due to the structure of the model as compared to the more random nature of other CS measurement matrices. By introducing the SXR, we are able to find a better predictive measurement that is only dependent on the known crosstalk matrix.

IV. Dropped-Channel System Microstrip Antenna Design

The robustness region of -9 dB to -3 dB determined in Chapter 3 is much higher than PolSAR antennae are typically designed for. To give further credibility to the drop channel PolSAR model and to help start bridging the gap from theory to practice, a new antenna is required. In this chapter, a high crosstalk antenna is designed, simulated, built, and measured. The size of the robustness region provides flexibility to account for trade-offs in the design as well as provide a buffer zone for manufacturing defects.

4.1 Dropped-Channel PolSAR Antenna Design

The initial design of the prototype antenna was done with the consult of AFR-L/RMYF's sub-CTC lead for low-cost multifunctional RF sensing, Jeff Massman. Based on the manufacturing capabilities, connector types, and measurement capabilities available, a dual-pol S-band antenna is designed in Ansys HFSS. Figures 44 and 45 show the final antenna design in HFSS [106].

A center resonant frequency (f_r) of 3 GHz is chosen as it is the middle of S-band. The desired bandwidth is 10% of f_r , giving $B = 300$ MHz, which is on the high end of microstrip bandwidths without incorporating complex designs [79]. An $h = 1.524$ mm thick Rogers RO4350 substrate, with permeability $\epsilon_r = 3.66$, is chosen for availability reasons. First, [73, Eq 14-6] is used to determine the width of the patch.

$$W = \frac{1}{2f_r\sqrt{\epsilon_0\mu_0}}\sqrt{\frac{2}{\epsilon_r + 1}} = \frac{\nu_0}{2f_r}\sqrt{\frac{2}{\epsilon_r + 1}} = 2.5691 \text{ cm} \quad (41)$$

where ν_0 is the free space speed of light in cm/s^2 . Next the effective dielectric constant

is computed as

$$\epsilon_{r,eff} = \frac{\epsilon_r + 1}{2} + \frac{\epsilon_r - 1}{2} \left[1 + 12 \frac{h}{W} \right]^{-1/2} = 3.3954 \quad (42)$$

using the above, [73, Eq 14-2] can be used to determine the extension of length as

$$\Delta L = 0.412h \frac{(\epsilon_{r,eff} + 0.3) \left(\frac{W}{h} + 0.264 \right)}{(\epsilon_{r,eff} - 0.258) \left(\frac{W}{h} + 0.8 \right)} = 0.0722 \text{ cm.} \quad (43)$$

Finally, the radiating length of the patch can be solved for using

$$L = \frac{\nu_0}{2f_r \sqrt{\epsilon_{r,eff}}} - 2\Delta L = 2.6079 \text{ cm} \approx 2.5691 \text{ cm.} \quad (44)$$

Being a dual-pol microstrip antenna, L was used for both sides, leaving a square microstrip antenna. The starting location of the feed pins was centered along their respective sides and in-set about 1/4 of the distance to the center of the patch (Jeff Massman, personal communication, July 2021). The feed pin diameters were set to 1.27 mm as that is the size of the coax pins on the available SMA connectors. A 1 mm shorting pin was initially placed in the center as good RF engineering practice to ensure that the center of the microstrip antenna has zero current as expected. The shorting pin was then offset diagonally from the center away from the feed pins to help tune the crosstalk level. A ground plane of length $L_g = 6(h + L) \approx 165\text{mm}$ was used as it is effectively seen as an infinite ground by the patch antenna [107]. The final offset for the coax pins is 12.1191mm from the center. The shorting pin offset is 3.969375mm diagonally from center.

The final antenna values were the result of an optimization performed by HFSS. The variables available for the optimizer to change were the patch length (L), the shorting pin offset, and the coax offset. The coax pins were offset the same dis-

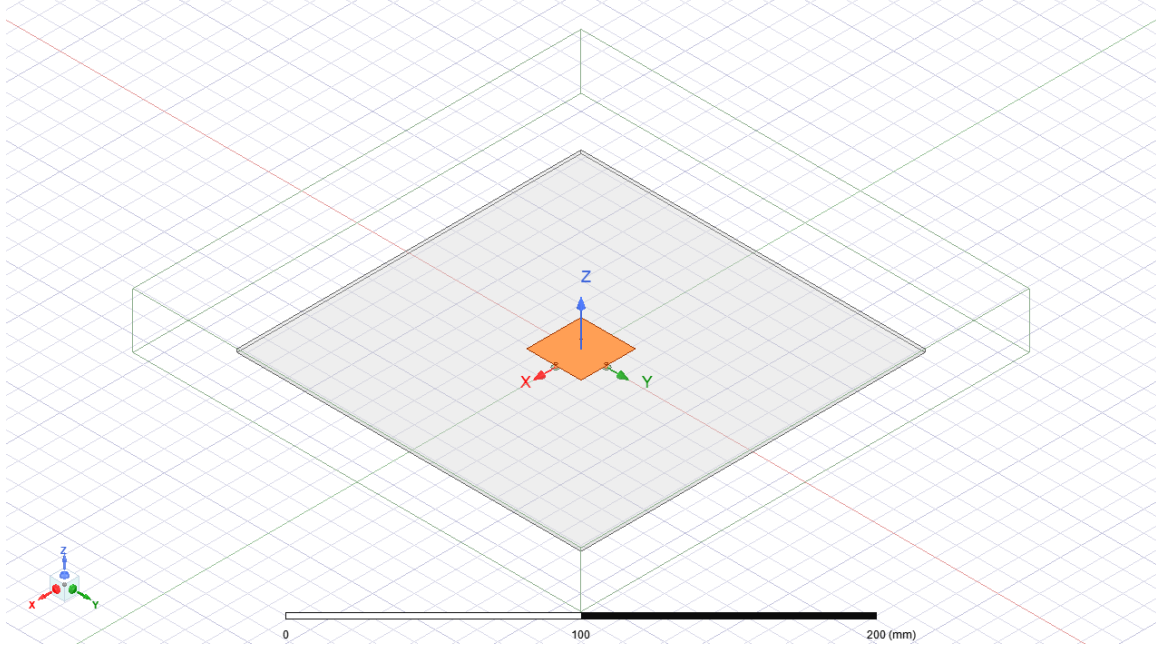


Figure 44. S-band Antenna Model in HFSS, Isometric View

tance to preserve symmetry, which is the same reason the shorting pin was moved diagonally. The optimization algorithm used was the Adaptive Multiple Objective (Random Search). This algorithm combines some aspects of machine learning and gradient descent to perform the optimization. Two equations were used to set the optimization goals and both were given the same weight. The first was $S_{1,1} \leq -10$ dB on the frequency range 2.8–3.2 GHz, the second was Realized Gain θ (dB) – Realized Gain ϕ (dB) = 6 dB at bore sight ($\theta = 0^\circ$, $\phi = 0^\circ$) and a frequency of $f_r = 3$ GHz. Realized gain is used as it accounts for impedance mismatch and losses. Recall from Chapter 2 that the difference between the realized gain θ and realized gain ϕ is analogous to the crosstalk level in the transmit crosstalk matrix.

Figure 46 shows the simulated S-parameters for the optimized S-band antenna in HFSS. The $S_{1,1}$ notch at 3 GHz suggests a good impedance match in the antenna design. In fact, most of the desired 2.85 – 3.15 GHz bandwidth is below -10 dB in $S_{1,1}$, with the exception of approximately 100 MHz on the low end and a few 10s of

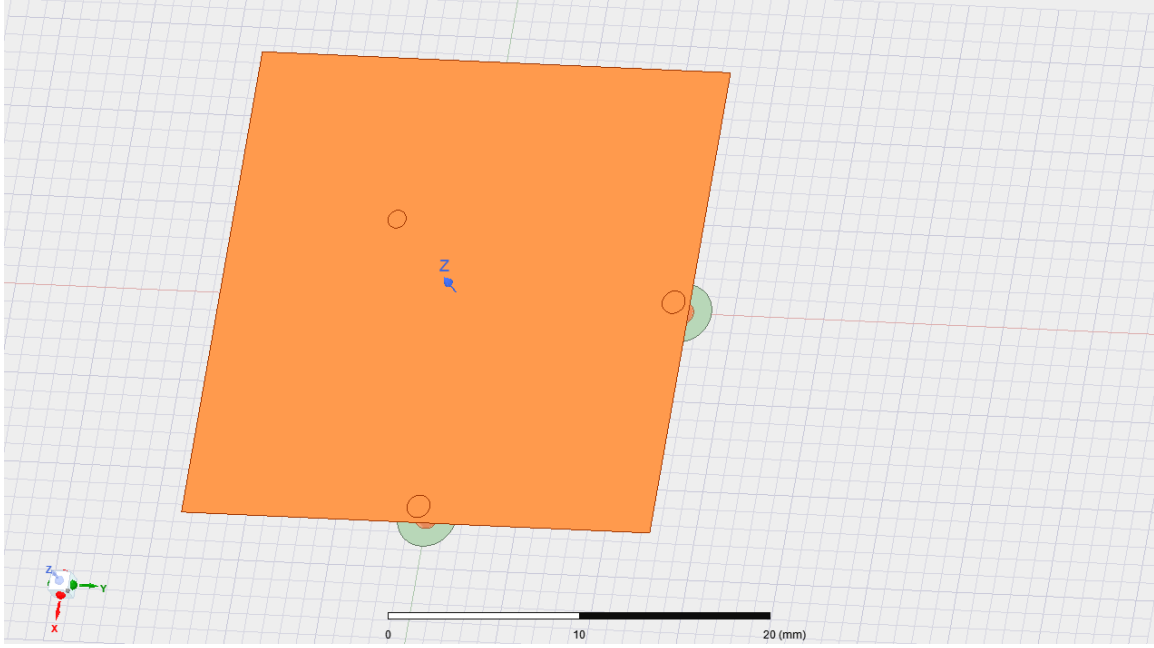


Figure 45. S-band Antenna Model in HFSS, Close-up View

MHz on the high end. Additionally, the $S_{2,1}$ match is poor as desired. Across the bandwidth, $S_{2,1}$ shows a high degree of coupling between Port 2 (V pol) and Port 1 (H pol), which is indicative of the desired high crosstalk. Since the antenna is symmetric, the $S_{1,1}=S_{2,2}$ and $S_{2,1}=S_{1,2}$ as expected.

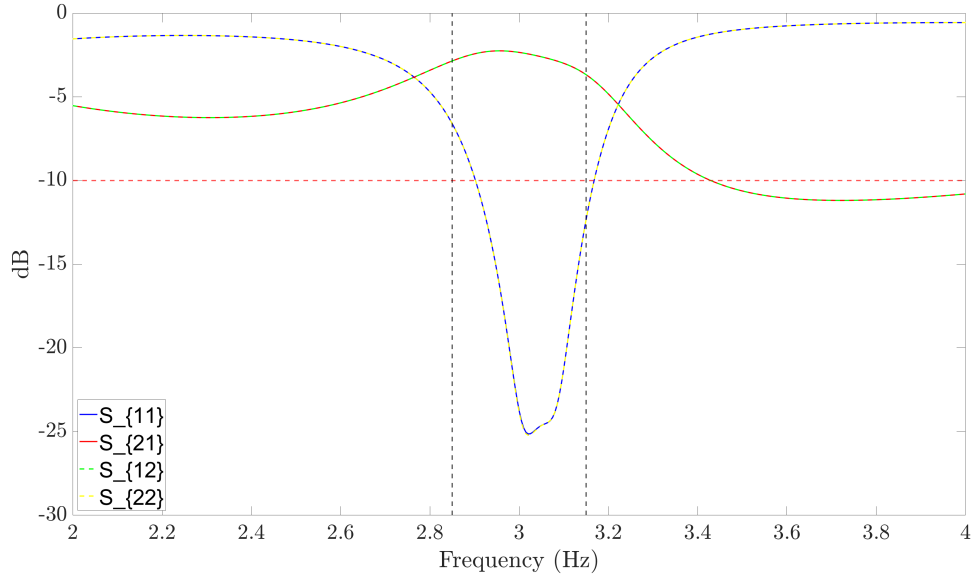


Figure 46. All 4 S-parameters from HFSS model of S-band antenna. Horizontal red line shows the S_{11} goal and the vertical black lines show the desired bandwidth.

Figure 47 shows the E-plane boresight realized gain as a function of frequency for a Port 1 (H pol) excitation. The blue line is the realized gain θ -cut (co-polar). The red line is the realized gain ϕ -cut (cross-polar). The yellow line is the difference between the θ and ϕ realized gains. The marker shows that a difference of -5.2023 dB at 3 GHz was achieved, which is within the robustness region of -9 dB to -3 dB determined in Chapter 3. The shape of the boresight gain shows the bandwidth and shows the narrow band nature of microstrip antenna. The gain is highest over the bandwidth, or perhaps just above it, and tapers noticeably outside of that frequency region. The center of the gain plateau is approximately over 3.1 GHz, which may mean that the optimization process has shifted the natural resonant frequency of the antenna. Addressing the potential shift in center frequency, specifically a potential shift this small is beyond the scope of this research effort.

Figure 48 shows a polar plot of the Port 1 (H pol) θ and ϕ patterns, taken at the $\phi = 0^\circ$ (E-plane) cut and 3 GHz. At the center frequency, a well-behaved and typical

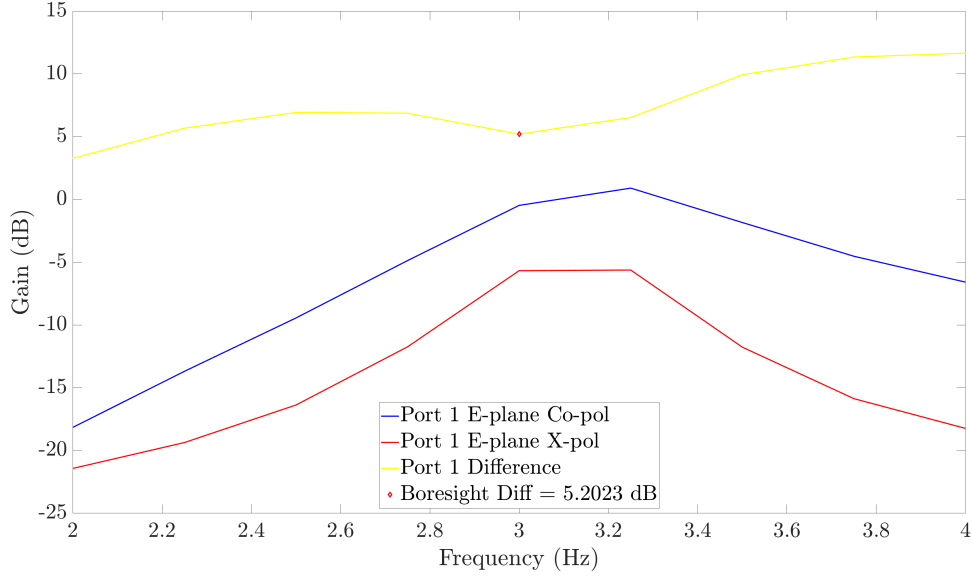


Figure 47. HFSS modeled Port 1 realized gain sweep across frequency at boresight in E-plane.

pattern shape [73] for a patch antenna is observed, with the exception of the higher crosstalk of course. Figure 49 shows the a polar plot of the θ and ϕ patterns, taken at the $\phi = 90^\circ$ (H-plane) cut and 3 GHz. Again the pattern is wide as is expected for a microstrip antenna. As a sanity check, the values at boresight (0° on polar plot) should be identical between the E-plane and H-plane patterns. The co-polar value at boresight of both E-plane and H-plane is -0.4759 dB, and the cross-polar value for both fields at boresight is -5.6782 dB, thus confirming the validity of the patterns.

Figure 50 shows the E-plane boresight realized gain as a function of frequency for a Port 2 excitation. As before, the blue line is the co-polar gain, the red line is the cross-polar gain, and the yellow line is the difference between the co-polar and cross-polar gains. The marker shows that a difference of 5.1595 dB at 3 GHz was achieved, which is equivalent to $\delta_1 = -5.1595$ and still within the robustness region of -9 dB to -3 dB determined in Chapter 3, but not the same as in Figure 47. Thus, Figures 47 and 50 are similar, but not identical. For the intents and purposes of the

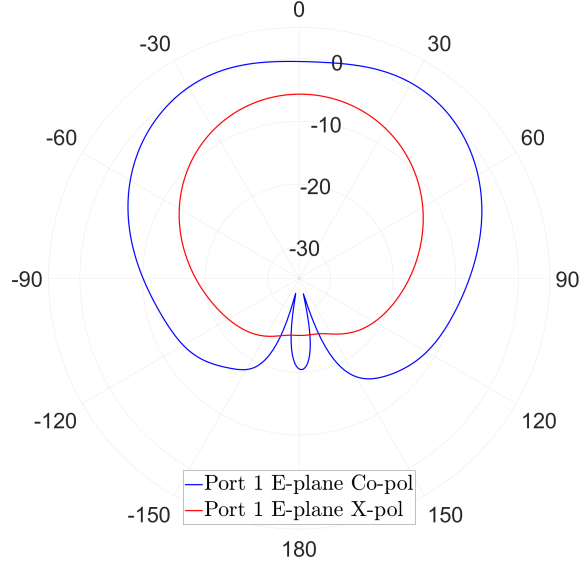


Figure 48. HFSS modeled Port 1 realized gain at 3GHz, Polar Plot, E-plane.

prototype, proof-of-concept antenna, these values are close enough though.

Figure 51 shows a polar plot of the Port 2 (V pol) θ and ϕ patterns, taken at the $\phi = 90^\circ$ (E-plane) cut and 3 GHz. Figure 52 shows the a polar plot of the θ and ϕ patterns, taken at the $\phi = 0^\circ$ (H-plane) cut and 3 GHz. The patterns are very similar to the Port 1 (H pol) examples in Figures 48 and 49, as expected. The co-polar value at boresight of both E-plane and H-plane is -0.4816 dB, and the cross-polar value for both fields at boresight is -5.6411 dB, thus confirming the validity of the patterns. With the antenna modeled, optimized, and characterized, it was ready to be manufactured and tested.

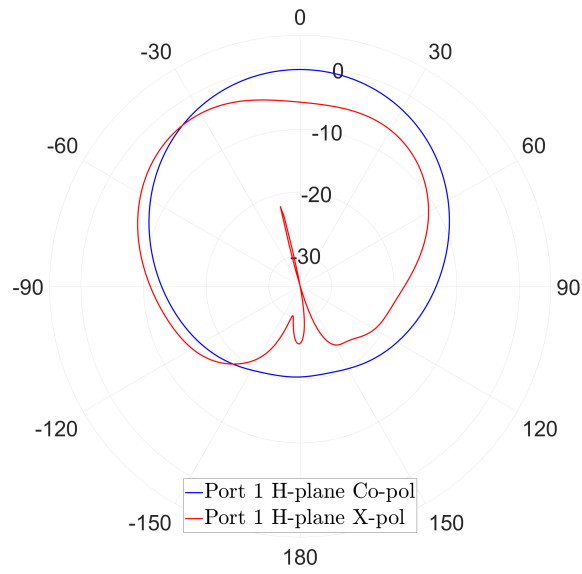


Figure 49. HFSS modeled Port 1 measured gain at 3GHz, Polar Plot, H-plane.

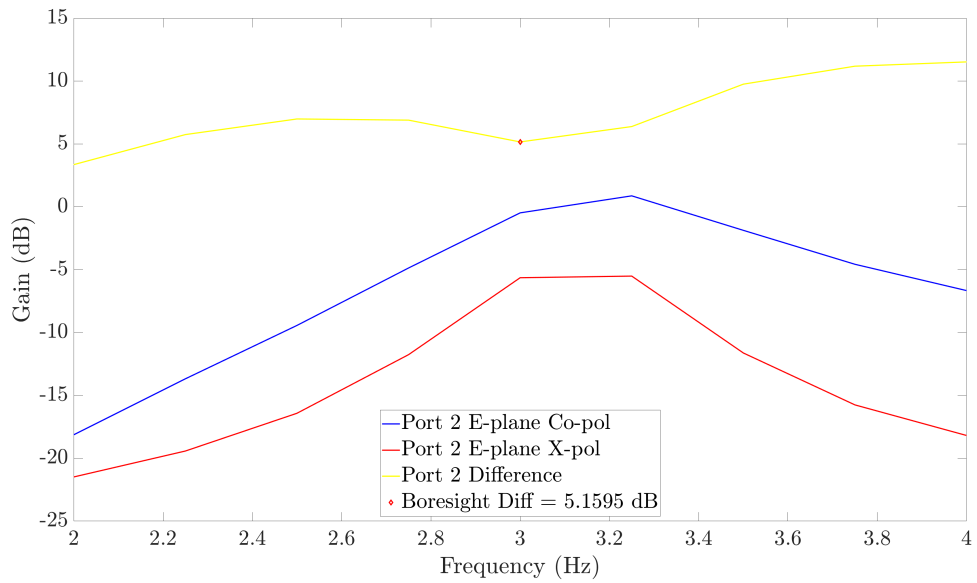


Figure 50. HFSS modeled Port 2 realized gain sweep across frequency at boresight in E-plane.

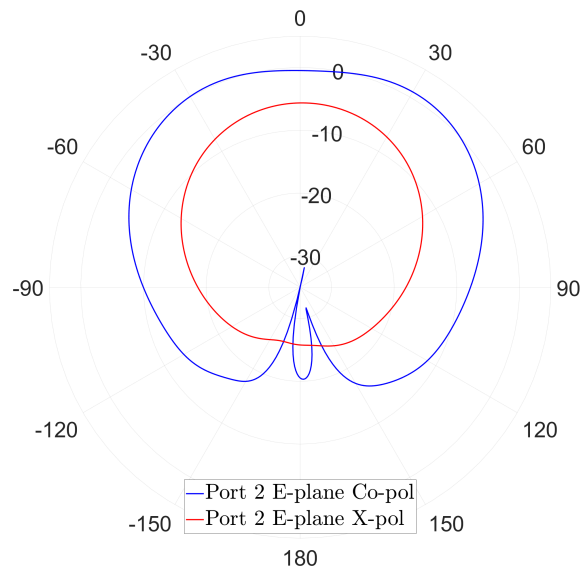


Figure 51. HFSS modeled Port 2 realized gain at 3GHz, Polar Plot, E-plane.

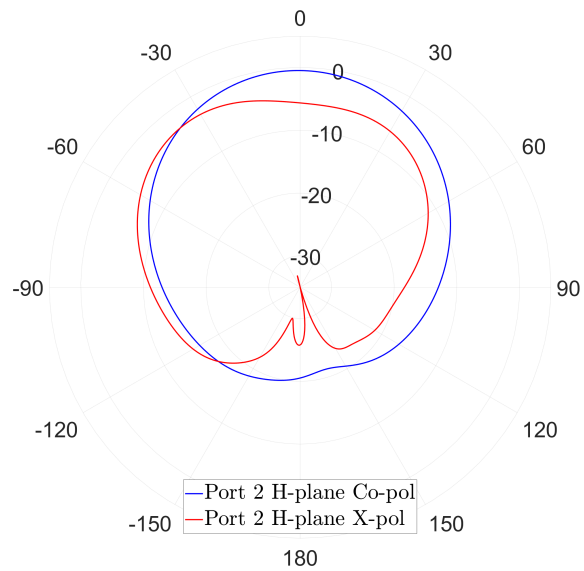


Figure 52. HFSS modeled Port 2 measured gain at 3GHz, Polar Plot, H-plane.

4.2 Drop-Channel PolSAR Antenna Measurements

The designed S-band antenna was built in the AFRL/Rymf ATEMS lab. Figures 53–55 show the constructed antenna from various angles. While the shape and pin holes were able to be cut on a CNC mill, the pins and SMA connectors had to be soldered on by hand. As can be seen in Figures 53–55, the soldering job is a bit messy, but manufacturing defects is a big reason for looking at robustness instead of optimization.



Figure 53. Constructed S-band antenna, top view.

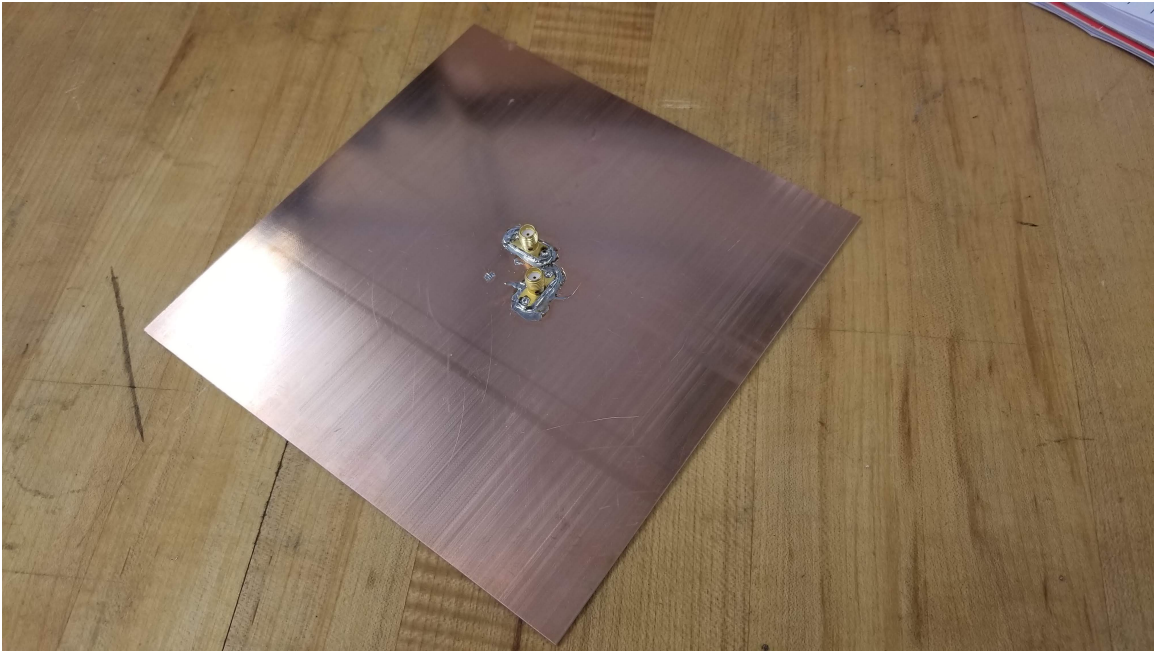


Figure 54. Constructed S-band antenna, back view.



Figure 55. Constructed S-band antenna, close-up view.

To prepare for the antenna measurements, the range was first calibrated using a RFSpin QRH18 Quad Ridged Broadband Horn Antenna as shown in Figure 56. The measurement software uses the known horn's parameters and automated test fires based on the desired testing sequence to calibrate the measurement horn, shown in Figure 57, in preparation for the test antenna. The measurement horn is also a RF-Spin QRH18 and is set to receive. The received measurements were captured using an Agilent Technologies E8364C PNA Network Analyzer connected to the measurement horn and the data was recorded in a custom software that controls the test stand, antenna positioner, the measurement horn, and the test antenna.

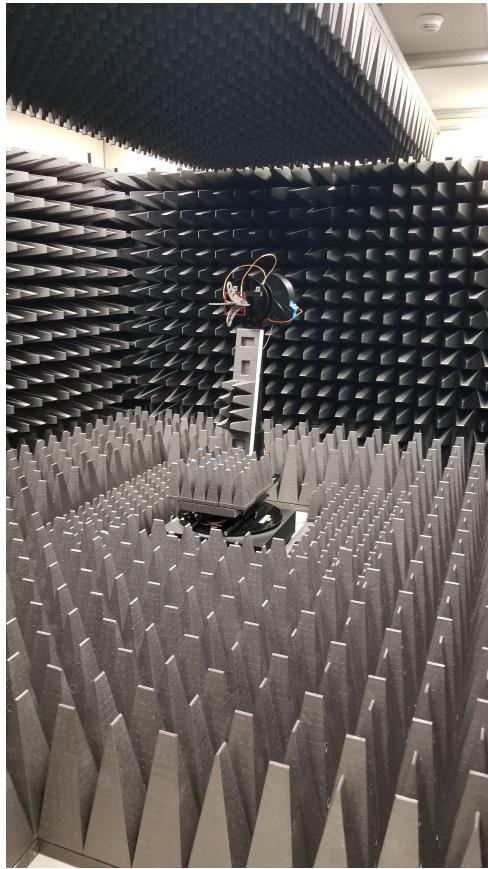


Figure 56. Calibration horn on the test stand.



Figure 57. Measurement horn in AFRL/RYMF ATEMS lab.

Once the measurement equipment was calibrated, the S-band antenna was affixed to the test stand as shown in Figure 58. For the test, we assumed port 1 was the “H” port and port 2 was the “V” port. In Figure 58, Port 2 (V pol) is down towards the base of the test stand and Port 1 (H pol) is to the right. The label for Port 1 (H pol) is covered by the strip of tape in the figure. Painters tape was used to attach the antenna to the mounting plate because it is electromagnetically invisible at the test frequencies. For each test, the port under test was oriented on the bottom, i.e. since Port 2 (V pol) is down in Figure 58, Port 2 (V pol) was being tested when that picture was taken. Two test were performed, one for each port.

The goal of the chamber test is to measure the principle plane gain patterns. For each test, the S-band patch is the test antenna setup in the transmit mode. The

test stand is rotated in azimuth over $\phi \in [-90^\circ, 90^\circ]$ in 2 degree steps. At each azimuth step, a known signal is transmitted from the S-band patch from 2–4 GHz. The network records the E-field and H-field gain measured by the H pol port and V pol port of the measurement horn at each frequency value in the sweep. When the test stand reaches the end of the azimuth range, the antenna is rotated 90° on the stand and the measurements are repeated for the other port. When both ports have been tested, the principle plane gain patterns can be built from the measured data.

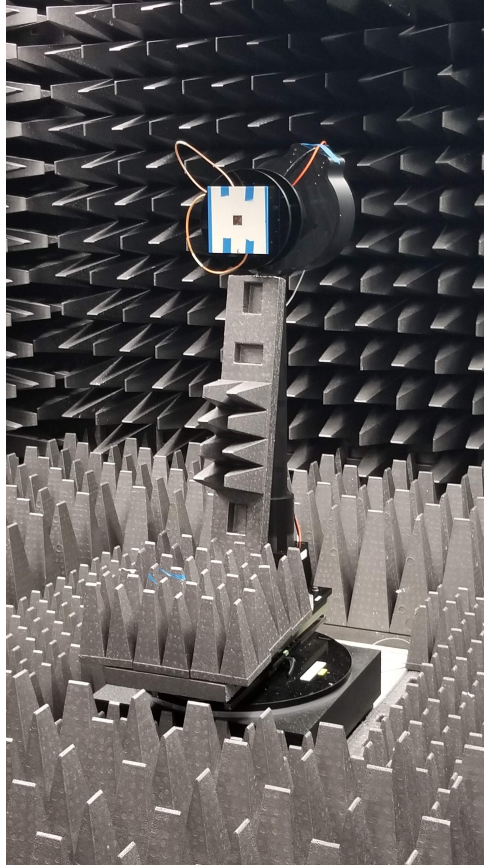


Figure 58. S-band antenna on test stand in ATEMS lab range.

To test the S-parameters, we again used the Agilent E8364C PNA. The PNA was disconnected from the measurement horn and set up to accept the test antenna directly. Once the necessary connectors were connected, the PNA was calibrated using the Agilent Technologies 85520A Calibration Kit. Once the PNA was calibrated for

the new cabling and adapters, the S-band antenna was connected as seen in Figure 59. All four S-parameters were measured from 2–4 GHz and the data was exported to a .csv file for further processing.

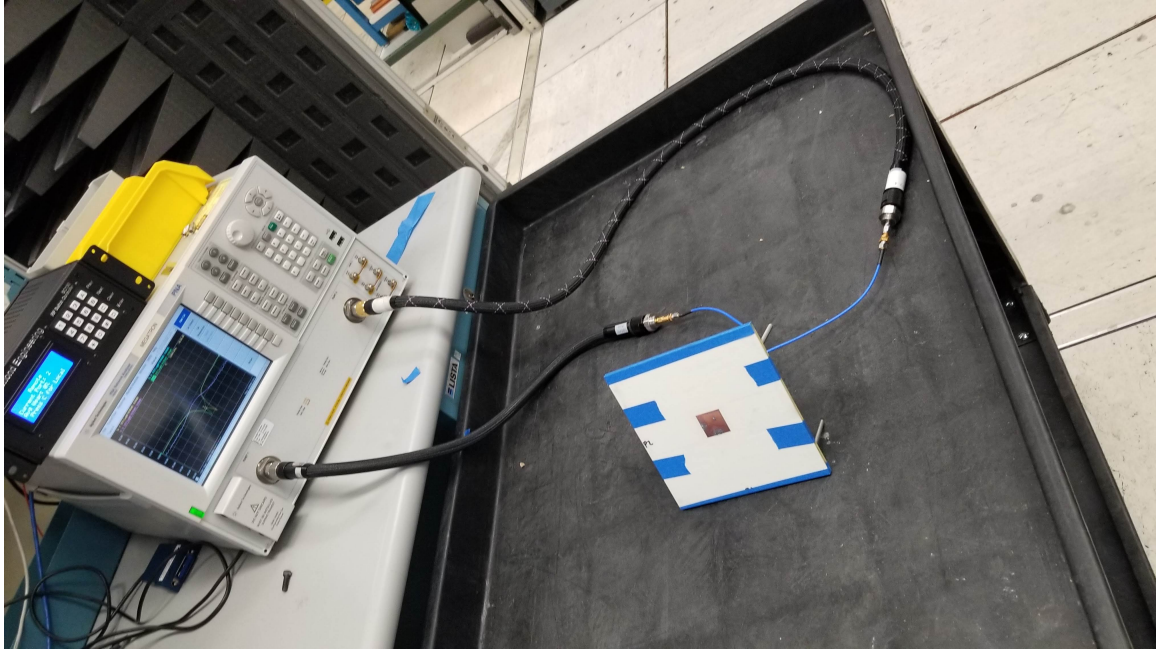


Figure 59. S-band antenna connected to Agilent PNA for S-parameter measurement.

Figure 60 shows the measured S-parameters overlaid with the HFSS modeled S-parameters. Generally, the measured results resemble the HFSS results, indicating that the antenna was constructed is close to the model. Note that the measured $S_{1,1}$ and $S_{2,2}$ are no longer the same. Small manufacturing defects have disrupted the symmetry. Similarly, the $S_{2,1}$ and $S_{1,2}$ are not equal, but fairly close together, particularly over the designed bandwidth.

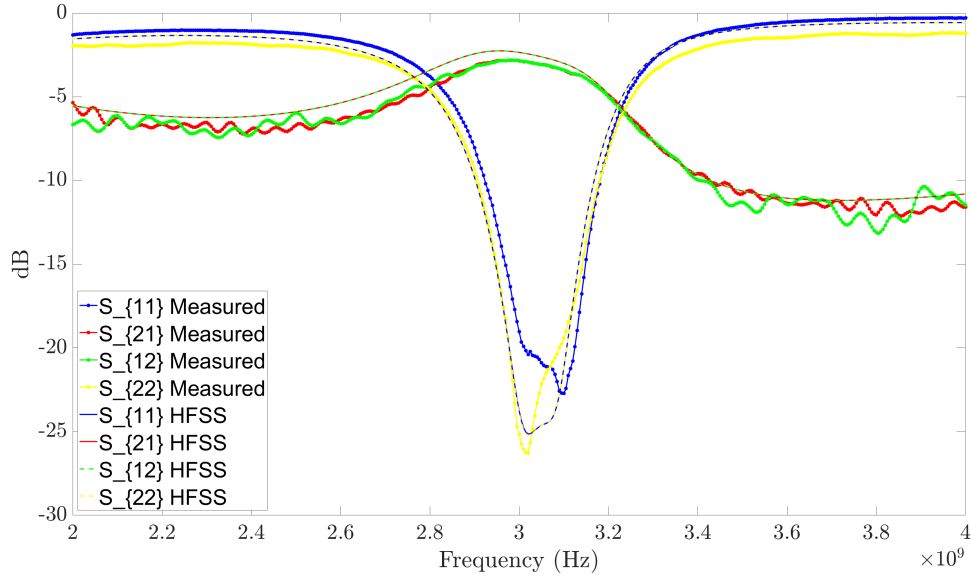


Figure 60. Measured S-parameters from constructed S-band antenna compared with HFSS model S-parameters.

4.2.1 Measurement Data Compared with Model - Port 1.

Figure 61 shows the E-plane measured gain at boresight over the frequency range 2–4 GHz for Port 1 (H pol), overlaid with the same information from Figure 47. The measured data follows the same trend as the HFSS data, but the crosstalk level is much higher. The difference in measured co-polar and cross-polar gain at 3 GHz is 1.4404 dB, much higher than the 5.2023 dB of the HFSS data. Taken as a zero-phase value, the measured crosstalk for Port 1 (H pol) is equivalent to a $\delta_1 = -1.44$ dB which is out of the robustness region of -9 dB to -3 dB. However, the measured gain is complex, which will help with recovery performance. Ultimately, the constructed antenna is a proof-of-concept and is what it is. More accurate construction techniques are possible, but would have required off-site manufacturing. Sending the antenna out to be made would have incurred unknown schedule delays and cost increases, neither of which could be afforded.

Figure 62 shows a polar plot of the measured and HFSS data for Port 1 (H pol) E-

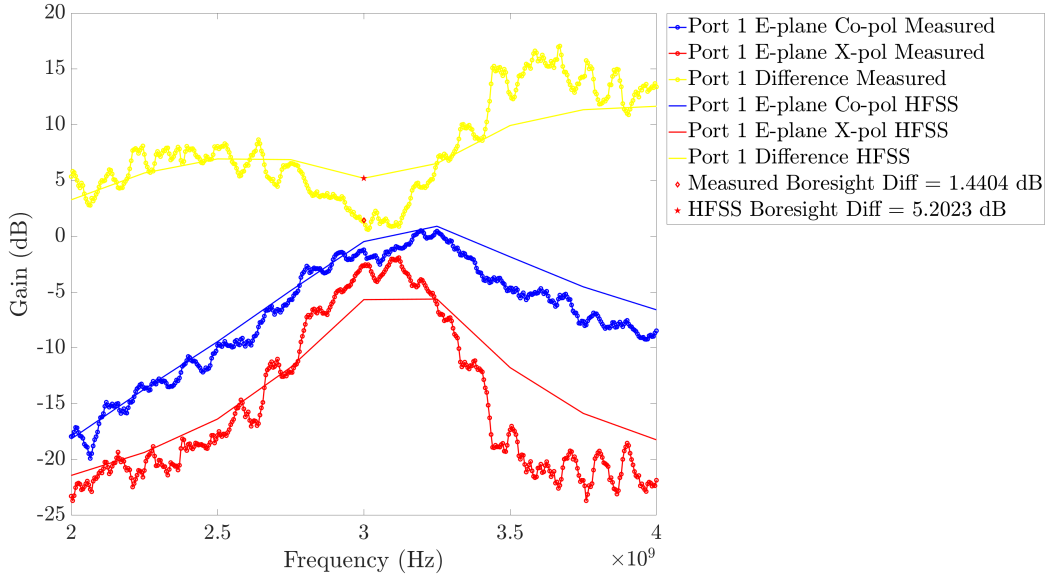


Figure 61. Port 1 measured gain sweep across frequency at boresight in E-plane compared with HFSS model.

plane co-polar and cross-polar gain at 3 GHz from -90° to $+90^\circ$. Figure 63 shows the corresponding polar plot for the H-plane. In the E-plane, the measured data pattern follows the HFSS pattern well, but with higher crosstalk all around. Interestingly, the measured data seems to show a co-polar gain dip at boresight. As shown by the HFSS data, the patch pattern should be mostly uniform over -30° to $+30^\circ$ in azimuth, but the measured data shows a dip in gain at boresight. The dip is a likely indication of an imperfect alignment on the test stand.

The difference between measured and modeled patterns is more obvious in Figure 63. The cross-polar gain seems to follow the same trend as the HFSS pattern, but the level is much higher. To the point that, even though the measured co-polar gain follows the HFSS pattern well, the overall picture is different due to the cross-polar gain being higher in amplitude than the co-polar gain for most of the azimuth region measured. Additionally, since Figures 62 and 63 are on the same scale, it is easily seen that the measured data are not identical at boresight. The difference between

the E-plane and H-plane co-polar gain at boresight is 0.5116 dB and the difference in cross-polar gain is 0.0180 dB. The small difference in gain at boresight points towards measurement error. Likely the antenna was not perfectly flat on the stand such that an H-plane measurement was a slightly different angle than an E-plane measurement.

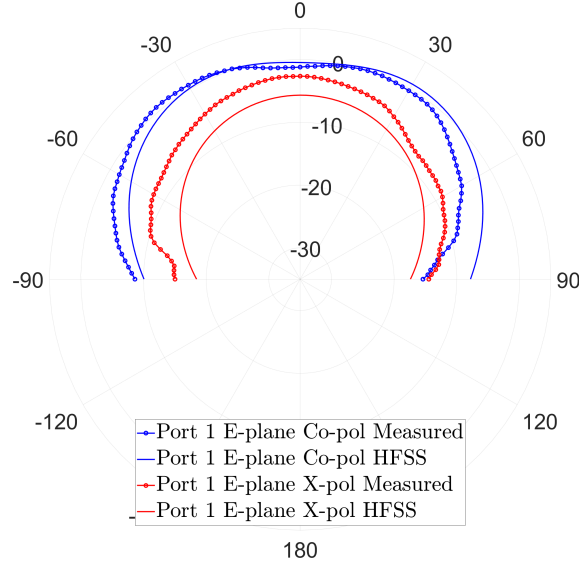


Figure 62. Port 1 measured gain at 3GHz, Polar Plot, E-plane compared to HFSS results.

4.2.2 Measurement Data Compared with Model - Port 2.

Figure 64 shows the E-plane measured gain at boresight over the frequency range 2–4 GHz for Port 1 (H pol), overlaid with the same information from Figure 50. As with the Port 1 (H pol), the measured data has the same trend as the HFSS data but with a higher crosstalk. The crosstalk delta in Port 2 (V pol) is 2.3603 dB, which is closer than Port 1 (H pol) to the original designed value of 6 dB. The measured data also tapers much quicker above the top end of the bandwidth than the HFSS data, further demonstrating the narrow bandwidth properties of a typical microstrip antenna.

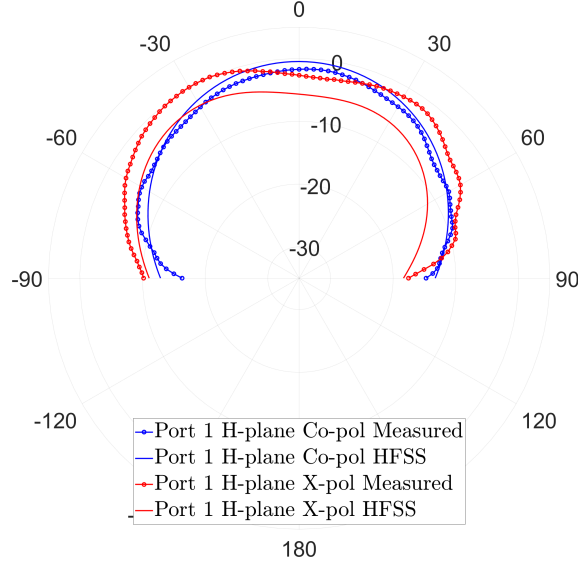


Figure 63. Port 1 measured gain at 3GHz, Polar Plot, H-plane compared to HFSS results.

Figure 65 shows the polar plot of the measured and HFSS data for Port 2 (V pol) E-plane co-polar and cross-polar gain at 3 GHz from -90° to $+90^\circ$. Figure 66 shows the corresponding polar plot for the H-plane. For the E-plane in Port 2 (V pol), the agreement between measured data and the model is very good. The co-polar gain lines are nearly identical and the cross-polar gain lines are very close on the range of $\pm 60^\circ$ with some anomalous behavior towards the fringes of the measurement interval.

A much larger departure is observed in the H-plane results in Figure 66. The co-polar lines follow the same trend, but the measured gain is noticeably lower. From -90° to boresight, the cross-polar lines are close, but from boresight to $+90^\circ$, the measured cross-polar gain is significantly higher. Again, the E-plane and H-plane results do not match at boresight due to likely measurement error. The difference between the E-plane and H-plane co-polar gain at boresight is 0.7216 dB and the difference in cross-polar gain is 1.5938 dB. The error is larger here, possibly the way in which the antenna was off in the Port 1 (H pol) case was amplified when the

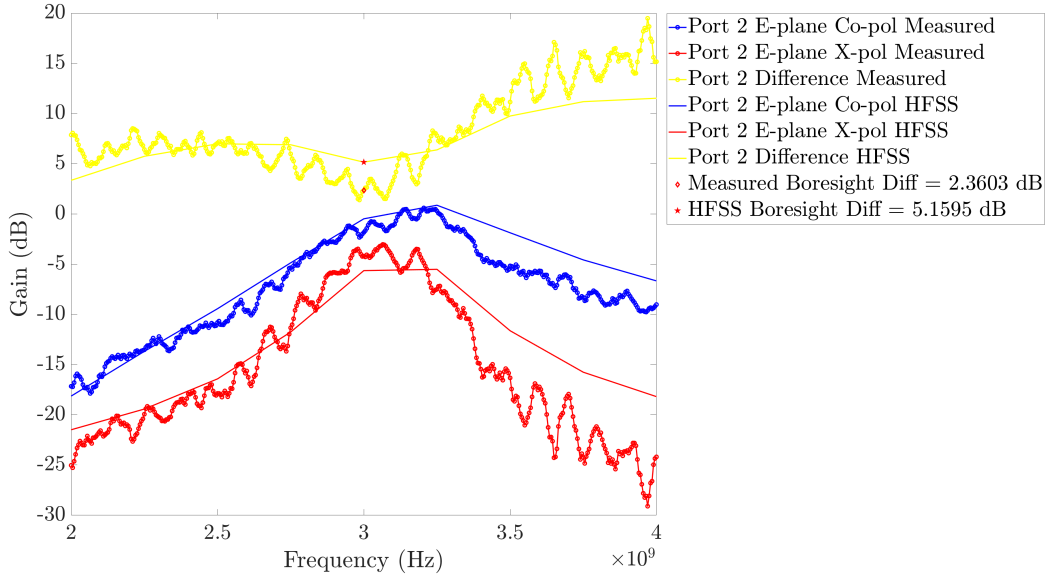


Figure 64. Port 2 measured gain sweep across frequency at boresight in E-plane.

positioner was rotated 90 degrees to do the Port 2 (V pol) measurement.

The lack of symmetry in the constructed antenna is favorable. Recall that the robustness region was much larger off the anti-diagonal in Chapter 2. By being somewhat asymmetric, the higher crosstalk in the real antenna is more tolerable. With the antenna now constructed and characterized, the values can be used in a sample synthetic scene to show that the proof-of-concept has merit in the dropped channel PolSAR model.

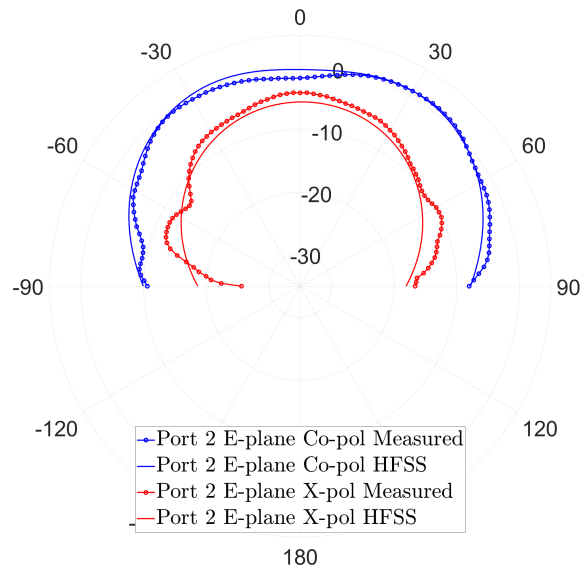


Figure 65. Port 2 measured gain at 3GHz, Polar Plot, E-plane compared to HFSS results.

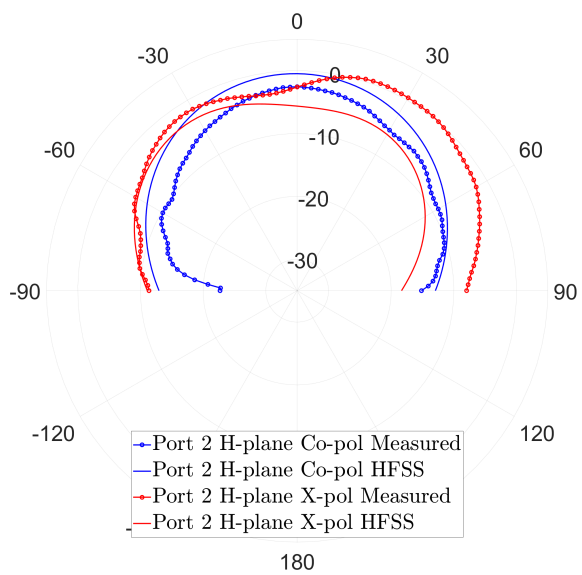


Figure 66. Port 2 measured gain at 3GHz, Polar Plot, H-plane compared to HFSS results.

4.3 BPDN Results using Measured Antenna Crosstalk

In order to use the measured antenna results in the drop channel PolSAR model, some assumptions will be required. First, assume that the antenna is the sole source of crosstalk in the system. Further, assume that only the boresight values are used in the transmit matrix \mathbf{T} . By assuming boresight only, the direct values can be used instead of needing the Ludwig cross-pol definitions for off-boresight data [90]. Also assume that port 1 is the horizontal port and port 2 is the vertical port. Finally, assume that $\mathbf{T} = \mathbf{R}$ in a monostatic system.

In the previous section, the gain patterns were shown in dB magnitude as is customary for reporting antenna performance. However, the measured data is complex in nature, recorded as dB magnitude (shown in previous section as gain patterns), and angle. As previously discussed, phase crosstalk is nearly impossible to design into an antenna, so the measured phase value is not reported as there is no meaningful simulated value to compare with. The dB magnitude at 3 GHz boresight is converted to power and then combined with the angle value to provide a complex coefficient for the transmit crosstalk matrix. The transmit matrix can now be populated with the measured data as

$$\mathbf{T} = \begin{bmatrix} t_{HH} & t_{HV} \\ t_{VH} & t_{VV} \end{bmatrix} = \begin{bmatrix} \text{Port 1 co-pol} & \text{Port 1 x-pol} \\ \text{Port 2 x-pol} & \text{Port 2 co-pol} \end{bmatrix} \quad (45)$$

$$= \begin{bmatrix} 0.5746 - 0.4925i & 0.5432 + 0.0001i \\ 0.5327 + 0.3820i & 0.3802 + 0.0186i \end{bmatrix}. \quad (46)$$

The \mathbf{T} in (45) is then used to create the crosstalk matrix using (31). The crosstalk model is then used in dropped channel PolSAR model in (24) along with each of the aperture extents in Table 1. The deterministic scenes in Figure 15 were used to

test the ability of the measured antenna crosstalk in the model. Each scene at each aperture extent had the HH channel dropped and then recovered with BPDN. Recall that scenes 2 and 3 were specifically designed to stress the dropped channel PolSAR model.

Figure 67 shows the BPDN recovered scenes for the 2.5 degree aperture extent. Even though the 2.5 degree aperture is the hardest to recover, BPDN does good job on scenes 1 and 2. The bottom left string of targets in scene 3 was successful in tripping the model up though. The psf spreads the information too much in the horizontal string of targets and BPDN cannot recover them. Table 4 shows the relative ℓ_2 error (38) for each scene and aperture extent. In the 2.5 degree aperture extent, the second scene is almost within the 0.1 threshold for successful recovery, the first scene obviously is, and the third scene is over 5 times the higher than the 0.1 threshold. Despite the high recovery error, each target is still clearly visible and the recovery is driven by polarimetric errors.

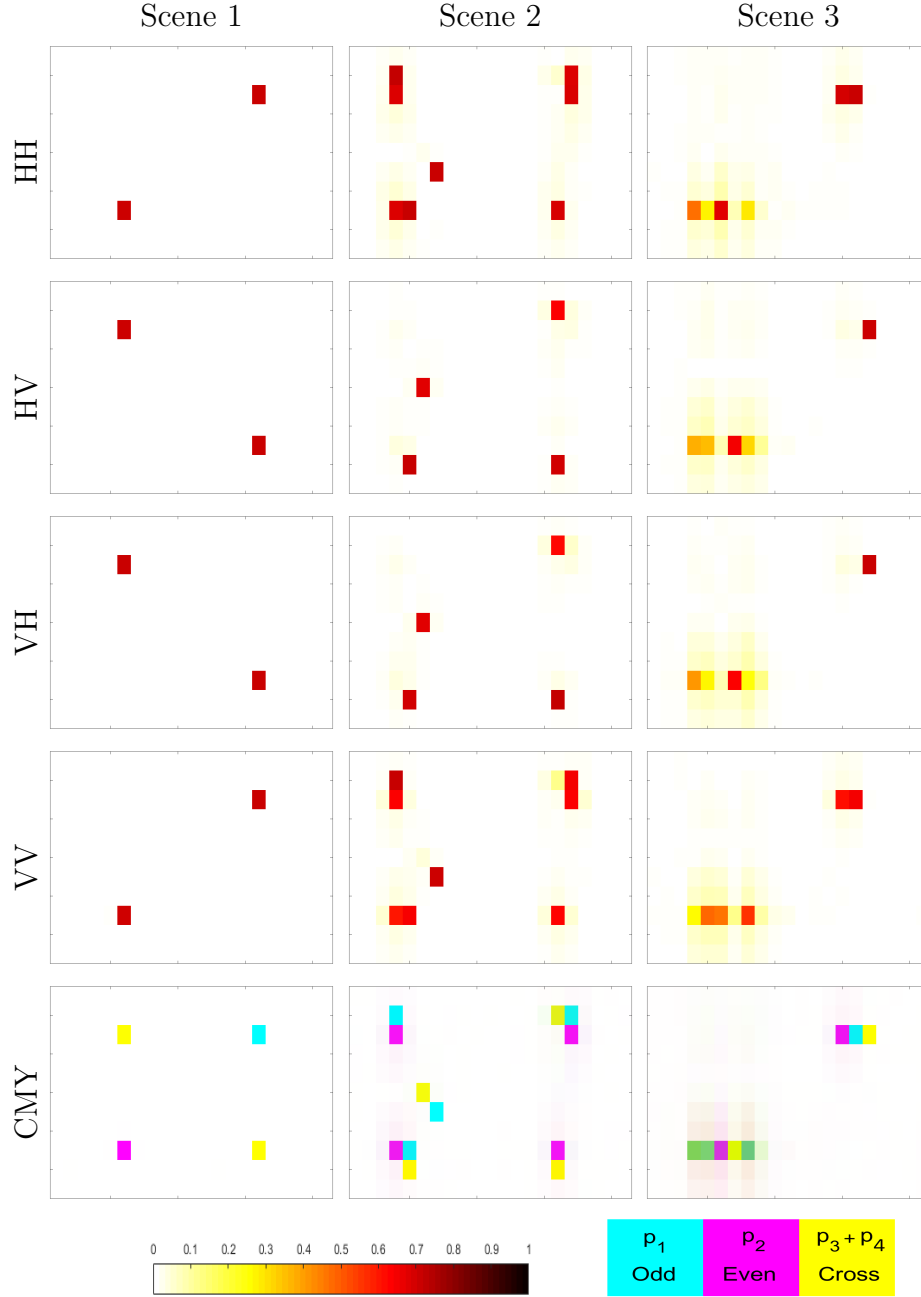


Figure 67. Recovered test scenes using measured antenna crosstalk matrix and 2.5° aperture extent.

Figure 68 shows the recovered scenes for the 5 degree aperture. Here BPDN was much more successful. Despite the crosstalk being higher than designed and the 5 degree psf still being fairly blurry, each scene is recovered nearly flawlessly. Table 4

further confirms the recovery success as the relative error for each recovery is much smaller than the 0.1 threshold used in the robustness study. Naturally, the 10-degree aperture results in Figure 69 are as good or better still. Table 4 confirms the superior recovery performance in the 10 degree aperture case with a recovery error significantly lower than the successful threshold. Figures 67-69 and Table 4 show that the high crosstalk antenna is a good fit for the dropped channel PolSAR CS model.

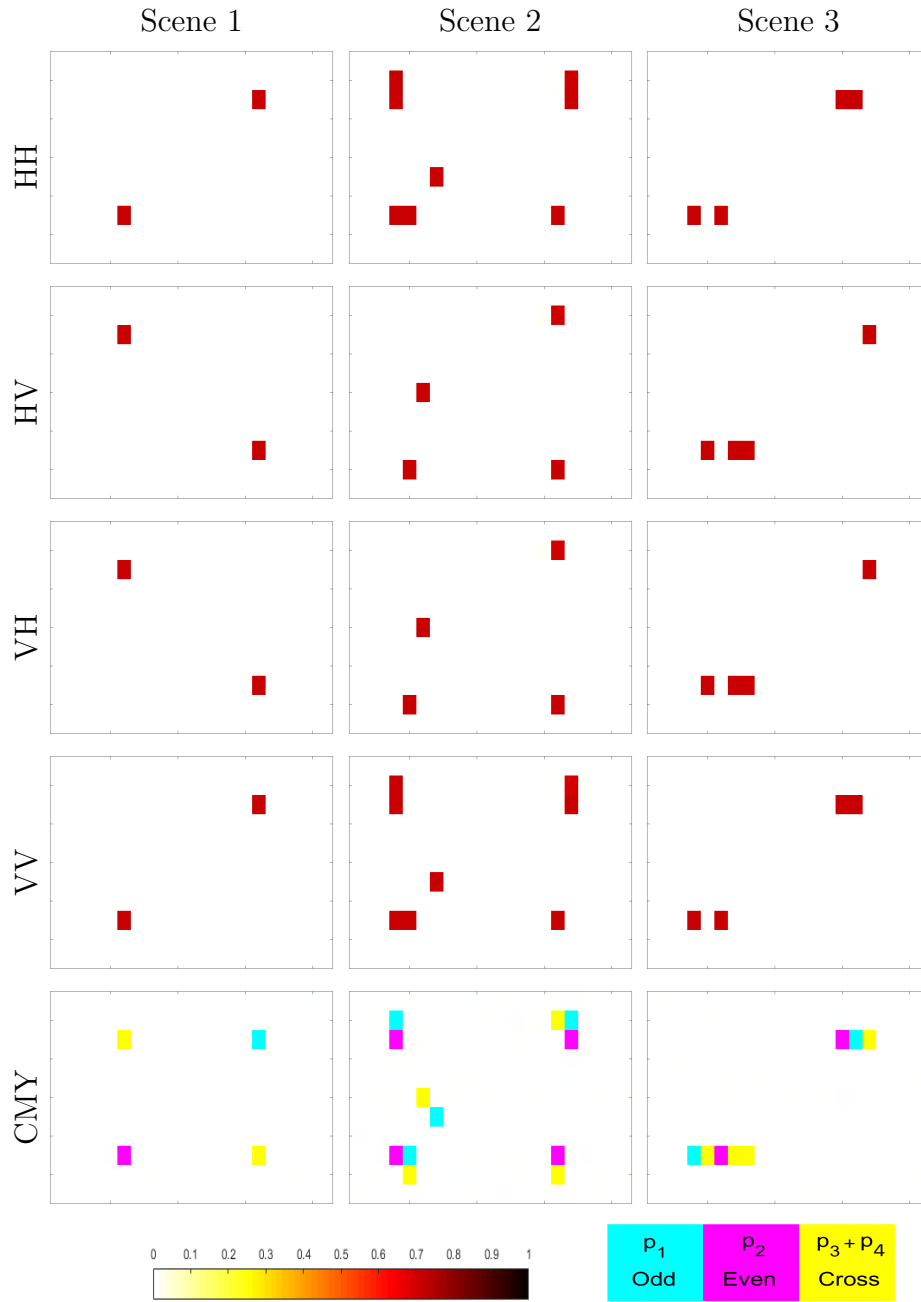


Figure 68. Recovered test scenes using measured antenna crosstalk matrix and 5° aperture extent.



Figure 69. Recovered test scenes using measured antenna crosstalk matrix and 10° aperture extent.

Table 4. Relative Error on \mathbf{b} for test scenes.

Scene #	2.5 Degree	5 Degree	10 Degree
1	0.0099	0.0072	0.0085
2	0.1137	0.0129	0.0084
3	0.5513	0.0086	0.0086

4.4 Antenna Conclusions

A high crosstalk microstrip antenna was designed in Ansys HFSS. The designed crosstalk was ≈ 5 dB at boresight and resonant frequency, putting the modeled antenna well within the robustness region determined in Chapter II. The model antenna also displayed good coupling characteristics in the S-parameters. The high crosstalk antenna was then constructed and tested in the AFRL/RYMF ATEMS lab. The physical antenna showed good agreement with the model, but higher crosstalk than was designed for. The physical antenna has a port 1 crosstalk level of -1.4404 dB and a port 2 crosstalk of -2.3603 dB, much higher than the -5.2 dB of designed crosstalk. These values would be outside the robustness region of -9 dB to -3 dB if taken as zero-phase. However, the physical antenna was slightly asymmetric and had complex crosstalk. These two factors contributed to successful recoveries of several fixed synthetic point target scenes. By assuming that port 1 on the physical antenna was the horizontal port and assuming port 2 was the vertical port, the measured boresight co- and cross-pol gain values could be used to construct a transmit matrix and thus a crosstalk matrix for the dropped-channel PolSAR model. Using the measured crosstalk matrix, the model was able to recover almost all fixed scenes over three different psfs. The successful modeling, construction, and measurement of the high crosstalk antenna along with the successful recovery of synthetic point target scenes using the physical antenna's measure gain values lends further credibility to feasibility of a dropped channel PolSAR system.

The successful design and measurement campaign of the antenna moves us closer

to a system design. However, other forms of compression are available. Currently, the compression is in the polarimetric and spatial domain via the dropped channel mechanic and the spatial dictionary representation of \mathbf{x} . Some literature points to the ability to compressively sense in the range and crossrange dimensions. Specifically, fast and slow-time sub-Nyquist sampling has been theorized for SAR systems. By combining fast-time and slow-time compression, along with polarimetric and spatial compression, a very high level of compressed sensing could be achieved, which would be invaluable for systems that cannot be recovered and thus need to transmit data to an operator elsewhere. In the next chapter, the integration of fast and slow time sub-Nyquist sampling to the dropped channel PolSAR model is explored.

V. Sub-Nyquist Sampling for Drop-Channel PolSAR Model

Determining a region of acceptable crosstalk values and demonstrating a proof-of-concept antenna give further validity to the drop channel PolSAR model. However, there are other dimensions in a PolSAR system that can benefit from CS techniques. Individually, each dimension has had CS techniques performed successfully on it; however, the author is unaware of any work that combines multiple dimensions into the same CS model. In this chapter, a model is developed that allows compressed sensing across fast-time, slow-time, and polarimetric channels simultaneously. By performing CS across all three of these dimensions together, a greater overall level of compression is achieved.

Previous attempts at dropping samples came in the form of bandwidth limitation [64]. While in a similar vein to the QuadCS method used in this chapter, the number of samples in [64] was not changed, only the bandwidth was limited. A corresponding oversampling was then used to aid in recovery. While the limit and oversample method was successful, as seen in Figure 70, the solution is not as elegant as QuadCS. Additionally, performing oversampling can be expensive at the hardware level while bandpass filtering and low-rate sampling is more affordable. More details on the reduced bandwidth and oversampling method can be found in [64].

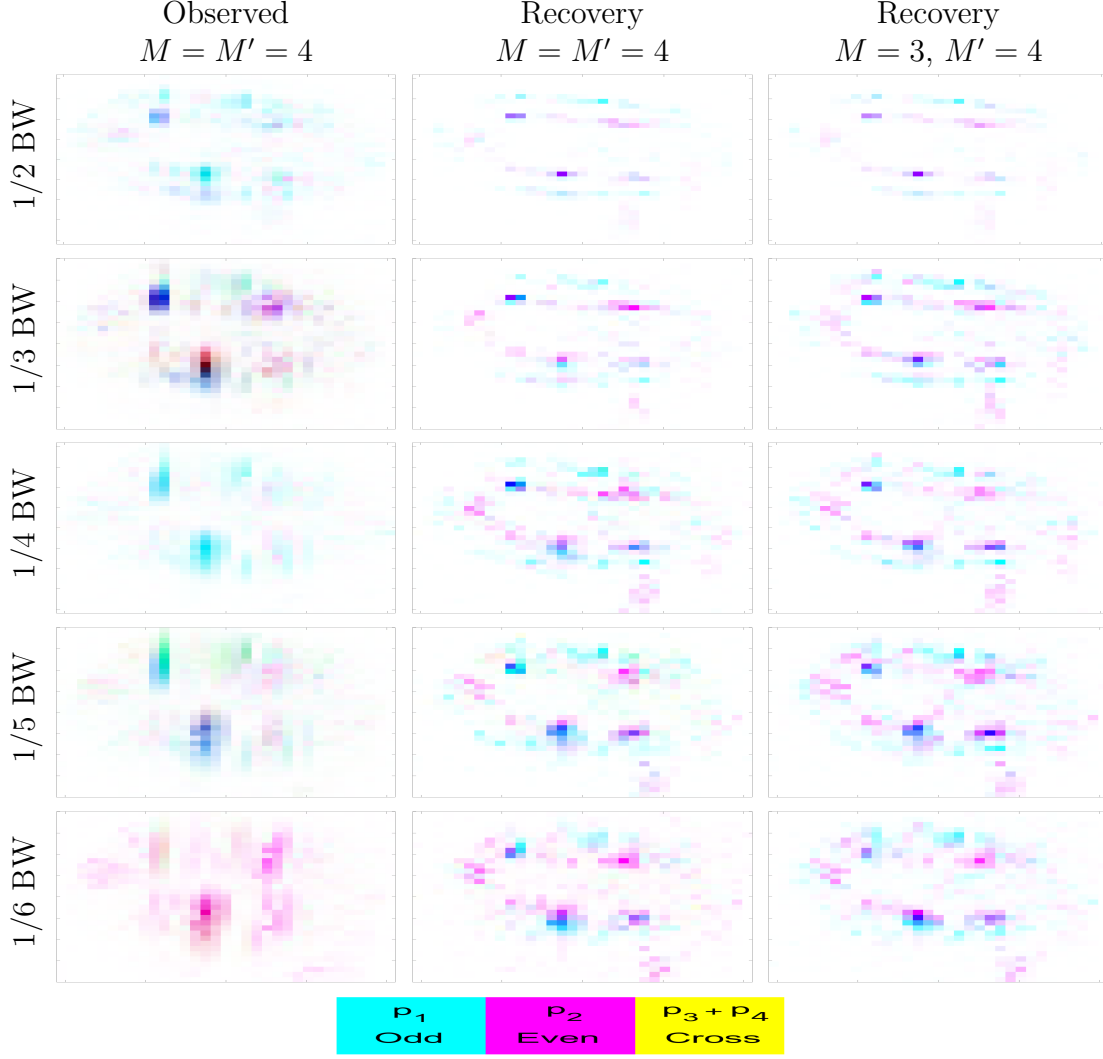


Figure 70. GOTCHA CMY results as a function of bandwidth.

5.1 Integration of Sub-Nyquist SAR with Drop-Channel PolSAR Model

The integration of fast-time and slow-time undersampling takes place in two stages. First, a single channel spotlight SAR model with sub-Nyquist sampling is described and tested. Second, the undersampled spotlight SAR model is extended to full-polarimetric model and combined with the drop channel PolSAR model. The full, sub-Nyquist dropped channel PolSAR model is tested first with no channel dropped. Finally, the highly compressed PolSAR model will be tested over a few combinations

of undersample rates and channel drops to begin to determine the limits of compression within the model based on the ability of BPDN to recover.

5.1.1 Single-channel Spotlight-mode SAR sub-Nyquist Model.

In the dropped channel PolSAR model, the psf was used to describe the measurement system [5–8, 63, 64]. In order to compare compression rates with sample rates, as well as to perform operations in the receiver chain, the psf convolution can no longer be used to approximate the system. Instead, a waveform matching dictionary is used which allows for the simulation of fast-time and slow-time samples. In the single channel case, two different models are being combined. The fast-time undersampling is inspired by the model in [59, 66], while the slow-time undersampling comes from the model in [17, 18, 62].

As described in Section 2.2, the fast-time undersampling model from [66] can take either a vector of the discretized reflectivity scene or the sampled phase histories as an input. The relation between the vector and phase history is

$$\mathbf{y}_{\phi_i} = \mathbf{D}_{\phi_i} \mathbf{x}_m \quad (47)$$

where \mathbf{x}_m is the $N_r N_s \times 1$ complex vector of scene reflectivities for a single channel, N_r is the number of Nyquist-rate fast-time samples, N_s is the number fully sampled slow-time samples, \mathbf{D}_{ϕ_i} is the $N_r \times N_r N_s$ waveform matching dictionary for the ϕ_i -th slow-time sample, and $\mathbf{y}_{\phi_i} \in \mathbb{C}^{N_r \times 1}$ is the ϕ_i -th fast-time sampled phase history vector in the spatial frequency domain [66]. Much like in [108], the full phase history is built

as

$$\mathbf{y} = \mathbf{D}\mathbf{x}_m + \boldsymbol{\eta} \quad (48)$$

$$\begin{bmatrix} \mathbf{y}_{\phi_1} \\ \vdots \\ \mathbf{y}_{\phi_{N_s}} \end{bmatrix} = \begin{bmatrix} \mathbf{D}_{\phi_1} \\ \vdots \\ \mathbf{D}_{\phi_{N_s}} \end{bmatrix} \mathbf{x}_m + \boldsymbol{\eta} \quad (49)$$

where $\boldsymbol{\eta} \in \mathbb{C}^{N_r N_s \times 1}$ is the measurement noise.

The elements of the ϕ_i -th waveform matching dictionary can be described as

$$\mathbf{D}_{\phi_i}^{n,q} = \exp\{-j2\pi f_n/c\Delta R_q\} \quad (50)$$

where f_n is the n th discrete frequency of a set spanning the bandwidth with $n = 1, \dots, N_r$, and ΔR_q is the differential range to the q th position in the discretized scene with $q = 1, \dots, N_r N_s$, defined as

$$\begin{aligned} \Delta R_q &= x_q(\cos(\phi_t)\cos(\theta_t) + \cos(\phi_r)\cos(\theta_r)) \\ &\quad + y_q(\sin(\phi_t)\cos(\theta_t) + \sin(\phi_r)\cos(\theta_r)), \end{aligned} \quad (51)$$

where (x_q, y_q) are the coordinates of the q th position in the discretized scene, ϕ_t, ϕ_r are vectors of azimuth (ϕ) positions of the transmitter and receiver and θ_t, θ_r are vectors of the elevation (θ) positions of the transmitter and receiver. In words, the elements of \mathbf{D} describe all possible target phase histories for the fast time pulse at the given slow time position. Notably, the elements of \mathbf{D} as defined in (50) assumes that the targets are isotropic point scatterers. Modification to \mathbf{D} would be required for extended scatterers. Also note that (51) assumes all scatterers are at $z = 0$. The 2D assumption was done for simplicity and computational memory concerns. For the monostatic case, $t = r$ and (51) reduces to the two-way differential range.

The formulation of (51) allows for extension to a bistatic case in the future, but a monostatic assumption is made in the simulations later in this chapter.

The fast-time undersampling from [59, 66] is then implemented. The fast-time undersampled measurement model can now be written as

$$\tilde{\mathbf{y}} = \text{diag}(\mathbf{R}_1 \hat{\mathbf{P}}_{c1}, \dots, \mathbf{R}_{N_s} \hat{\mathbf{P}}_{cN_s}) \mathbf{D} \mathbf{x}_m + \boldsymbol{\eta} \quad (52)$$

where $\hat{\mathbf{P}}_{ci} \in \mathbb{C}^{N_r \times N_r}$ performs convolution with frequency-domain chipping sequence coefficients and $\mathbf{R}_i \in \mathbb{C}^{M_r \times N_r}$ describes the operation of the bandpass filter and low-rate sampling [59]. Recall that matrices $\hat{\mathbf{P}}_c$ and \mathbf{R}_i are described in more detail in Chapter 2.2. As in [60], the chipping sequence for each slow-time measurement is assumed to be independent to increase the randomness of the final measurement and thus spread the information across the spectrum. The output of (52) is $\tilde{\mathbf{y}} \in \mathbb{C}^{M_r N_s \times 1}$ the vector of fast-time undersampled phase history. Figure 71 shows a toy example of the effects of fast-time undersampling as a visual aid. Note that in addition to the bandwidth being reduced, the sample spacing has changed as well. In [59, 60], the QuadCS model still performs Nyquist rate sampling, but in reference to the reduced bandwidth.

The fast-time samples are taken at each slow-time pulse. In [17, 18, 62], slow-time undersampling is accomplished through the use of a restriction operator. The slow-time undersampling operator is included in the model as

$$\tilde{\mathbf{y}} = \mathbf{R}_S \text{diag}(\mathbf{R}_1 \hat{\mathbf{P}}_{c1}, \dots, \mathbf{R}_{N_s} \hat{\mathbf{P}}_{cN_s}) \mathbf{D} \mathbf{x}_m + \boldsymbol{\eta} \quad (53)$$

where $\mathbf{R}_S \in \mathbb{R}^{M_r M_s \times M_r N_s}$ is a restriction operator that selects $M_s < N_s$ random slow-time samples to be measured. That is, the PRF does not change but a randomly flipped switch will prevent a certain number of pulses from being either received or

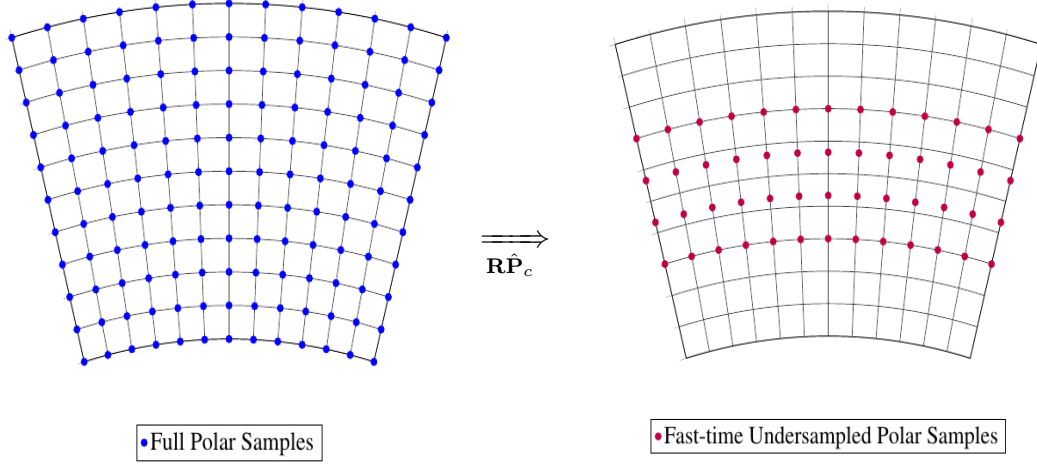


Figure 71. Example of fast-time undersampling

transmitted [62]. The restriction operator matrix can be thought of as a $M_r N_s \times M_r N_s$ identity matrix that has random blocks of N_r rows removed to simulate the non-measurement of those slow-time pulses. The final output is $\mathbf{y}^{cs} \in \mathbb{C}^{M_r M_s \times 1}$ the vector of fast-time and slow-time undersampled phase history. Figure 72 shows a toy example to illustrate the result of slow-time undersampling after fast-time undersampling. With fast-time and slow-time undersampling successfully implemented, the model is extended to the fully polarimetric case.

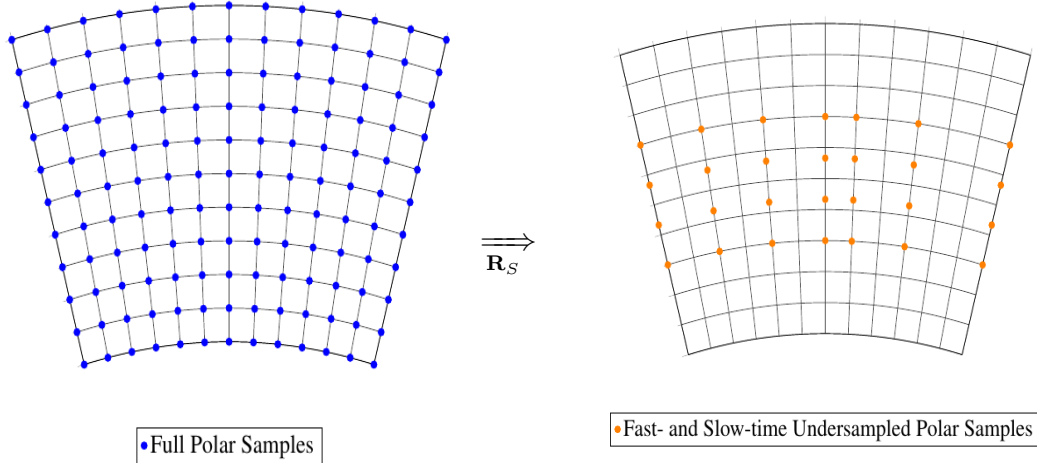


Figure 72. Example of slow-time undersampling

5.1.2 Highly compressed PolSAR Model.

Extending the single-channel model to be combined with the dropped channel PolSAR model is fairly straightforward. First, let the steps in (53) replace the single channel measurement matrix \mathbf{A}_1 in (24). Then, note that (24) can be written as

$$\mathbf{y} = \tilde{\mathbf{A}}_P(\mathbf{J}\mathbf{C} \otimes \mathbf{I}_N)(\mathbf{x} + \mathbf{w}) \quad (54)$$

where \mathbf{w} is the random clutter vector and

$$\tilde{\mathbf{A}}_P = \begin{bmatrix} \mathbf{A}_1 & \mathbf{0} & \mathbf{0} & \dots \\ \mathbf{0} & \mathbf{A}_2 & \mathbf{0} & \vdots \\ \mathbf{0} & \mathbf{0} & \ddots & \mathbf{0} \\ \mathbf{0} & \mathbf{0} & \dots & \mathbf{A}_{N_p} \end{bmatrix} \quad (55)$$

as described in [7]. Also note that the sub-matrices of $\tilde{\mathbf{A}}_P$ are not required to be identical however, they are assumed to be for this research effort. Now let $\mathbf{A}_1 = \mathbf{R}_S \text{diag}(\mathbf{R}_1 \hat{\mathbf{P}}_{c1}, \dots, \mathbf{R}_{M_s} \hat{\mathbf{P}}_{cM_s}) \mathbf{D}$ be the new channel measurement matrix. It is also assumed that the polarimetric pulse interleaving is fast enough to not cause changes in \mathbf{D} due to platform position shift or changes to the slow-time restriction operator between channels.

The highly compressed PolSAR model can then be written as

$$\mathbf{y}^{hc} = \tilde{\mathbf{A}}_P(\mathbf{J}\mathbf{C} \otimes \mathbf{I}_N)(\mathbf{x} + \mathbf{w}) \quad (56)$$

$$= (\mathbf{J}\mathbf{C} \otimes \mathbf{A}_1)(\mathbf{x} + \mathbf{w}) \quad (57)$$

$$= (\mathbf{J}\mathbf{C} \otimes \mathbf{R}_S \text{diag}(\mathbf{R}_1 \hat{\mathbf{P}}_{c1}, \dots, \mathbf{R}_{N_s} \hat{\mathbf{P}}_{cN_s}) \mathbf{D})(\mathbf{x} + \mathbf{w}). \quad (58)$$

The output is the highly compressed vector $\mathbf{y}^{hc} \in \mathbb{C}^{M_c M_s M_r \times 1}$ of measured, under-

sampled, channel dropped, phase histories. The model in (56) can then be solved via BPDN. While similar to the model in [7], note that the output vector \mathbf{y}^{hc} is not a vectorized image, but rather vectorized sampled phase histories in the spatial frequency domain. Since the measured vector is in the spatial frequency domain, an imaging algorithm will still be required to “view” the measurement vector.

5.2 Sub-Nyquist Drop-Channel PolSAR CS Results

When combining multiple, complex models together, care needs to be taken to ensure that each piece is working as intended and that all the pieces are working together as expected. To validate the highly compressed PolSAR model, a single channel case is examined first. In the single channel case, fast-time and slow-time undersampling are examined both individually and then as combined on a known scene. When extending to the fully polarimetric model, the drop channel compression is examined separately, and then together with the fast-time and slow-time compression to show the full model. Finally, two examples from the GOTCHA data set are examined to show the model’s performance on realistic scenes. For the verification scenes, no noise or clutter is added to the signal. Since no noise is added to the point target scenes, $\epsilon = 0$ and the BPDN problem reduces to the basis pursuit problem. In the single channel case, the BP problem can be written as

$$\min_{\mathbf{x}_m} \|\mathbf{x}_m\|_1 \quad \text{subject to } \mathbf{R}_S \text{diag}(\mathbf{R}_1 \hat{\mathbf{P}}_{c1}, \dots, \mathbf{R}_{N_s} \hat{\mathbf{P}}_{cN_s}) \mathbf{D} \mathbf{x}_m = \tilde{\mathbf{y}}. \quad (59)$$

As in Chapter 3, a pseudo-truth vector is made for the GOTCHA subscenes. That pseudo-truth vector is then put through the model in (56) to generate results. While no clutter is added to these pseudo-truth vectors, some clutter may have spilled through from the original GOTCHA data when forming the vectors. As such, the

full-pol GOTCHA-like scenes will use the BPDN problem given as

$$\min_{\mathbf{x}} \|\mathbf{x}\|_1 \quad \text{subject to } \|\mathbf{y}^{hc} - (\mathbf{JC} \otimes \mathbf{R}_S \text{diag}(\mathbf{R}_1 \hat{\mathbf{P}}_{c1}, \dots, \mathbf{R}_{N_s} \hat{\mathbf{P}}_{cN_s}) \mathbf{D}) \mathbf{x}\|_2 \leq \epsilon, \quad (60)$$

where $\epsilon = 1.2763 \times 10^{-6}$. The value of ϵ was estimated by forming a pseudo-truth vector of an area with no targets using the same parameters as used to make the pseudo-truth vectors of the test scenes.

5.2.1 Single-Channel Case.

The reference scene to used to validate the model can be scene in Figure 73. The scene is inspired by the 19 target scene from [28] and some of his example system parameters are used. Specifically, the scene is a ring of point targets 10 meters in diameter with a target every 45 degrees and one more target in the center. The radar system parameters are the same as those listed on [28, pg 174], recreated here in Table 5 for clarity. With a wavelength of $\lambda = 0.03$ m and an aperture extent of $\Delta\phi = 2.34^\circ$, the range and cross-range resolution are both calculated as 0.3743 m [28].

Table 5. SAR system parameters from [28, pg 174]

Parameter	Value	Symbol
Initial Squint Angle	-1.17°	ϕ_{s_i}
Final Squint Angle	$+1.17^\circ$	ϕ_{s_f}
Center Frequency	1.0×10^{10} Hz	f_0
Bandwidth	4.015×10^8 Hz	B
Slant-plane scene diameter	37.5 m	D
Number of fast-time samples	100	N_r
Number of slow-time samples	100	N_s

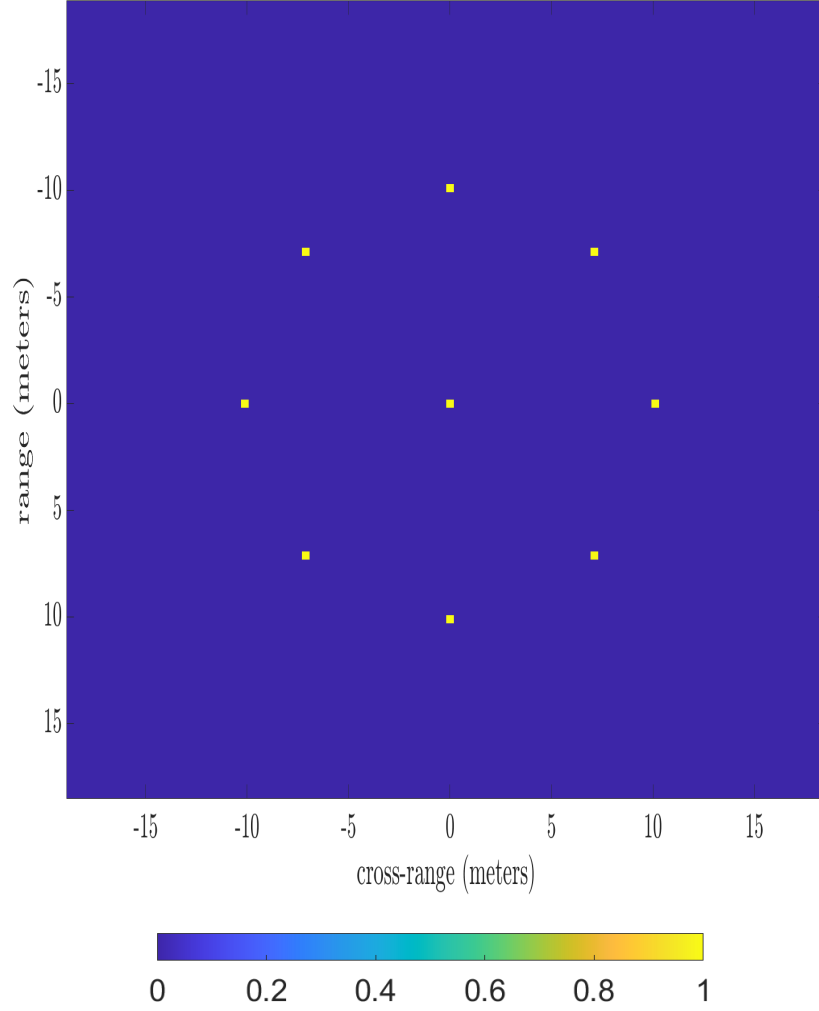


Figure 73. Truth image of the point target test scene.

To first validate the model in (53), the recovery is run with no undersampling ($\mathbf{R}_S = \mathbf{I}$, $\mathbf{R} = \mathbf{I}$ and no chipping sequence $\hat{\mathbf{P}}_c = \mathbf{I}$). The middle column of Figure 74 shows the PFA image of the output $\tilde{\mathbf{y}}$ and the right column shows the BP recovery. The relative recovery error in \mathbf{x} , defined as

$$E = \frac{\|\mathbf{x}_{true} - \hat{\mathbf{x}}\|_2^2}{\|\mathbf{x}_{true}\|_2^2}, \quad (61)$$

was very low at 9.8948×10^{-5} , as expected. The purpose of the baseline test is to

verify that \mathbf{D} is behaving as expected. Figure 74 shows the expected target spreading in the observed image due to the band-limited nature of the fast-time and slow-time samples. Since the bandwidth (B) and aperture extent ($\Delta\phi$) are finite, a spreading is observed in both the range and cross range dimensions respectively. The recovered image in Figure 74 does not exhibit the spreading effects because BP is simultaneously deconvolving the spread while finding a sparse solution $\hat{\mathbf{x}}$ to the BP problem.

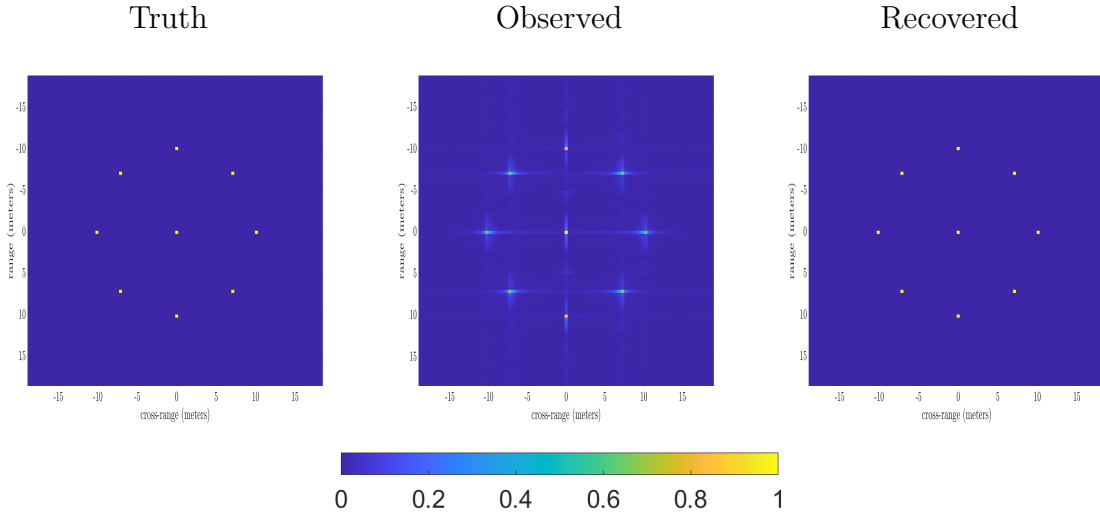


Figure 74. PFA observed and BP recovered images of the scene with no undersampling and no chipping sequence, compared with truth

Slow-time compression is then performed via a restriction operator [18, 62]. To isolate the analysis to only the effects of the slow-time undersampling, fast-time sampling is omitted by setting $\mathbf{R} = \mathbf{I}$ and “turning off” the chipping sequence via $\hat{\mathbf{P}}_c = \mathbf{I}$. To perform slow-time undersampling functionally, a list of M_s random indices out of N_s possible indices is created without replacement. These random indices are then used to reduce blocks of N_r rows from $\mathbf{R}_S = \mathbf{I}$ to get the restriction operator $\mathbf{R}_S \in \mathbb{R}^{N_r M_s \times N_r N_s}$.

For the first test, a 50% slow-time undersampling is used, meaning only half of the fully sampled data is measured. The observed PFA image of the undersampled

phase history can be seen in Figure 75. By reducing the number of slow-time samples acquired, the maximum un-aliased cross range limit has been reduced from 37.5 m to 18.75 m. Then, by attempting to plot on the same size as the fully sampled scene, aliasing effects become visible in cross range. The aliasing effects show in the middle column of Figure 75 as the cross range blurring of the point targets. Note that; while the undersampling does not need to be explicitly random, there is a benefit to doing so. A uniform undersampling, such as picking every other slow-time sample, produces strong aliasing effects due to periodicity. By selecting random slow-time samples for undersampling, the periodicity is broken and the strong aliasing artifacts appear more random noise-like [18].

The right column of Figure 75 shows the BP recovered, 50% slow-time under-sampled scene. The scene is recovered with an error in \mathbf{x} of 4.6430×10^{-5} , which is on par with the baseline. The scene is extremely sparse, so a perfect recovery is expected from the model [18]. While a scene this sparse can be recovered equally as well from uniform undersampling, a less sparse scene (such as a GOTCHA subscene) would suffer significantly more from the strong aliasing effects of non-random undersampling. In testing, the use of random undersampling produced approximately half the ℓ_2 error as uniform undersampling for the same GOTCHA-inspired scene.

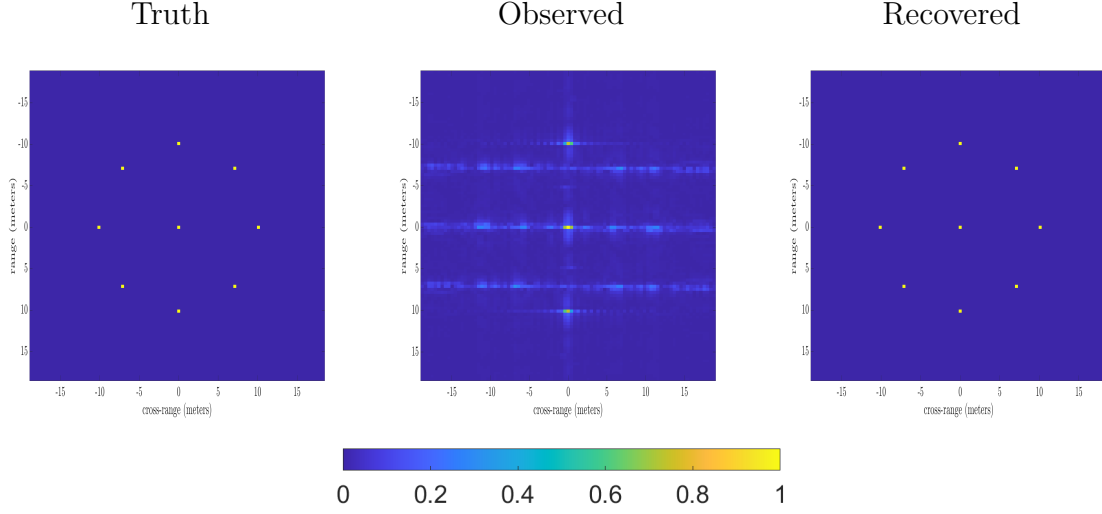


Figure 75. PFA observed and BP recovered images of the scene with 50% slow-time undersampling, compared with truth

With slow-time undersampling verified, fast-time undersampling is now examined. First, no undersampling is performed and the chipping sequence is included to verify that the original scene can still be recovered in the randomness. The middle column of Figure 76 shows the PFA image of the chipped scene. As seen in Chapter 2.2, the chipping sequence spreads the information across the spectrum. Thus, PFA images of undersampled scenes will be uninformative with the chipping sequence included, so PFA images prior to recovery will no longer be shown. The right column of Figure 76 shows the BP recovered scene. Since the chipping sequence is a known random noise, and no undersampling is performed, Figure 76 shows the expected result of an excellent recovery. The recovery error on \mathbf{x}_m for the fully-sampled, chipped scene was 3.6076×10^{-6} .

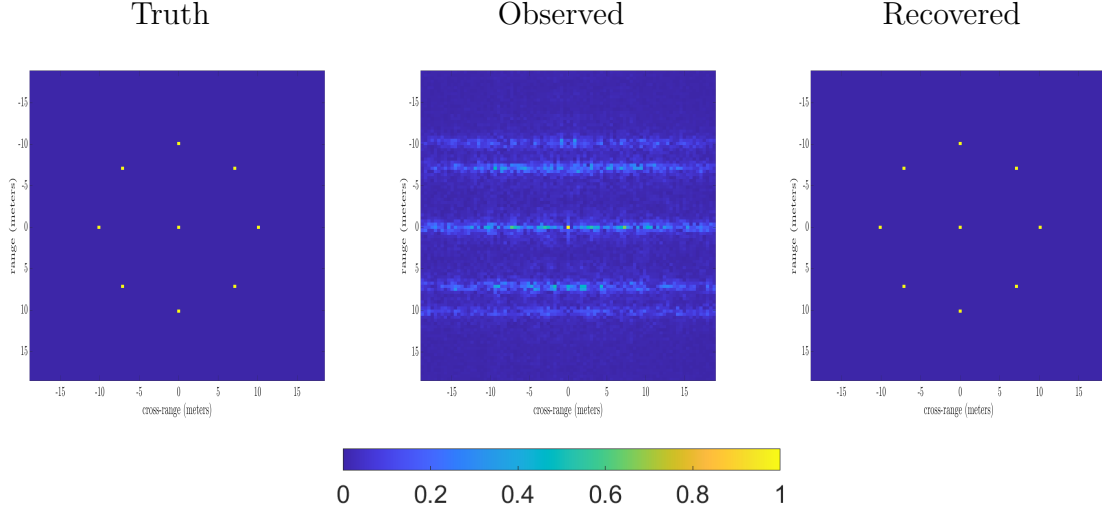


Figure 76. PFA observed and BP recovered images of the scene with chipping sequence and no undersampling, compared with truth

With the chipping sequence recovery verified, fast-time undersampling is tested without slow-time undersampling. As in the slow-time case, a 50% fast-time undersampling rate is used. Figure 77 shows the BP recovered scene. The targets are clearly recovered, and the recovery error on \mathbf{x}_m is 2.1522×10^{-5} . Again, the scene is very sparse, so perfect recovery was expected. Now that the individual undersampling schemes have been verified, they are combined to do fast-time and slow-time undersampling and recovery.

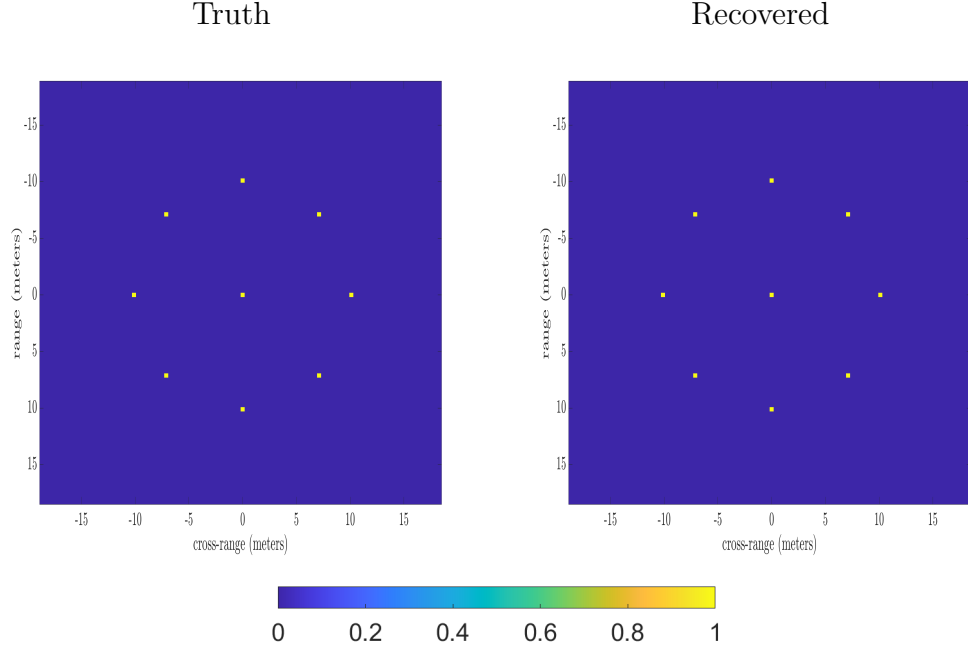


Figure 77. BP recovered scene with 50% fast-time undersampling, compared with truth

Finally, both fast-time and slow-time undersampling are combined and tested. Specifically, a 50% fast-time and 50% slow-time undersampling rate are used. The total amount of data reduction is now at 25% of the fully sampled data measured. Figure 78 shows the BP recovered scene. Again, given the sparsity of the scene, the recovery is excellent with a recovery error of 1.3175×10^{-4} . Given the sparsity of the scene, the model in (53) is able to recovery the scene accurately using only 25% of the fully sampled data! With fast-time and slow-time undersampling both verified, the model can be extended to the fully polarimetric case.

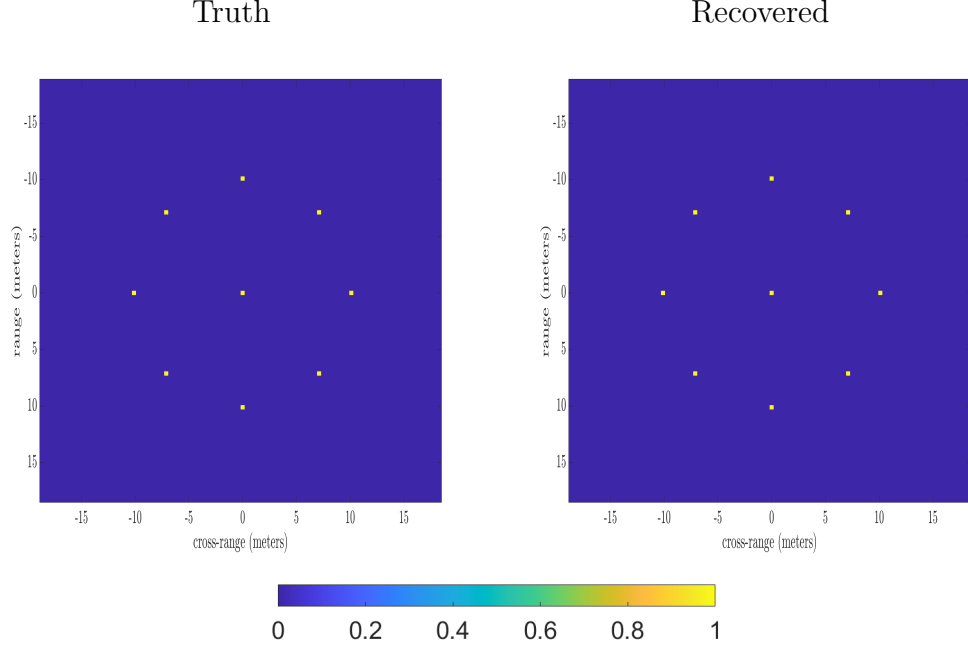


Figure 78. BP recovered scene with 50% fast-time and slow-time undersampling, compared with truth

5.2.2 Fully-Polarimetric Case.

Extending the single channel undersampling model to include all four polarization channels requires the input \mathbf{x}_m to be extended to \mathbf{x} in length to $N = N_p N_s N_r$ where N_p is the total possible number of polarization channels, N_s is the number of full-rate slow-time samples and N_r is the number of full-rate fast-time samples. To extend the input scene reflectivity data, each target in the reference scene is given a polarization response. The two targets at 10 m due East and West are set to an odd bounce response corresponding to the first column in the Pauli basis. The four targets at Northeast, Northwest, Southeast, and Southwest are given a cross-pol response corresponding to the third column of the Pauli basis. The two targets 10 m due North and South, as well as the center target, are given an even bounce corresponding with the second column of the Pauli basis. The vectorized scene reflectivities for each channel are then stacked on top of each other to form the required $N \times 1$ vector length.

Figure 79 shows the truth CMY images of the full-pol scene.

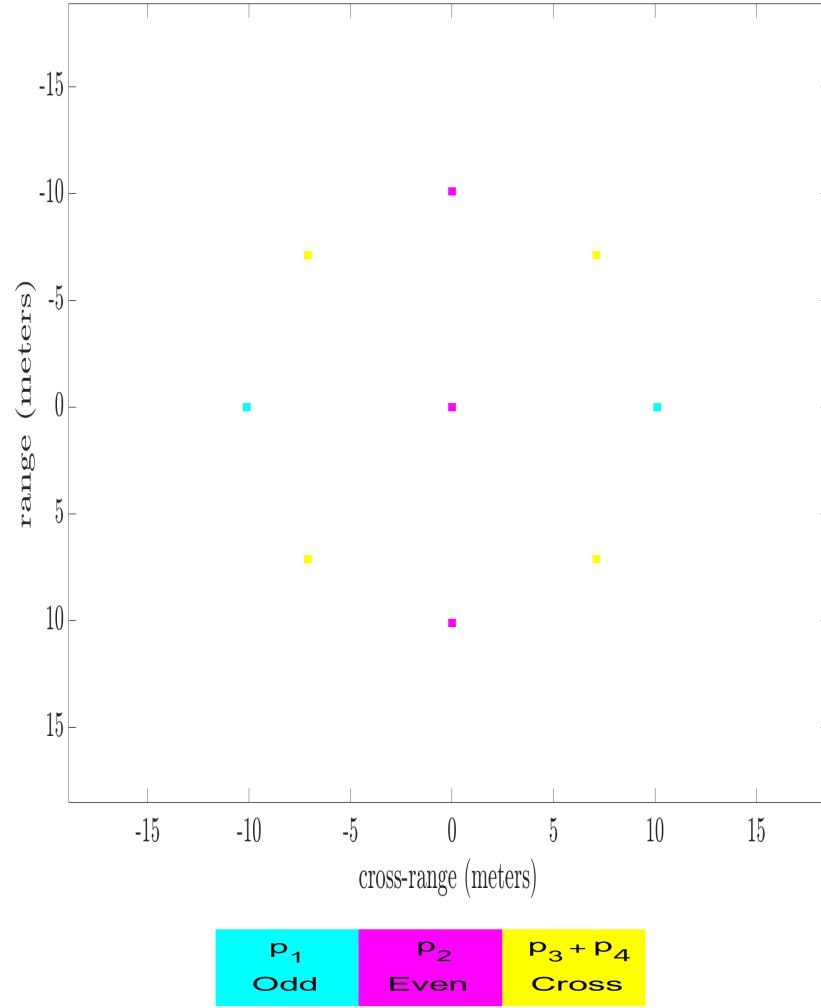


Figure 79. Truth CMY image of full-pol point target test scene.

The first test is a situation with no undersampling and no channel drop. The

chipping sequence and crosstalk are both included, using the crosstalk matrix

$$\mathbf{C} = \begin{bmatrix} 0.78 & -0.6201 + 0.0695i \\ 0.6802 + 0.2030i & 0.7098 \end{bmatrix} \otimes \begin{bmatrix} 0.93 & -0.0220 - 0.3713i \\ -0.0220 - 0.3713i & 0.93 \end{bmatrix} \quad (62)$$

from [7] and previously stated as (40). Figure 80 shows the BP recovered scene. The scene is recovered perfectly as expected, with a recovery error of 1.9877×10^{-5} . With the baseline verified, the undersampling can start to be incorporated. To discuss the remaining scenes, a compression ratio is defined. Let $M = M_p M_s M_r$ be the number of samples in the undersampled scene where M_p is the number of measure polarization channels, M_s is the number of measured slow-time samples, and M_r is the number of measured fast-time samples. The compression ratio can then be defined as $\frac{M}{N}$ and is used as a performance metric.

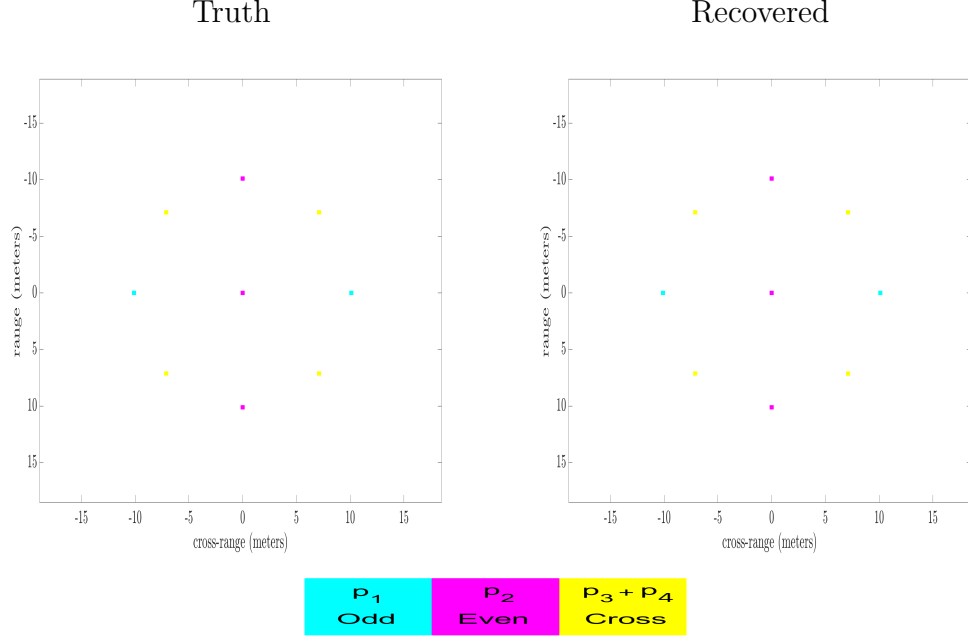


Figure 80. BP recovered scene with no undersampling and no channel drop compared with truth

Next, $M_r = 0.5N_r$ fast-time undersampling is included. As in the single channel example, 50% of the original fast-time data is measured. Figure 81 shows the BPDN recovered results. With a compression ratio of 0.5, the scene is recovered fully with a recovery error in \mathbf{x} of 2.0940×10^{-6} . A $M_s = 0.5N_s$ slow-time undersampling is then combined with the fast-time undersampling. Figure 82 shows the results. With a compression ratio of 0.25, the targets are still fully recovered and the recovery error is 2.3702×10^{-6} . Finally, the HH channel is dropped and the full model is tested. Figure 83 shows the results. With a compression ratio of 0.1875, the model shows no issues in recovery. The recovery error for the scene where only 18.75% of the full-sampled data are measured, is still a very low 1.4426×10^{-5} . Table 6 shows the relative error on \mathbf{x} for each of the point target scenes. With the full, highly compressed PolSAR model verified, the model can be demonstrated on sub-scenes of the GOTCHA data set to gauge performance on realistic scenes.

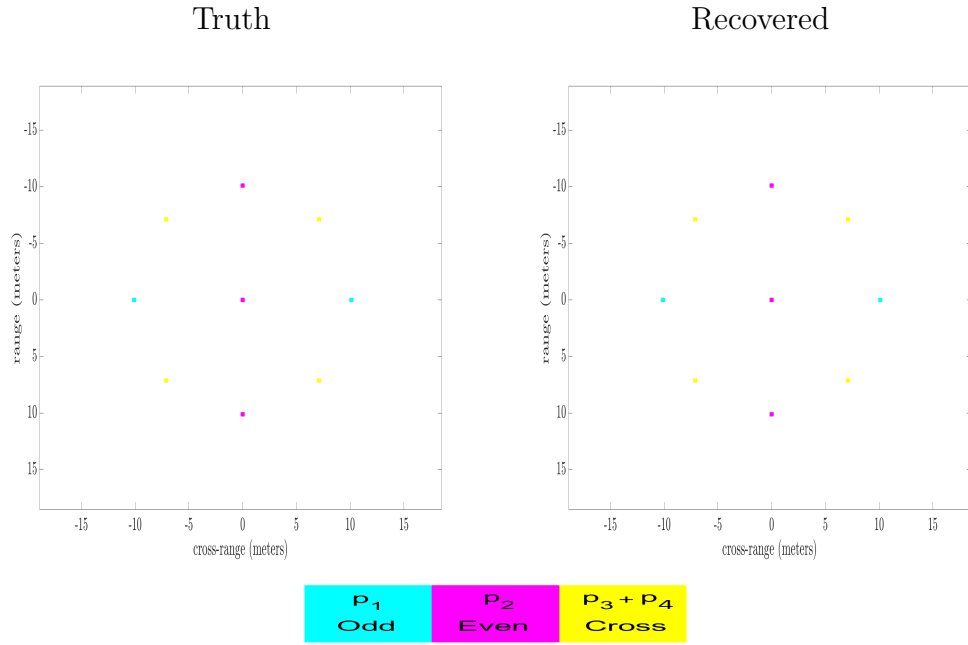


Figure 81. BP recovered scene, 50% fast-time undersampling, no channel drop

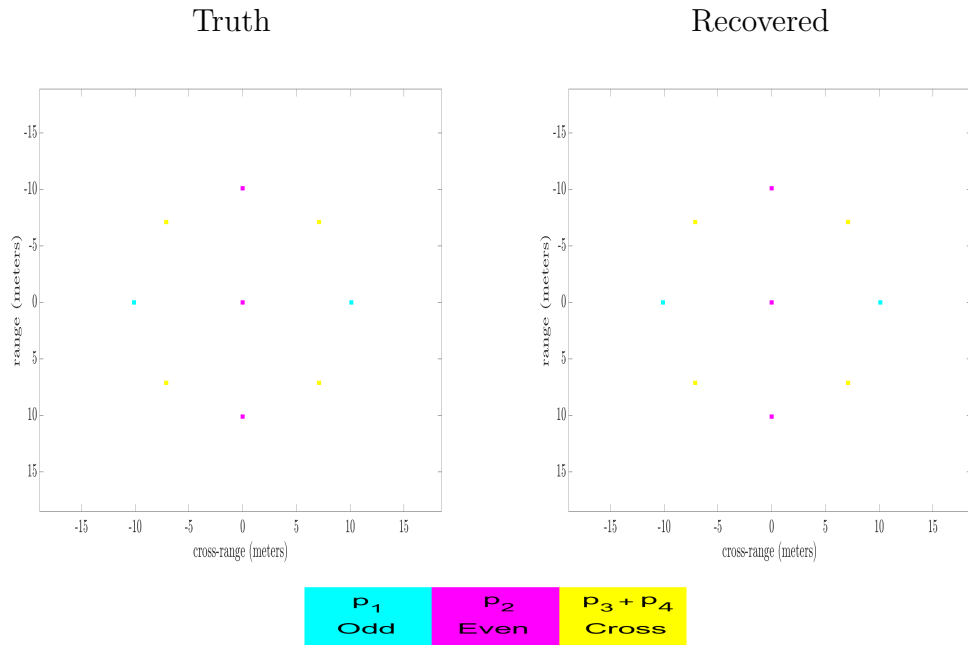


Figure 82. BP recovered scene, 50% fast- and slow-time undersampling, no channel drop

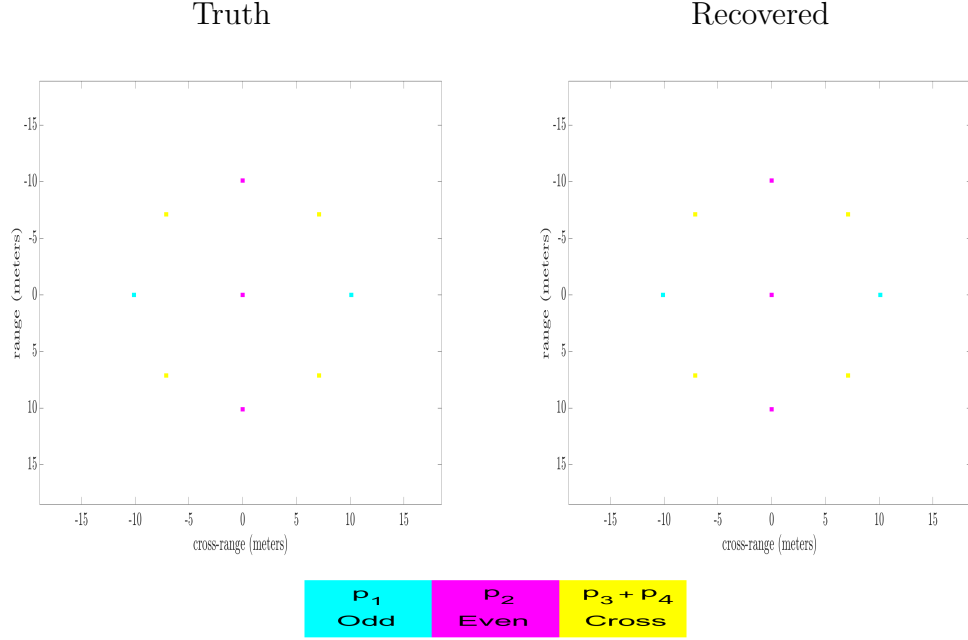


Figure 83. BP recovered scene, 50% fast- and slow-time undersampling, HH dropped

Table 6. Relative Error on \mathbf{x} for point target scenes.

	Undersampling	Compression	Rel Err on \mathbf{x}
Singe Pol	$M_r = N_r, M_s = N_s, \mathbf{P}_c = \mathbf{I}$	0%	9.8948×10^{-5}
	$M_r = N_r, M_s = 0.5N_s, \mathbf{P}_c = \mathbf{I}$	50%	4.6430×10^{-5}
	$M_r = N_r, M_s = N_s, \mathbf{P}_c = \mathbf{P}_c$	0%	3.6076×10^{-6}
	$M_r = 0.5N_r, M_s = N_s$	50%	2.1522×10^{-5}
	$M_r = 0.5N_r, M_s = 0.5N_s$	75%	1.3175×10^{-4}
Full Pol	$M_r = N_r, M_s = N_s, M_p = N_p$	0%	1.9877×10^{-5}
	$M_r = 0.5N_r, M_s = N_s, M_p = N_p$	50%	2.0940×10^{-6}
	$M_r = 0.5N_r, M_s = 0.5N_s, M_p = N_p$	75%	2.3702×10^{-6}
	$M_r = 0.5N_r, M_s = 0.5N_s, M_p = 0.75N_p$	81.25%	1.4426×10^{-5}

5.2.3 GOTCHA Examples.

Two scenes are now observed, inspired by sub-scenes from the GOTCHA data set [29]. These scenes are used to demonstrate the highly compressed PolSAR model's performance on more realistic looking data. The first scene is taken from a segment of the calibration target scene in the upper left corner. Figure 84 shows the reference

CMY image for the calibration scene. The second is taken from a segment of the parking lot. Figure 85 shows the reference CMY image of the parking lot portion used. For all GOTCHA scenes, the crosstalk matrix in (40) is used as it showed the best performance in Chapter III. Also, as in Chapter III, pseudo-truth vectors are made from the GOTCHA sub-scenes to ease the integration of the model as well as to provide a consistent performance metric.

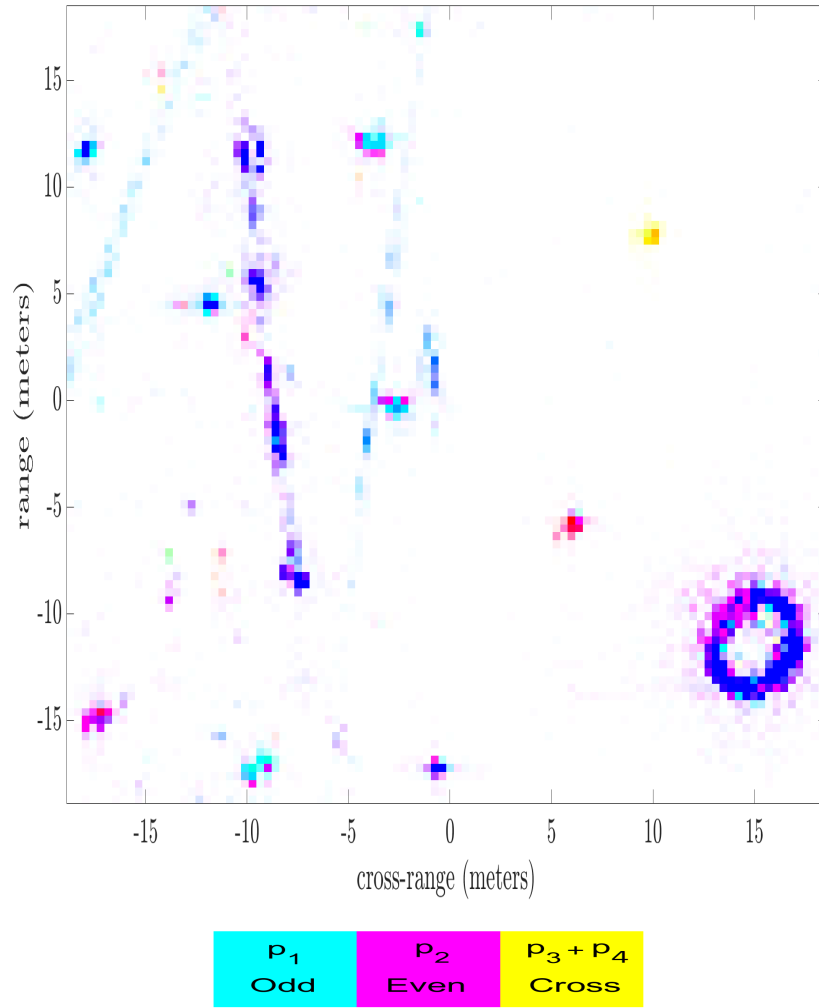


Figure 84. Reference CMY image of calibration target sub-scene

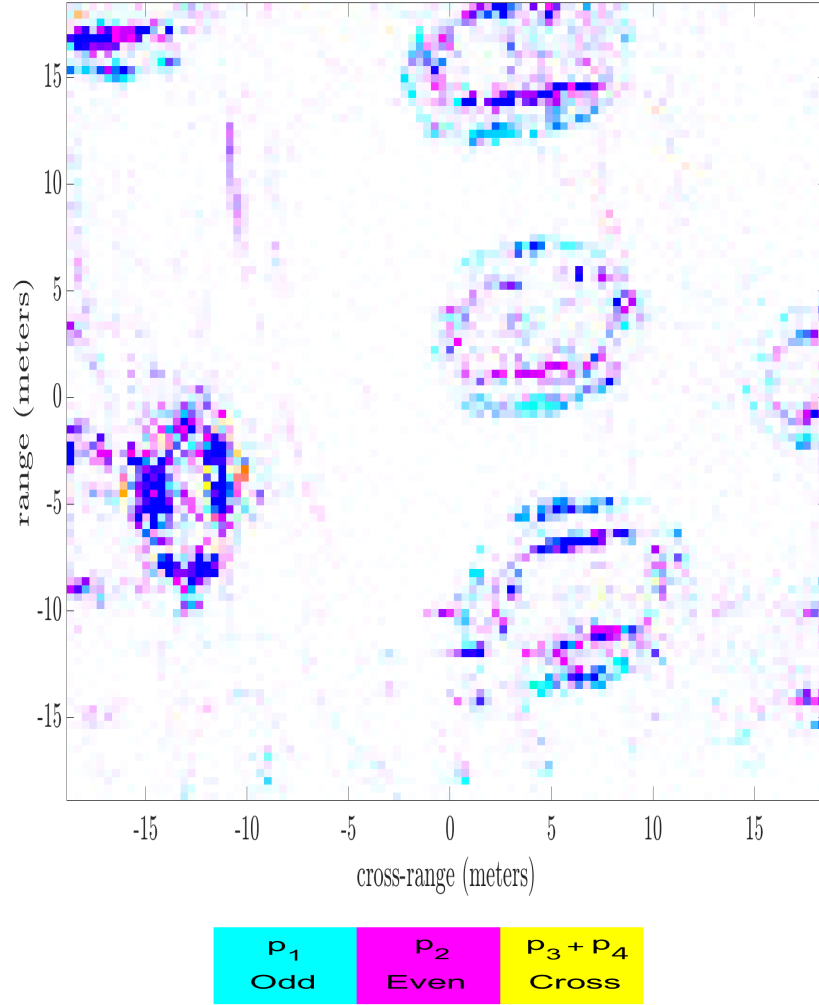


Figure 85. Reference CMY image of parking lot sub-scene

The GOTCHA sub-scenes are noticeably less sparse than the point target scene used to validate the model. As such, lower amounts of undersampling will be applied. To get a baseline, each scene is run through the model without any undersampling or channel drops. The relative recovery error in \mathbf{x} for the calibration scene is 0.2298 and for the parking lot the recovery error is 0.3998. The recovery error for the calibration scene is very similar to what was achieved with this scene and crosstalk matrix in Chapter 3.

The fast-time and slow-time undersample rates are now set to 10%, meaning 90% of the fully sampled data is used, and the polarization “undersample rate” is now effectively $M_p = 0.75N_p$. The compression ratio is now 0.6075, meaning 60.75% of the fully sampled data is used in total. Figures 86 and 87 show the recovered results for the calibration scene and parking lot respectively. The recovery error for the calibration scene is 0.3629, and the recovery error for the parking lot is 0.5320. Comparing Figure 86 to Figure 84, the target positions and sizes appear similar, but some obvious polarimetric errors are visible. Similarly, comparing Figures 85 and 87 show noticeable differences in the recovered undersampled scene.

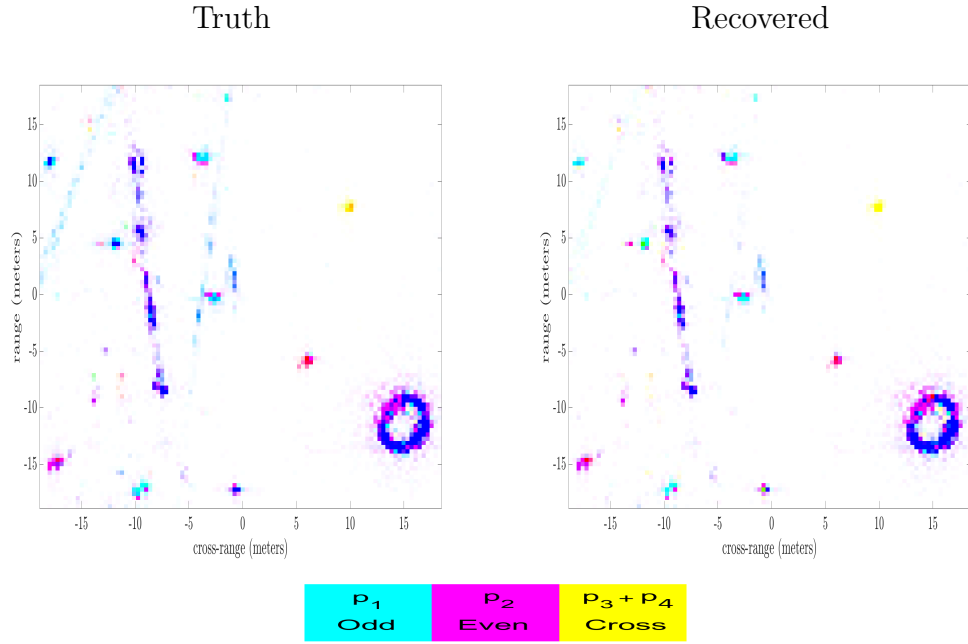


Figure 86. CMY image of recovered calibration target sub-scene, $M_r = 0.9N_r$, $M_s = 0.9N_s$, HH Dropped ($M_p = 0.75N_p$)

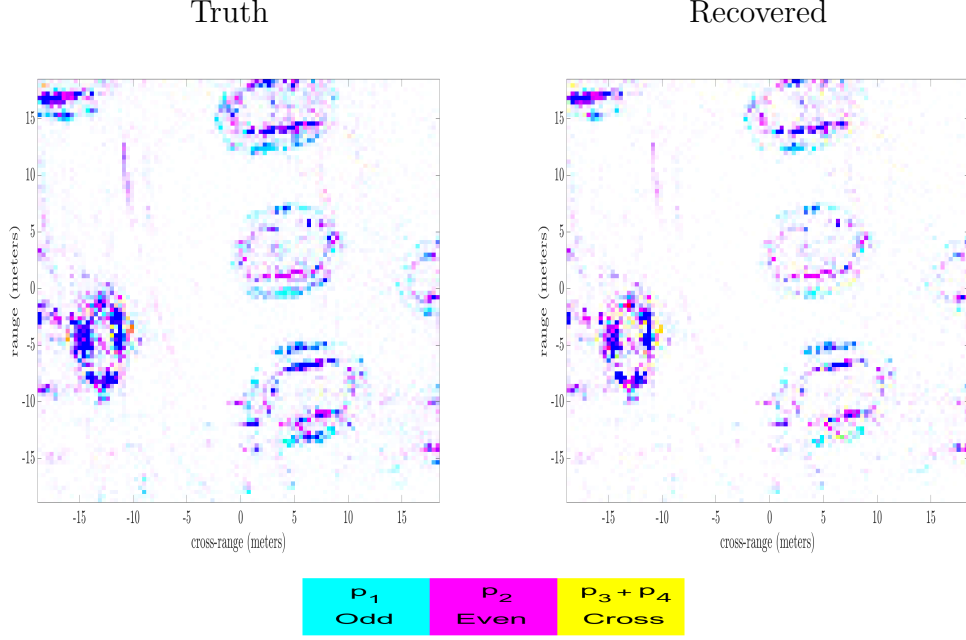


Figure 87. CMY image of recovered parking lot sub-scene, $M_r = 0.9N_r$, $M_s = 0.9N_s$, **HH **Dropped** ($M_p = 0.75N_p$)**

There are two factors working against the recovery of the GOTCHA-like scenes. First, these scenes are significantly less sparse as mentioned in Chapter 3. For every CS model, there is a direct relationship between scene sparsity and recovery performance. The approximate target density of the calibration scene in Figure 84 is 18.31% and the parking lot in Figure 85 has a target density of 17.43%, both much higher than Chapter 3 showed the model capable of going. Second and related, the compression factors in the undersampling model are multiplicative. Since there is a string of fast-time samples at every slow-time sample and a set of fast-time and slow-time samples for each channel, any amount of undersampling in any domain is multiplied through, giving much great compression. The ability to achieve great compression by applying CS technique to each domain is the goal of the model in (56), but it is also a double-edged blade. In situations with lower sparsity, the increased compression becomes an issue instead of a benefit. However, there are a few possible avenues to

combat higher target density scenes in future work. By solving for the coefficients vector $\mathbf{b} = (\mathbf{P} \otimes \mathbf{S})\mathbf{x}$, the sparsity may increased enough for the model. Additionally, an extend spatial dictionary could be used for \mathbf{S} like in [63] to further increase the sparsity of the scene representation. There are many different matrices available to tune for recovery performance and a different analysis could likely provide a more successful combination.

5.3 Sub-Nyquist Drop-Channel PolSAR System Diagram

A proposed block diagram of a highly compressed SAR receiver is shown in Figure 88. For a modern system, the transmit and receive antennas are likely to be a dual-pol phased array. Channel selection must happen after the signal has been measured and coupled by the antenna in order for the crosstalk information to propagate through the system and allow for recovery of a dropped channel. The slow-time restriction operator can be co-located with the ADC to prevent random PRIs from being sampled. The QuadCS scheme handles the fast-time undersampling prior to data storage. Once aperture extent has been completed, the measured data can then be transmitted or transferred to a station that will perform the sparse recovery and produce the estimated scene reflectivity image. While the system diagram in Figure 88 is very basic, it can be thought of as an extension to [7, Fig 1], and another step closer to bridging the gap between a model and a system design.

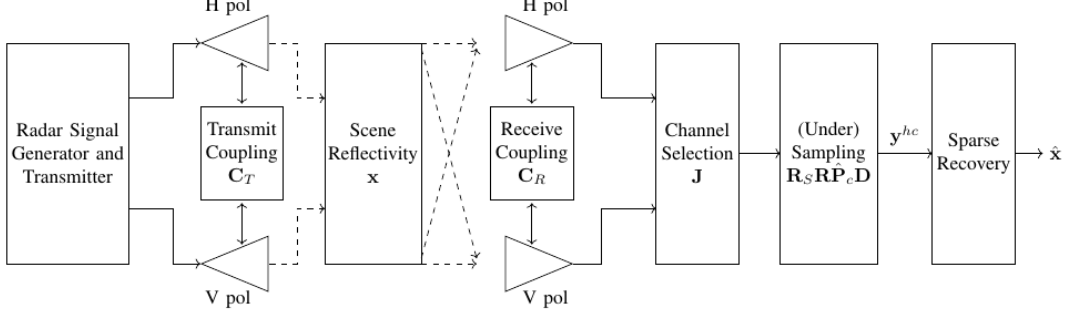


Figure 88. Block Diagram for Sub-Nyquist Drop Channel PolSAR System

5.4 Sub-Nyquist Drop-Channel PolSAR CS Conclusions

The highly compressed PolSAR model is able to combine compressed sensing in multiple dimensions to reduce the overall amount of measured data. In the single channel case, combining fast-time and slow-time undersampling was able to reduce the measured data to 18.75% of the normally required amount while still recovering the point target scene. By including dropped channel polarimetric sub-scenes of the GOTCHA data set, the model's performance is evaluated on a more realistic scene. Recovery error was much higher on the GOTCHA-like sub-scenes. The higher target density of the scenes, along with the multiplicative compression of the model, made for less accurate recoveries. However, the recovery error of each GOTCHA-like scene was only approximately 0.14 above baseline while only using 60.75% of the fully sampled data! It is possible that different combinations of undersampling amounts or a different crosstalk matrix may be able to further reduce the required data.

The amount of possible reduction will also have a dependence on scene sparsity levels. A future study will examine different combinations of undersampling amounts along with their effects over scene sparsity. By developing a model for highly compressed PolSAR, another step is taken towards being able to design a compressed PolSAR system. While data storage rates and quantities have become increasingly inexpensive, there are still applications where being able to measure a fraction of the

data to get all of the information are beneficial. Spaceborne platforms and attritable systems both depend on transmission of the data to provide the information instead of storage and delivery. In these use cases, being able to transmit less data to a base station that can then do the recovery and image formation could mean getting the data quicker, or at all.

VI. Conclusions

With the addition of polarimetry to SAR, more information about the scene is collected, which requires proportionally more data storage, processing, and transmission requirements. To help alleviate the data volume requirements in PolSAR systems, CS techniques have been leveraged. **The goal of this research was to define required crosstalk levels for dropped-channel PolSAR CS, use the desired crosstalk design point to define and simulate a prototype antenna for a dropped-channel PolSAR CS system, and further increase the compression by integrating fast and slow-time CS methods to the dropped-channel PolSAR model.**

In Chapter III, a region of crosstalk values capable of providing successful recovery in the drop channel PolSAR model was determined. These values were tested on both synthetic point target scenes as well as a portion of the GOTCHA scene. The determination of such a robustness region both informs and alleviates some of the challenges of an antenna design. Seeing that the required crosstalk region was above what usual radar antennas are designed for, a novel antenna design was determined to be necessary.

In Chapter IV, a high crosstalk antenna was design, built, and tested. A patch antenna was chosen for cost, weight, and manufacturability. The design was performed in ANSYS/HFSS targeting and achieving the middle point of the robustness region. The antenna was then manufactured and tested. The manufactured antenna displayed a higher level of crosstalk than designed for, but still an acceptable amount. To confirm that the designed antenna meets requirements, the measured crosstalk values were used to recover a dropped channel in a synthetic scene accurately.

Chapter V details the design, validation, and some performance of a highly compressed PolSAR system. The highly compressed PolSAR system integrates a fast-

time undersampling technique and a slow-time undersampling technique into the drop channel PolSAR model. By including other dimensions to compress over, the overall measured data requirements were lowered. The highly compressed PolSAR model performance was demonstrated on both a synthetic point target scene as well as two sub-scene of the GOTCHA data set. In both cases, significantly more compression was able to be achieved than in the drop channel PolSAR model alone while still providing good recovery performance. The definition and demonstration of the highly compressed PolSAR model moves the bar further for compressed sensing of PolSAR data and moves the research one step closer to system design.

6.1 Research Contributions

In this dissertation, the following research contributions were demonstrated:

1. Chapter III determined a range of crosstalk levels from -9 dB to -3 dB that provides low ℓ_2 recovery error for a range of measurement matrices.
 - (a) Chapter III also displayed the extension of the drop channel PolSAR model to include a spatial dictionary.
 - (b) Chapter III also demonstrated the ability of the drop channel PolSAR model to perform super resolution.
2. Chapter IV showed the design, simulation, and measurement of an antenna capable of providing the desired crosstalk parameters for a compressed PolSAR system.
3. Chapter V demonstrated the incorporation of fast and slow-time undersampling to dropped-channel PolSAR model and a unifying algorithm to combine polarimetric compression with fast- and slow-time compression to generate highly compressed PolSAR data.

6.2 Future Work

Several future studies are recommended by the author. In terms of system robustness, there are other dimensions worth considering. For now, it is assumed that the crosstalk matrix is known exactly. Such knowledge is rarely, if ever, available. Thus, a future study should look at how robust the system is to differences between the true crosstalk matrix and the recovery crosstalk matrix. Additionally, it was shown that allowing for different crosstalk amounts on transmit and receiver allowed for less sparse scenes to be recovered more accurately than when transmit and receive were assumed to have the same crosstalk components. A future study might look at repeating the Monte Carlo robustness study over varying differences between the transmit and receiver crosstalk amounts to determine another, perhaps wider, robustness region.

The high crosstalk antenna design was a valuable proof of concept. However, real modern radar antenna systems are typically arrays of antennas. A useful next step would be to design and measure a high crosstalk antenna array to see if better crosstalk performance can be achieved. Additionally, antenna crosstalk is dependent on look angle. The author assumed a boresight-only view for simplicity in this research effort. Moving forward, the angular dependence of crosstalk should be examined and accounted for in the recovery, which will make the model more friendly to techniques such as electronic beam steering.

Highly compressed PolSAR as defined here is in its infancy. Perhaps the most useful future study would be a determination of how different combinations of different levels of fast-time and slow-time compression affect recovery performance. Ideally, scene sparsity would be taken into account as well. Another good follow on would be a comparison between different fast-time undersampling (i.e., Xampling) and slow-time undersampling (i.e., jitter slow-time) techniques to see if different combinations

of undersampling techniques can provide better compression ratios. Nevertheless, the research presented in this dissertation pushed the drop channel PolSAR CS model further towards a physical realization and significantly increases the amount of compression possible through the inclusion of CS techniques in other dimensions of the PolSAR data.

Bibliography

1. J. J. van Zyl, *Synthetic Aperture Radar Polarimetry*, 1st ed. Hoboken, NJ: Wiley, Nov. 2011.
2. F. Ulaby and C. Elachi, Eds., *Radar Polarimetry for Geoscience Applications*. Norwood, MA: Artech House, 1990.
3. S. Cloude, *Polarisation: Applications in Remote Sensing*. New York: Oxford University Press, 2010.
4. S. Foucart and H. Rauhut, *A Mathematical Introduction to Compressive Sensing*, 1st ed., ser. Applied and Numerical Harmonic Analysis. Birkhäuser Basel, 2013.
5. J. A. Jackson and F. Lee-Elkin, “Channel crosstalk model for fully-polarimetric SAR compressive sensing,” *IEEE Radar Conf.*, pp. 1–6, May 2017.
6. —, “Polarimetric SAR Compressive Sensing Examples,” *IEEE Radar Conf.*, pp. 0736–0741, Apr. 2018.
7. —, “Exploiting Channel Crosstalk for Polarimetric SAR Compressive Sensing,” *IEEE Transactions on Aerospace and Electronic Systems*, vol. 56, no. 1, pp. 475–485, Feb. 2020.
8. J. A. Jackson and F. A. Lee-Elkin, “System, Method, and Apparatus for Recovering Polarization Radar Data,” United States of America Patent US11 194 104B1, Dec., 2021.
9. O. Bar-Ilan and Y. C. Elda, “Compressed radar via Doppler focusing,” in *2014 IEEE Radar Conference*, May 2014, pp. 0181–0184.

10. O. Bar-Ilan and Y. C. Eldar, "Sub-Nyquist Radar," in *SCC 2013; 9th International ITG Conference on Systems, Communication and Coding*, Jan. 2013, pp. 1–6.
11. E. Baransky, G. Itzhak, N. Wagner, I. Shmuel, E. Shoshan, and Y. Eldar, "Sub-Nyquist radar prototype: Hardware and algorithm," *IEEE Transactions on Aerospace and Electronic Systems*, vol. 50, no. 2, pp. 809–822, Apr. 2014.
12. K. Aberman and Y. C. Eldar, "Sub-Nyquist SAR via Fourier Domain Range-Doppler Processing," *IEEE Transactions on Geoscience and Remote Sensing*, vol. 55, no. 11, pp. 6228–6244, Nov. 2017.
13. Y. C. Eldar and G. Kutyniok, Eds., *Compressed Sensing: Theory and Applications*, 1st ed. Cambridge; New York: Cambridge University Press, Jun. 2012.
14. Y. C. Eldar, *Sampling Theory: Beyond Bandlimited Systems*. Cambridge, United Kingdom: Cambridge University Press, 2015.
15. Q. Liang, "Compressive sensing for synthetic aperture radar in fast-time and slow-time domains," in *2011 Conference Record of the Forty Fifth Asilomar Conference on Signals, Systems and Computers (ASILOMAR)*, Nov. 2011, pp. 1479–1483.
16. J. Sun and J. Yu, "Compressed synthetic aperture radar with structurally sparse random matrices," in *2017 IEEE Radar Conference*, May 2017, pp. 1344–1347.
17. V. M. Patel, G. R. Easley, D. M. Healy, and R. Chellappa, "Compressed sensing for Synthetic Aperture Radar imaging," in *2009 16th IEEE International Conference on Image Processing (ICIP)*, Nov. 2009, pp. 2141–2144.

18. V. M. Patel, G. R. Easley, D. M. H. Jr, and R. Chellappa, "Compressed Synthetic Aperture Radar," *IEEE Journal of Selected Topics in Signal Processing*, vol. 4, no. 2, pp. 244–254, Apr. 2010.
19. C. A. Wiley, "Synthetic Aperture Radars," *IEEE Transactions on Aerospace and Electronic Systems*, vol. 21, no. 3, pp. 440–443, May 1985.
20. M. A. Richards, *Fundamentals of Radar Signal Processing*. McGraw-Hill, 2014.
21. W. G. Carrara, R. M. Majewski, and R. S. Goodman, *Spotlight Synthetic Aperture Radar: Signal Processing Algorithms*. Boston: Artech Print on Demand, Jul. 1995.
22. W. L. Melvin and J. A. Scheer, Eds., *Principles of Modern Radar: Advanced techniques*. Raleigh, NC: Scitech Publishing, Oct. 2012.
23. D. Munson, "An introduction to strip-mapping synthetic aperture radar," in *ICASSP '87. IEEE International Conference on Acoustics, Speech, and Signal Processing*, vol. 12, Apr. 1987, pp. 2245–2248.
24. D. C. Munson and R. L. Visentin, "A signal processing view of strip-mapping synthetic aperture radar," *IEEE Transactions on Acoustics, Speech, and Signal Processing*, vol. 37, no. 12, pp. 2131–2147, Dec. 1989.
25. F. Li, C. Croft, and D. N. Held, "Comparison of Several Techniques to Obtain Multiple-Look SAR Imagery," *IEEE Transactions on Geoscience and Remote Sensing*, vol. 21, no. 3, pp. 370–375, Jul. 1983.
26. R. K. Moore, J. P. Claassen, and Y. H. Lin, "Scanning Spaceborne Synthetic Aperture Radar with Integrated Radiometer," *IEEE Transactions on Aerospace and Electronic Systems*, vol. AES-17, no. 3, pp. 410–421, May 1981.

27. R. Bamler and M. Eineder, "ScanSAR processing using standard high precision SAR algorithms," *IEEE Transactions on Geoscience and Remote Sensing*, vol. 34, no. 1, pp. 212–218, Jan. 1996.
28. C. V. Jakowatz, Jr., D. E. Wahl, P. H. Eichel, D. C. Ghiglia, and P. A. Thompson, *Spotlight-Mode Synthetic Aperture Radar: A Signal Processing Approach*. New York, NY: Springer Science+Buisness Media, 1996.
29. C. H. Casteel Jr., L. A. Gorham, M. J. Minardi, S. M. Scarborough, K. D. Naidu, and U. K. Majumder, "A challenge problem for 2D/3D imaging of targets from a volumetric data set in an urban environment," in *Proc. of SPIE*, E. G. Zelnio and F. D. Garber, Eds., Orlando, Florida, USA, Apr. 2007, p. 65680D.
30. M. Desai and W. Jenkins, "Convolution backprojection image reconstruction for spotlight mode synthetic aperture radar," *IEEE Transactions on Image Processing*, vol. 1, no. 4, pp. 505–517, Oct. 1992.
31. M. Jin, F. Cheng, and M. Chen, "Chirp scaling algorithms for SAR processing," in *Proceedings of IGARSS '93 - IEEE International Geoscience and Remote Sensing Symposium*, Aug. 1993, pp. 1169–1172 vol.3.
32. J. Sun, J. Wang, Y. Yuan, and S. Mao, "Extended Chirp Scaling Algorithm for Spotlight SAR," *Chinese Journal of Aeronautics*, vol. 15, no. 2, pp. 103–108, May 2002. [Online]. Available: <https://www.sciencedirect.com/science/article/pii/S1000936111601386>
33. C. Cafforio, C. Prati, and F. Rocca, "SAR data focusing using seismic migration techniques," *IEEE Transactions on Aerospace and Electronic Systems*, vol. 27, no. 2, pp. 194–207, Mar. 1991.

34. H. Huachao, J. Xin, C. Yingying, and W. Wei, "Omega-k algorithm for bistatic spotlight SAR imaging," in *2009 2nd Asian-Pacific Conference on Synthetic Aperture Radar*, Oct. 2009, pp. 330–333.
35. H.-S. Shin and J.-T. Lim, "Omega-K Algorithm for Spaceborne Spotlight SAR Imaging," *IEEE Geoscience and Remote Sensing Letters*, vol. 9, no. 3, pp. 343–347, May 2012.
36. Y. Gao, D. Liang, T. Fang, Z.-X. Zhou, H. Zhang, and R. Wang, "A Modified Extended Wavenumber-Domain Algorithm for Ultra-High Resolution Spaceborne Spotlight SAR Data Processing," in *IGARSS 2020 - 2020 IEEE International Geoscience and Remote Sensing Symposium*, Sep. 2020, pp. 1544–1547, iSSN: 2153-7003.
37. R. Hu, B. S. M. R. Rao, M. Alae-Kerahroodi, and B. Ottersten, "Orthorectified Polar Format Algorithm for Generalized Spotlight SAR Imaging With DEM," *IEEE Transactions on Geoscience and Remote Sensing*, vol. 59, no. 5, pp. 3999–4007, May 2021.
38. J. Chen, Y. Wang, Q. Jin, and X. Mao, "Modified Polar Format Algorithm for Spotlight SAR with High Squint and Dive Angle," in *2021 IEEE 6th International Conference on Signal and Image Processing (ICSIP)*, Oct. 2021, pp. 629–634.
39. Z. Wei, Y. Wang, and L. Zhuang, "Polar Format Algorithm Based Azimuth-Range Decouple for Sparse SAR Imaging," in *EUSAR 2021; 13th European Conference on Synthetic Aperture Radar*, Mar. 2021, pp. 1–4.

40. H. Lin, J. Chen, M. Xing, X. Chen, D. You, and G. Sun, “2-D Frequency Autofocus for Squint Spotlight SAR Imaging With Extended Omega-K,” *IEEE Transactions on Geoscience and Remote Sensing*, vol. 60, pp. 1–12, 2022.
41. X. Mao, T. Shi, R. Zhan, Y.-D. Zhang, and D. Zhu, “Structure-Aided 2-D Autofocus for Airborne Bistatic Synthetic Aperture Radar,” *IEEE Transactions on Geoscience and Remote Sensing*, vol. 59, no. 9, pp. 7500–7516, Sep. 2021.
42. F. Tataranni, A. Gallipoli, and P. Inversi, “Focusing of new generation SAR Spotlight data through the Efficient Time-Domain Back-Projection,” in *EUSAR 2021; 13th European Conference on Synthetic Aperture Radar*, Mar. 2021, pp. 1–6.
43. Z. Chen, Y. Zhou, J. Qiu, W. Wang, Z. Zhang, and R. Wang, “A Novel Approach to Further Enhancing SNR in Digital Beamforming SAR Utilizing Hybrid Strip-Map/Spotlight Mode,” *IEEE Geoscience and Remote Sensing Letters*, vol. 19, pp. 1–5, 2022.
44. T. Kraus, J. P. T. Ribeiro, M. Bachmann, U. Steinbrecher, and C. Grigorov, “Concurrent Imaging for TerraSAR-X: Wide-Area Imaging paired with High-Resolution Capabilities,” *IEEE Transactions on Geoscience and Remote Sensing*, pp. 1–1, 2022.
45. J. Wu, D. Feng, J. Wang, and X. Huang, “SAR Imaging from Missing Raw Data via Sparsity Adaptive StOMP,” in *2021 IEEE 6th International Conference on Signal and Image Processing (ICSIP)*, Oct. 2021, pp. 371–375.
46. D. Zou and J. Lang, “Sparse Reconstruction Using Improved SL0 Algorithm by Tabu Search and Application to Spotlight SAR Imaging,” in *2021 IEEE 3rd*

Eurasia Conference on IOT, Communication and Engineering (ECICE), Oct. 2021, pp. 376–380.

47. Z. Suo, Y. Guo, and Z. Liao, “Analysis of Polarization Orientation Angle Estimation of X-Band Polsar Data and Experiment Investigation,” in *IGARSS 2020 - 2020 IEEE International Geoscience and Remote Sensing Symposium*, Sep. 2020, pp. 704–707, iSSN: 2153-7003.
48. M. Busquier, J. M. Lopez-Sanchez, and D. Bargiel, “Added Value of Coherent Copolar Polarimetry at X-Band for Crop-Type Mapping,” *IEEE Geoscience and Remote Sensing Letters*, vol. 17, no. 5, pp. 819–823, May 2020.
49. J. R. Huynen, “Phenomenological theory of radar targets,” Ph.D. Dissertation, Technical University, Delft, The Netherlands, 1970. [Online]. Available: <https://repository.tudelft.nl/islandora/object/uuid%3Ae4a140a0-c175-45a7-ad41-29b28361b426>
50. S. Cloude and E. Pottier, “A review of target decomposition theorems in radar polarimetry,” *IEEE Transactions on Geoscience and Remote Sensing*, vol. 34, no. 2, pp. 498–518, Mar. 1996.
51. C. A. Balanis, *Advanced Engineering Electromagnetics*, 2nd ed. John Wiley & Sons, 2012.
52. I. Hajnsek and Y.-L. Desnos, Eds., *Polarimetric Synthetic Aperture Radar: Principles and Application*. Springer Nature, 2021, accepted: 2021-04-20T12:47:49Z. [Online]. Available: <https://library.oapen.org/handle/20.500.12657/48227>

53. K. Aberman and Y. C. Eldar, "Range-Doppler processing via fourier coefficients: The path to a sub-Nyquist SAR," in *2016 IEEE Radar Conference (RadarConf)*, May 2016, pp. 1–5.
54. M. Mishali and Y. C. Eldar, "Sub-Nyquist Sampling: Bridging Theory and Practice," *arXiv:1106.4514 [cs, math]*, Jun. 2011, arXiv: 1106.4514. [Online]. Available: <http://arxiv.org/abs/1106.4514>
55. —, "From Theory to Practice: Sub-Nyquist Sampling of Sparse Wideband Analog Signals," *IEEE Journal of Selected Topics in Signal Processing*, vol. 4, no. 2, pp. 375–391, Apr. 2010, arXiv: 0902.4291. [Online]. Available: <http://arxiv.org/abs/0902.4291>
56. —, "Xampling: Analog Data Compression," in *2010 Data Compression Conference*, Mar. 2010, pp. 366–375.
57. M. Mishali, Y. C. Eldar, and A. J. Elron, "Xampling: Signal Acquisition and Processing in Union of Subspaces," *IEEE Transactions on Signal Processing*, vol. 59, no. 10, pp. 4719–4734, Oct. 2011.
58. M. Mishali, Y. C. Eldar, O. Dounaevsky, and E. Shoshan, "Xampling: Analog to digital at sub-Nyquist rates," *IET Circuits, Devices Systems*, vol. 5, no. 1, pp. 8–20, Jan. 2011.
59. F. Xi, S. Chen, and Z. Liu, "Quadrature Compressive Sampling for Radar Signals," *IEEE Transactions on Signal Processing*, vol. 62, no. 11, pp. 2787–2802, Jun. 2014.
60. H. Yang, C. Chen, S. Chen, and F. Xi, "Sub-Nyquist SAR via Quadrature Compressive Sampling with Independent Measurements," *Remote*

- Sensing*, vol. 11, no. 4, p. 472, Jan. 2019. [Online]. Available: <https://www.mdpi.com/2072-4292/11/4/472>
61. J. A. Tropp, J. N. Laska, M. F. Duarte, J. K. Romberg, and R. G. Baraniuk, "Beyond Nyquist: Efficient Sampling of Sparse Bandlimited Signals," *IEEE Transactions on Information Theory*, vol. 56, no. 1, pp. 520–544, Jan. 2010.
 62. X. V. Yang, V. M. Patel, and A. P. Petropulu, "Spaceborne SAR antenna size reduction enabled by compressive sampling," in *2016 IEEE Global Conference on Signal and Information Processing (GlobalSIP)*, Dec. 2016, pp. 297–301.
 63. J. Becker and J. A. Jackson, "Expansion of Dropped-Channel PolSAR CS to include a Spatial Dictionary," in *5th International Workshop on Compressed Sensing applied to Radar, Multimodal Sensing, and Imaging (CoSeRa)*, Sep. 2018, pp. 1–5.
 64. ———, "Super-Resolution Using Dropped-Channel PolSAR Compressive Sensing," in *IEEE Radar Conference 2019*, Apr. 2019, pp. 1–6.
 65. F. Xi, S. Chen, and Z. Liu, "Quadrature compressive sampling for radar signals: Output noise and robust reconstruction," in *2014 IEEE China Summit International Conference on Signal and Information Processing (ChinaSIP)*, Jul. 2014, pp. 790–794.
 66. H. Yang, S. Chen, F. Xi, and Z. Liu, "Quadrature Compressive Sampling SAR Imaging," in *IGARSS 2018 - 2018 IEEE International Geoscience and Remote Sensing Symposium*, Jul. 2018, pp. 5847–5850, iSSN: 2153-7003.
 67. S. Chen, F. Xi, Z. Liu, and B. Bao, "Quadrature compressive sampling of multi-band radar signals at sub-Landau rate," in *2015 IEEE International Conference on Digital Signal Processing (DSP)*, Jul. 2015, pp. 234–238, iSSN: 2165-3577.

68. S. Chen and F. Xi, "Quadrature Compressive Sampling for Multiband Radar Echo Signals," *IEEE Access*, vol. 5, pp. 19 742–19 760, 2017.
69. T. Michaeli and Y. C. Eldar, "Xampling at the Rate of Innovation," *IEEE Transactions on Signal Processing*, vol. 60, no. 3, pp. 1121–1133, Mar. 2012.
70. S. Kirolos, J. Laska, M. Wakin, M. Duarte, D. Baron, T. Ragheb, Y. Massoud, and R. Baraniuk, "Analog-to-Information Conversion via Random Demodulation," in *2006 IEEE Dallas/CAS Workshop on Design, Applications, Integration and Software*, Oct. 2006, pp. 71–74.
71. J. N. Laska, S. Kirolos, M. F. Duarte, T. S. Ragheb, R. G. Baraniuk, and Y. Massoud, "Theory and Implementation of an Analog-to-Information Converter using Random Demodulation," in *2007 IEEE International Symposium on Circuits and Systems*, May 2007, pp. 1959–1962, iSSN: 2158-1525.
72. M. A. Richards, J. A. Scheer, and W. A. Holm, *Principles of Modern Radar: Basic Principles*, 1st ed. Raleigh, NC: Scitech Publishing Inc, 2015.
73. C. A. Balanis, *Antenna Theory: Analysis and Design*, 4th ed. Hoboken, New Jersey: John Wiley & Sons, 2016.
74. "IEEE Standard for Definitions of Terms for Antennas," *IEEE Std 145-2013 (Revision of IEEE Std 145-1993)*, pp. 1–50, Mar. 2014.
75. "IEEE Standard Test Procedures for Antennas," *ANSI/IEEE Std 149-1979*, 1979.
76. D. M. Pozar, *Microwave Engineering*, 4th ed. Hoboken, NJ: Wiley, Nov. 2011.
77. J. Lu, *Design Technology of Synthetic Aperture Radar*, 1st ed. Hoboken, NJ, USA: Wiley-IEEE Press, Aug. 2019.

78. R. J. Mailloux, *Phased Array Antenna Handbook*, 2nd ed. Norwood, MA: Artech House, 2005.
79. R. Bancroft, *Microstrip and Printed Antenna Design*, 2nd ed. Raleigh, NC: Scitech Publishing, Jun. 2009.
80. C. A. Balanis, Ed., *Modern Antenna Handbook*, 1st ed. Hoboken, NJ: Wiley-Interscience, Sep. 2008.
81. Shih-Hsun Hsu, Yu-Jiun Ren, and Kai Chang, "A Dual-Polarized Planar-Array Antenna for S-Band and X-Band Airborne Applications," *IEEE Antennas and Propagation Magazine*, vol. 51, no. 4, pp. 70–78, Aug. 2009.
82. Nidheesh Kumar T R, N. Kumar, M. Sreenivasan, K. G. Thomas, and P. H. Rao, "A multilayer X-band FMCW-SAR microstrip array," in *2016 International Conference on Wireless Communications, Signal Processing and Networking (WiSPNET)*, Mar. 2016, pp. 272–274.
83. A. A. Serra, P. Nepa, G. Manara, G. Tribellini, and S. Cioci, "A Wide-Band Dual-Polarized Stacked Patch Antenna," *IEEE Antennas and Wireless Propagation Letters*, vol. 6, pp. 141–143, 2007.
84. C. A. Mcdonach, D. Nguyen, G. S. Gupta, and A. P. Luscombe, "Design Of A Dual Polarized Microstrip Patch Army For An Advanced Sar Antenna," in *12th Canadian Symposium on Remote Sensing Geoscience and Remote Sensing Symposium*, vol. 4, Jul. 1989, pp. 2275–2277.
85. M. Kai, F. Hou, and D. Sun, "Design of a broadband dual-polarized microstrip antenna array with high isolation," in *2017 Sixth Asia-Pacific Conference on Antennas and Propagation (APCAP)*, Oct. 2017, pp. 1–3.

86. J. A. Ortiz, J. Diaz, N. Aboserwal, J. L. Salazar, L. Jeon, S. Sim, and J. Chun, "Ultra-compact universal polarization X-band unit cell for high-performance active phased array radar," in *2016 IEEE International Symposium on Phased Array Systems and Technology (PAST)*. Waltham, MA, USA: IEEE, Oct. 2016, pp. 1–5.
87. Li, Lai, Luk, and Lau, "A wideband patch antenna with cross-polarization suppression," *IEEE Antennas and Wireless Propagation Letters*, vol. 3, pp. 211–214, 2004.
88. B. Li, Y. Yin, W. Hu, Y. Ding, and Y. Zhao, "Wideband Dual-Polarized Patch Antenna With Low Cross Polarization and High Isolation," *IEEE Antennas and Wireless Propagation Letters*, vol. 11, pp. 427–430, 2012.
89. J. D. Kraus and R. J. Marhefka, *Antennas For All Applications*, 3rd ed. New York: McGraw-Hill Science/Engineering/Math, Nov. 2001.
90. A. C. Ludwig, "The definition of cross polarization." *IEEE Transactions on Antennas and Propagation*, vol. 21, no. 1, pp. 116 – 119, Jan. 1973.
91. F. Biondi, "Super resolution of synthetic aperture radar data by convex optimization," in *4th International Workshop on Compressed Sensing Theory and its Applications to Radar, Sonar and Remote Sensing (CoSeRa)*, Sep. 2016, pp. 28–32.
92. C. Jiong and Y. Jian, "Super-Resolution of Polarimetric SAR Images for Ship Detection," in *International Symposium on Microwave, Antenna, Propagation and EMC Technologies for Wireless Communications*, Aug. 2007, pp. 1499–1502.

93. W. Qui, H. Zhao, J. Zhou, and Q. Fu, "High-Resolution Fully Polarimetric ISAR Imaging Based on Compressive Sensing," *IEEE Transactions on Geoscience and Remote Sensing*, vol. 52, no. 10, pp. 6119–6131, Oct. 2014.
94. M. Amin, Ed., *Compressive Sensing for Urban Radar*, 1st ed. Boca Raton: CRC Press, Aug. 2014.
95. R. Touzi, P. W. Vachon, and J. Wolfe, "Requirement on Antenna Cross-Polarization Isolation for the Operational Use of C-Band SAR Constellations in Maritime Surveillance," *IEEE Geoscience and Remote Sensing Letters*, vol. 7, no. 4, pp. 861–865, Oct. 2010.
96. K. Sarabandi, F. T. Ulaby, and M. A. Tassoudji, "Calibration of polarimetric radar systems with good polarization isolation," *IEEE Transactions on Geoscience and Remote Sensing*, vol. 28, no. 1, pp. 70–75, Jan. 1990.
97. A. Freeman, Y. Shen, and C. Werner, "Polarimetric SAR calibration experiment using active radar calibrators," *IEEE Transactions on Geoscience and Remote Sensing*, vol. 28, no. 2, pp. 224–240, Mar. 1990.
98. J. van Zyl, "A Technique To Calibrate Polarimetric Radar Images Using Only Image Parameters And Trihedral Corner Reflectors," in *12th Canadian Symposium on Remote Sensing Geoscience and Remote Sensing Symposium*, vol. 5, Jul. 1989, pp. 2889–2892.
99. Y. T. Jung and S.-E. Park, "Comparative Analysis of Polarimetric SAR Calibration Methods," *Remote Sensing*, vol. 10, no. 12, p. 2060, Dec. 2018. [Online]. Available: <https://www.mdpi.com/2072-4292/10/12/2060>
100. E. van den Berg and M. P. Friedlander, "SPGL1: A solver for large-scale sparse reconstruction," Jun. 2007. [Online]. Available: <https://friedlander.io/spgl1>

101. —, “Probing the Pareto frontier for basis pursuit solutions,” *SIAM Journal on Scientific Computing*, vol. 31, no. 2, pp. 890–912, Nov. 2008.
102. R. Obermeier and J. A. Martinez-Lorenzo, “Sensing Matrix Design via Mutual Coherence Minimization for Electromagnetic Compressive Imaging Applications,” *IEEE Transactions on Computational Imaging*, vol. 3, no. 2, pp. 217–229, Jun. 2017.
103. L. Gan, C. Ling, T. T. Do, and D.-N. Tran, “Analysis of the Statistical Restricted Isometry Property for Deterministic Sensing Matrices Using Stein’s Method,” 2009. [Online]. Available: <http://www.dsp.ece.rice.edu/files/cs/GanStatRIP.pdf>
104. P. Patel, “A dual polarised microstrip antenna with low cross-polarisation, for SAR applications,” in *IEEE Antennas and Propagation Society International Symposium. 1996 Digest*, vol. 3, Jul. 1996, pp. 1536–1539.
105. J. Becker and J. A. Jackson, “Robustness of Dropped-Channel PolSAR CS,” *Submitted to IEEE Transactions on Aerospace Electronics Systems*, Oct. 2021.
106. “ANSYS HFSS.” [Online]. Available: <https://www.ansys.com/products/electronics/ansys-hfss>
107. B. S. Tomar, S. Bharadwaj, and P. Gupta, “Designing A Microstrip Square Patch Antenna,” in *2019 Fifth International Conference on Image Information Processing (ICIIP)*, Nov. 2019, pp. 564–567, iSSN: 2640-074X.
108. M. Cetin, “Feature-enhanced synthetic aperture radar imaging,” Ph.D. dissertation, 2001.

REPORT DOCUMENTATION PAGE					<i>Form Approved</i> OMB No. 0704-0188	
<p>The public reporting burden for this collection of information is estimated to average 1 hour per response, including the time for reviewing instructions, searching existing data sources, gathering and maintaining the data needed, and completing and reviewing the collection of information. Send comments regarding this burden estimate or any other aspect of this collection of information, including suggestions for reducing the burden, to Department of Defense, Washington Headquarters Services, Directorate for Information Operations and Reports (0704-0188), 1215 Jefferson Davis Highway, Suite 1204, Arlington, VA 22202-4302. Respondents should be aware that notwithstanding any other provision of law, no person shall be subject to any penalty for failing to comply with a collection of information if it does not display a currently valid OMB control number.</p> <p>PLEASE DO NOT RETURN YOUR FORM TO THE ABOVE ADDRESS.</p>						
1. REPORT DATE (DD-MM-YYYY) 06/16/2022		2. REPORT TYPE PhD Dissertation			3. DATES COVERED (From - To) August 2017 - June 2022	
4. TITLE AND SUBTITLE Theory and Design of a Highly Compressed Dropped-Channel Polarimetric Synthetic Aperture Radar				5a. CONTRACT NUMBER		
				5b. GRANT NUMBER		
				5c. PROGRAM ELEMENT NUMBER		
6. AUTHOR(S) Becker, John, T, Capt				5d. PROJECT NUMBER		
				5e. TASK NUMBER		
				5f. WORK UNIT NUMBER		
7. PERFORMING ORGANIZATION NAME(S) AND ADDRESS(ES) Air Force Institute of Technology Graduate School of Engineering and Management (AFIT/EN) 2950 Hobson Way Wright-Patterson AFB OH 45433-7765					8. PERFORMING ORGANIZATION REPORT NUMBER AFIT-ENG-DS-22-J-004	
9. SPONSORING/MONITORING AGENCY NAME(S) AND ADDRESS(ES) Intentionally Left Blank					10. SPONSOR/MONITOR'S ACRONYM(S)	
					11. SPONSOR/MONITOR'S REPORT NUMBER(S)	
12. DISTRIBUTION/AVAILABILITY STATEMENT DISTRIBUTION STATEMENT A. APPROVED FOR PUBLIC RELEASE; DISTRIBUTION IS UNLIMITED.						
13. SUPPLEMENTARY NOTES This work is declared a work of the U.S. Government and is not subject to copyright protection in the United States.						
14. ABSTRACT Compressed sensing (CS) is a recent mathematical technique that leverages the sparsity in certain sets of data to solve an underdetermined system and recover a full set of data from a sub-Nyquist set of measurements of the data. Given the size and sparsity of the data, radar has been a natural choice to apply compressed sensing to, typically in the fast-time and slow-time domains. Polarimetric synthetic aperture radar (PolSAR) generates a particularly large amount of data for a given scene						
15. SUBJECT TERMS Compressed Sensing, Synthetic Aperture Radar, Basis Pursuit, Antenna Design						
16. SECURITY CLASSIFICATION OF:			17. LIMITATION OF ABSTRACT	18. NUMBER OF PAGES	19a. NAME OF RESPONSIBLE PERSON	
a. REPORT	b. ABSTRACT	c. THIS PAGE			Dr. Julie Ann Jackson, AFIT/ENG	
U	U	U			19b. TELEPHONE NUMBER (Include area code) 937-255-3636 x4678 julie.jackson@afit.edu	

INSTRUCTIONS FOR COMPLETING SF 298

1. REPORT DATE. Full publication date, including day, month, if available. Must cite at least the year and be Year 2000 compliant, e.g. 30-06-1998; xx-06-1998; xx-xx-1998.

2. REPORT TYPE. State the type of report, such as final, technical, interim, memorandum, master's thesis, progress, quarterly, research, special, group study, etc.

3. DATE COVERED. Indicate the time during which the work was performed and the report was written, e.g., Jun 1997 - Jun 1998; 1-10 Jun 1996; May - Nov 1998; Nov 1998.

4. TITLE. Enter title and subtitle with volume number and part number, if applicable. On classified documents, enter the title classification in parentheses.

5a. CONTRACT NUMBER. Enter all contract numbers as they appear in the report, e.g. F33315-86-C-5169.

5b. GRANT NUMBER. Enter all grant numbers as they appear in the report. e.g. AFOSR-82-1234.

5c. PROGRAM ELEMENT NUMBER. Enter all program element numbers as they appear in the report, e.g. 61101A.

5e. TASK NUMBER. Enter all task numbers as they appear in the report, e.g. 05; RF0330201; T4112.

5f. WORK UNIT NUMBER. Enter all work unit numbers as they appear in the report, e.g. 001; AFAPL30480105.

6. AUTHOR(S). Enter name(s) of person(s) responsible for writing the report, performing the research, or credited with the content of the report. The form of entry is the last name, first name, middle initial, and additional qualifiers separated by commas, e.g. Smith, Richard, J, Jr.

7. PERFORMING ORGANIZATION NAME(S) AND ADDRESS(ES). Self-explanatory.

8. PERFORMING ORGANIZATION REPORT NUMBER. Enter all unique alphanumeric report numbers assigned by the performing organization, e.g. BRL-1234; AFWL-TR-85-4017-Vol-21-PT-2.

9. SPONSORING/MONITORING AGENCY NAME(S) AND ADDRESS(ES). Enter the name and address of the organization(s) financially responsible for and monitoring the work.

10. SPONSOR/MONITOR'S ACRONYM(S). Enter, if available, e.g. BRL, ARDEC, NADC.

11. SPONSOR/MONITOR'S REPORT NUMBER(S). Enter report number as assigned by the sponsoring/monitoring agency, if available, e.g. BRL-TR-829; -215.

12. DISTRIBUTION/AVAILABILITY STATEMENT. Use agency-mandated availability statements to indicate the public availability or distribution limitations of the report. If additional limitations/ restrictions or special markings are indicated, follow agency authorization procedures, e.g. RD/FRD, PROPIN, ITAR, etc. Include copyright information.

13. SUPPLEMENTARY NOTES. Enter information not included elsewhere such as: prepared in cooperation with; translation of; report supersedes; old edition number, etc.

14. ABSTRACT. A brief (approximately 200 words) factual summary of the most significant information.

15. SUBJECT TERMS. Key words or phrases identifying major concepts in the report.

16. SECURITY CLASSIFICATION. Enter security classification in accordance with security classification regulations, e.g. U, C, S, etc. If this form contains classified information, stamp classification level on the top and bottom of this page.

17. LIMITATION OF ABSTRACT. This block must be completed to assign a distribution limitation to the abstract. Enter UU (Unclassified Unlimited) or SAR (Same as Report). An entry in this block is necessary if the abstract is to be limited.